University of Alberta

Active Flow Control of a Precessing Jet

by

Hamed Babazadeh

A thesis submitted to the Faculty of Graduate Studies and Research
in partial fulfillment of the requirements for the degree of

Master of Science

Department of Mechanical Engineering

Spring 2011
Edmonton, Alberta

Examining Committee

C. R. (Bob) Koch (Supervisor), Mechanical Engineering

David S. Nobes (Co-Supervisor), Mechanical Engineering

Morris R. Flynn, Mechanical Engineering

Suzanne M. Kresta, Chemical and Materials Engineering

Abstract

Active flow control of a precessing jet is the focus of this work. A round jet confined by a round cavity exhibits a self-excited rotational motion, precession, for a specific range of cavity lengths. Active flow control of this unstable flow provides the ability to control near-field mixing of the precessing jet. Twelve micro-jets on the periphery of the nozzle inlet are used as actuation and near-field pressure data is measured by four pressure probes at the chamber exit to monitor the flow behavior. A phase plane, based on pressure signals, is used to find a Reynolds number and actuation frequency range where actuation stabilizes the flow motion. Phase-locked stereoscopic PIV is also used to validate the pressure processing tool. The results confirm the pressure measurement and micro-jet actuation can be employed to develop a future closed-loop flow control on a precessing jet.

Acknowledgements

Dr. Bob Koch, Advisor for his guidance, support, and always encouraging me to think about the "big picture"! I will never forget his help over weekdays and weekends, especially during the course of writing my thesis.

Dr. David Nobes, Advisor for his guidance and support and helping me with all details of academic research ranging from technical writing to maintenance of equipments. Despite his hectic schedule, the door of his office is always open (even over weekends) to discuss every detail of my experiments, and always has some inspiring ideas about what to do.

Bernie Faulkner, Specialist Technician don't hesitate to talk to him if you have any technical problem in the lab.

Rick Conrad, Electronic Engineering Technician

Tuula Hilvo, Technician

Roger Marchand, Technical Services Supervisor

Andrew Campbell, Machinist Technician

for their help during fabrication of my setup and

Natural Sciences and Engineering Research Council of Canada

Alberta Ingenuity

for their financial support of this research and

Dr. Morris Flynn, Mechanical Engineering

Dr. Suzanne Kresta, Chemical and Material Engineering

for their great comments as my committee members and my friends in

4-28 MecE, Controls Lab

5-27 MecE, Optical Diagnostic Lab

5-25 MecE, Aerosol/Fluid Mechanics

3-31 MecE, Thermodynamics and Kinetics Lab

4-25 MecE, Advanced Structures & Materials Research Lab

2-9 MecE, Aerosol Research Laboratory

5-23 MecE, Water Channel

3-23 MecE, Advanced Robotics and Controls Lab

2-7 MecE, Composite Materials Engineering

National Institute for Nanotechnology (NINT)

for our inspiring discussions and all my friends in the University of Alberta whose warm friendship helped me to survive in Edmonton's cold winters.

Contents

List of Tables

List of Figures

Nomenclature

Symbols

C_μ	Momentum coefficient [-]
d	Chamber inlet diameter [m]
d_{cj}	Micro-jet diameter [m]
D	Diameter of chamber [m]
D_c	Diameter of center body [m]
D_i	Pre-conditioner pipe diameter [m]
D_o	Chamber outlet diameter [m]
f	Frequency of actuation [Hz]
f_p	Frequency of precession [Hz]
g	Gravity acceleration $[\frac{m}{s^2}]$
h	Height of pressure sensors with respect to water level [m]
H	Height of pressure sensors with respect to pressure probes [m]
L	Length of chamber [m]
L_c	Center body distance [m]
$\dot{m}$	Mass flow rate $[\frac{kg}{s}]$
n	Number of simultaneously firing injectors [-]

p	Pressure [Pa]
r	Phase-plane radius [Pa]
$\tilde{R}$	Relative difference of R_n with and without center body [-]
R_n	Normalized average of phase-plane radius within actuation [-]
Re	Reynolds number [-]
s	Directional area under jet high velocity trajectory curve in phase-plane between to successive points [Pa^2]
S	Directional total area bounded by jet high velocity trajectory in phase-plane [Pa^2]
St_d	Strouhal number based on nozzle diameter [-]
St_h	Strouhal number based on step height [-]
St_L	Strouhal number including chamber length [-]
t	Time [s]
t_w	Cross correlation window size [s]
U_i	Axial velocity in nozzle inlet $[\frac{m}{s}]$
U_{cj}	Velocity of control jet $[\frac{m}{s}]$
v	Voltage [V]
w	Center body thickness [m]
w'	RMS Axial velocity in chamber exit plane$[\frac{m}{s}]$
W	Axial velocity in chamber exit plane $[\frac{m}{s}]$
x	Pressure difference between horizontal pressure probes [Pa]
X	Horizontal direction in the chamber exit plane, perpendicular to the chamber axis [m]

y	Pressure difference between vertical pressure probes [Pa]
Y	Vertical direction in the chamber exit plane, perpendicular to the chamber axis [m]
z	The distance from chamber outlet plane along the chamber axis [m]
Z	Direction perpendicular to the chamber exit plane [m]

Greek

α	Micro-jet injection angle [degree]
β	Phase lag between jet high velocity region and injection line [degree]
γ	Lip deflection angle [degree]
Δt	Opening time (pulse width) [s]
Δt_s	Switching time [s]
θ	Phase of jet high velocity region [degree]
μ	Dynamic viscosity [Pa.s]
ρ	Water density $[\frac{kg}{\mathrm{m}^3}]$
φ	Injection line phase [degree]
Ω	Pump rotation speed [RPM]

Acronyms

AFC	Active Flow Control
AJ	Axial Jet
CB	Center Body
CCW	Counter Clockwise

CW	Clockwise
LDA	Laser Doppler Anemometry
PE	Polyethylene
PJ	Precessing Jet
PTU	Programmable Time Unit
px	Pixel
RMS	Root Mean Square
S-PIV	Stereoscopic Particle Image Velocimetry

Subscripts and Superscripts

0	Initial condition
$act.$	Actuation
$atm.$	Atmosphere
c	Collected pressure
cj	Control jet
i	Nozzle inlet
STD	Standard Deviation
w	Cross Correlation window size

Chapter 1

Introduction

Mixing of two or more fluids is at the heart of many industrial applications in which the performance of the overall process or the quality of final product depends entirely on the level of mixing [1]. For instance, a well mixed air/fuel mixture can improve the overall performance of an engine (or heater) by increasing the combustion efficiency, reducing combustion instability and emissions [2]. The potential benefits of mixing enhancement range from saving billions of dollars in fuel cost for transportation due to combustion improvement to facilitate and expedite chemical reactions in petroleum and other chemical industries [3]. The ubiquitous applications of jets in industrial processes provide motivation for this research on mixing enhancement of jet flows.

Jet flow is a model to describe any fluid flow in which the flow from a limited space expands and spreads into a free environment with a velocity gradient with respect to the free environment. Fuel injection into the combustion chamber and dispersion effluent into rivers through a diffuser are examples which can be studied using jet flow models [4]. Recently, a specific configuration of jet flow has found applications as combustion burner in several industries (e.g. lime, cement) [5]. A precessing jet, in its simplest form, is a cylindrical chamber with a small axisymmetric inlet at one end as shown in Figure 1.1. This configuration destabilizes the free jet which leads to a self-excited oscillatory rotational motion of the entire jet. This rotational motion causes a significant increase in entrainment rate and heat transfer which result in a significant reduction in NO_x emissions (up to 70%), considerable fuel saving (up to 20%) and an improvement in product quality (up to 10%, e.g. in lime industry) [6].

The objective of this research is to understand and characterize the behavior of a precessing jet by different flow control strategies. In this chapter, existing studies on precessing jet in the literature are first summarized and then active flow control is introduced.

1.1 The precessing jet

A precessing jet consists of an axisymmetric jet with a nozzle inlet diameter of d which discharges through a sudden expansion into a confined chamber with a length L and a diameter D such that $D > d$ as shown in Figure 1.1. The Reynolds number of the precessing jet is defined in the similar way to the axisymmetric jet:

$$Re = \frac{\rho U_i d}{\mu} \tag{1.1}$$

where U_i is the average axial velocity at the nozzle inlet and ρ and μ are the working fluid density and dynamic viscosity, respectively.

This flow belongs to a category of self-induced oscillatory flows which are denoted as either flapping or precessing jet, depending on geometry [7]. A flapping jet refers to a 2D jet (a long slot) which discharges into a space which is confined between two parallel plates of finite length in the jet downstream direction. As the flow leaves the slot into the sudden expansion, it attaches to one wall or the other asymmetrically, leading to an oscillatory flow which frequently deflects up and down [7, 8].

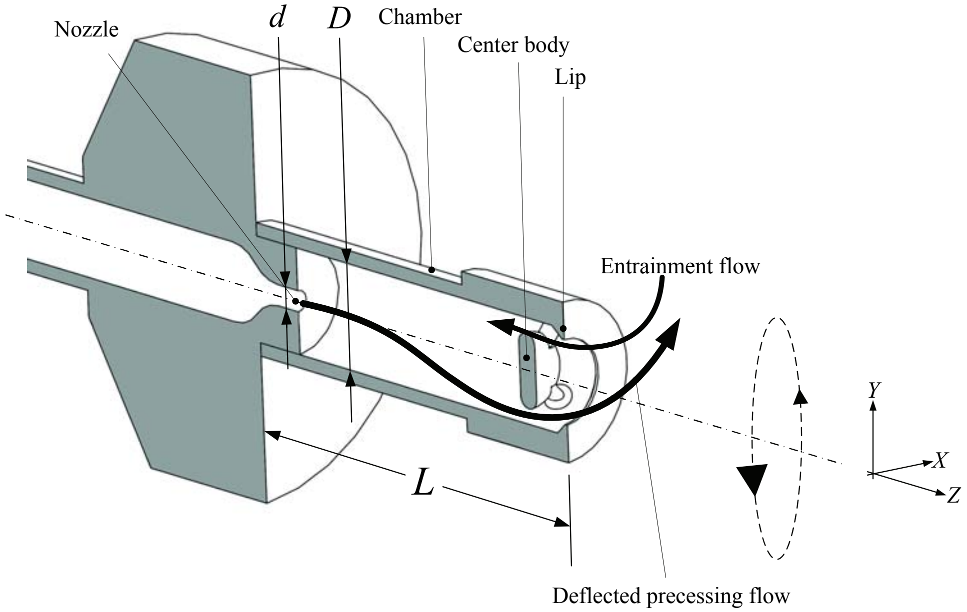

Figure 1.1: Schematic description of a precessing jet with a center body in the precessing mode.

A precessing jet is a circular axisymmetric jet which initially discharges into a confined pipe, concentric to the jet axis. The pipe is referred to as the chamber (or cavity or shroud) [9]. Similar to a flapping jet, a precessing jet also reattaches to part of the chamber wall. However, the precessing jet reattaches asymmetrically to the wall and then deflects as it leaves the chamber due to the exit lip. Surface flow visualization techniques in air and water flow visualization are used to investigate the flow inside the chamber showing the precessing jet reattaches to the chamber wall at about halfway down the chamber length [9]. A lip is often mounted at the chamber exit to assist the deflection as shown in Figure 1.1. The deflection angle between the precessing jet and the chamber axis is reported about 50° which decreases to 30° at Z =0.4D downstream of the chamber outlet plane [10]. The flow leaving the chamber rotates around an axis which itself arbitrarily spins (precesses) around the chamber axis as it exits the chamber (denoted *precessing mode*). Momentary axisymmetric jet flow behavior (denoted *axial mode*) where the jet exits the chamber uniformly in the axial direction can be interspersed with the precessing mode. A double peak shape of total pressure profiles at the chamber exit plane and the subsequent evolution to a bell mouth shape profile have been observed downstream indicating that the precessing mode evolves into the axial mode in downstream [11]. These modes inside the chamber are

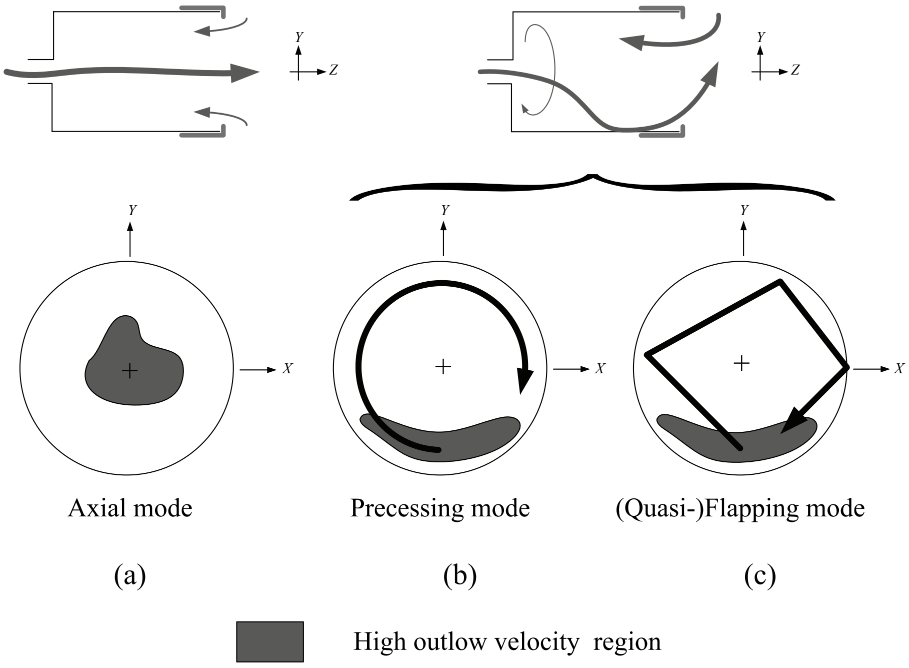

Axial mode (a)

Precessing mode (b)

(Quasi-)Flapping mode (c)

Figure 1.2: Representation of different flow patterns (modes) in precessing jet.

depicted in Figure 1.2. The flow can exhibit temporal switching between the modes with the probability of being in a certain mode depending on the geometry of the nozzle and flow conditions. For instance, adding a baffle, called a center body, at the chamber exit (see Figure 1.1) decreases the probability of the axial mode while stabilizing the precessing mode [12].

A geometrical ratio range ($2 \leq \frac{L}{D} \leq 3.5$) in which precession occurs was found through a parametric study [13, 14]. Recently, the effect of chamber length on the probability of precessing jet is studied and shows that the highest probability occurs in a range of $2 \leq \frac{L}{D} \leq 2.75$ but increasing the length ratio causes the probability of jet precession to dramatically drop [15]. An experimental study of different jet configurations using particle trace flow visualization found that a minimum Reynolds number of 3700 and expansion ratio ($\frac{D}{d} = 3.75$) are needed for precession to occur [16].

Two flow regimes are observed in the precessing mode. In the first mode, the jet precesses regularly around the chamber (see Figure 1.2(b)). A model describing flow precession can be found in [17]. In the second mode, the flow does not complete a precessing cycle around the centerline, but instead jumps among a few locations of the chamber wall (see Figure 1.2(c)). These flow regimes were initially reported in [13, 18]. A precessing jet, in a Reynolds number range of $Re = 50,000 - 200,000$ and expansion ratio of $\frac{D}{d} = 2 - 6$ was investigated numerically [19]. The results of numerical simulations were used to establish a flow regime map consisting of Reynolds number versus expansion ratio. The numerical results show that at high Reynolds number ($Re = 100,000$) and expansion ratio between $4 \leq \frac{D}{d} \leq 6$, only regular precession exists whereas in expansion ratios of $3 \leq \frac{D}{d} \leq 4$, along with precession, quasi-flapping behavior was observed in which jet may be unable to complete a precessing cycle.

The frequency of the jet precession is used to define Strouhal number of the precessing jet:

$$St_d = \frac{f_p d}{U_i} \tag{1.2}$$

where f_p is the frequency of precession. A comprehensive review on Strouhal number for different jets (with or without excitement) can be found in [11]. Dye-trace measurements in water show that the frequency of precession is between 0.05 Hz to 0.25 Hz and increases linearly with Reynolds number (Re=5,000 to 20,000), indicating that the jet precesses with a constant Strouhal number, $St_h = 0.005$; where St_h is defined based on the inlet step height ($h = \frac{(D-d)}{2}$) [11]:

$$St_h = \frac{f_p h}{U_i} \tag{1.3}$$

Approximately the same results are reported for air using hot wire anemometry [11]. The numerical simulation also verifies the weak dependence of Strouhal on Reynolds number [19].

An experimental study of a precessing jet with an expansion ratio, $\frac{D}{d} = 6.4$, and relative length, $\frac{L}{D} = 2.6$, at high Reynolds number ranging from $Re = 53,000$ to $Re = 134,000$ is described in [9]. Several pressure probes are mounted in different locations to identify the flow mode (i.e. either axial or precessing) and they found the probability of precessing mode to be around 95% with a constant Strouhal number of ($St_d = 0.0015$) at relatively high Reynolds number ($Re > 50,000$).

A hot wire probe near the chamber exit was utilized to find the frequency of precession in a precessing jet with lip and center body [20]. Total pressure measurement was made along the nozzle axis chamber for $1.5 \leq \frac{L}{D} \leq 3.5$. They observed that the downstream mixing field is more affected by Strouhal number than Reynolds number. They also found that the precessing frequency increases linearly with either $\frac{L}{D}$ or Reynolds number. The numerical simulation results also indicate that by increasing the expansion ratio, Strouhal number increases linearly ($St_d \propto \frac{D}{d}$) [19]. So to characterize downstream mixing field by Strouhal number, the influence of the chamber length on the Strouhal number definition should be considered. The following equation instead of Equation 1.2 or $St_h = \frac{1}{2}(\frac{D}{d} - 1)St_d$ is suggested [10]:

$$St_L = C_2(\frac{L}{d})^2 St_d \tag{1.4}$$

Nevertheless, this definition has not been commonly used in the literature afterwards.

A precessing jet configuration leads to a self-excited rotational oscillatory motion of the entire jet [13] which provides a unique way for mixing fuel, e.g. natural gas, into the surrounding air [6]. Using this configuration for a burner decreases flame stand-off distance by a factor of 4 based on chamber diameter [21]. The stirring action of a precessing jet gives a highly luminous flame despite the inherently poor luminosity achieved by natural gas combustion. The poor flame luminosity means that more natural gas needs to be burnt to achieve the same radiant heat transfer required for an industrial process (e.g. to the kiln charge). Therefore, the deficiency of natural gas fuel is overcome through the application of precessing jet burners [6]. Full-scale installation of commercial gas-firing precessing jet burners systems in rotary kilns (15-120 MW) in process industries (e.g. cement, lime, alumina and zinc oxide) shows 50-70% reduction of NO_x emissions and simultaneously, a fuel saving of about 5-20% relative to current burners [6]. Application of precessing jet in Gyro-Therm gas burner for rotary kiln use has shown a significant reduction in NO_x (more than 50%), reduction in fuel consumption (by 5%) and an improvement in product quality [22]. Using the Gyro-Therm burner equipped with precessing jet technology in lime production resulted in fuel savings around 7%, NO_x reduction of 35% and production increase by 8% [6]. These results confirm that the precessing jet improves the combustion process by manipulating the downstream near field mixing of an axisymmetric jet.

Several studies have been carried out to compare the downstream mixing field of the precessing jet (after leaving the chamber) with a free jet. The length of potential core downstream of a precessing jet nozzle is $Z \simeq 3.5d$ (in free jet, it is $Z \simeq 6d$) and axial velocity decay rate (spreading rate) of the precessing jet is more than a free jet and in contrast with a free jet, this rate changes along with axial direction non-linearly [10]. To identify the dominant in-plane ($X - Y$ plane) vortical structures and investigate the trajectory of vortices, a precessing jet with center body was studied by a phase-averaged single camera PIV measurement [23]. A filtered hot wire signal was used to trigger PIV system. PIV results reveal the trajectory of vortical structures of the precessing jet at the chamber exit plane. Using the numerical simulation, a spiral mode is observed in the flow downstream which rotates in opposite direction to the precession [19]. A precessing jet was further investigated using phase-averaged LDA axial velocity measurement within and in the near external field with lip and center body in air [10]. The results confirm that entrainment rate of precessing jet into the chamber is between six and seven times that of an equivalent unconfined jet [10].

Different configurations have been suggested to alter the downstream mixing field of a precessing jet. A mechanically rotating nozzle was developed in [24] to study a precessing jet where Reynolds and Strouhal number effects are decoupled. The frequency used in Strouhal definition is the frequency of the mechanically rotating nozzle. A four-hole pitot tube Cobra probe was used to investigate phase-averaged three dimensional velocity components which shows that the decay of maximum phase-averaged axial velocity component is much higher than for an axisymmetric jet. A mechanically precessing jet was studied using hot wire probe resulting in a critical Strouhal number of 0.01 based on the nozzle diameter [25]. At $St < 0.01$, the flow never evolves into axisymmetric jet far downstream of the chamber exit. Above this critical value, the precessing jet is only present in the near field of the chamber exit plane and eventually develops into a simple jet-like regime in the far field; for instance, at St=0.02, the flow switches to a simple jet at $\frac{Z}{d} \geq 20$ [25].

Another proposed configuration is a co-annular nozzle [26] for two-phase applications where the inner flow benefits from precessing jet configuration. Also a triangular nozzle inlet for the precessing jet is introduced in [27] to stabilize the precessing mode and to investigate the effect of density ratio on the near field of the precessing jet with a triangular nozzle.

The downstream of a precessing jet can also be manipulated by altering the precessing jet in upstream of the nozzle inlet. To investigate the effect of different initial conditions on the jet precession, a time-averaged LDA velocity measurement was conducted at $Z = 0.63d$ downstream of the chamber outlet plane for different initial conditions: a long pipe, a smooth contraction and an orifice [12]. An open chamber, a chamber with lip and a chamber with lip and center body were used with each initial conditions. A double peak axial velocity profile instead of a bell shaped profile and increased radial velocity indicate a precessing jet. Having a dominant frequency peak in power spectrum of the near field pressure (or velocity) also is an indicator of a precessing jet. Orifice and long pipe promote precessing jet mode probability in comparison to the smooth contraction. Adding a lip increases the predominance of precessing jet mode and center body stabilizes precessing jet mode. The initial condition does not have any significant effect on Strouhal number for $Re > 100,000$. The orifice results in the highest decay rate (turbulence intensity), while the long pipe has the lowest spreading rate and turbulence intensity having more similarity to a free jet. A more detailed study of the effect of initial conditions on jet flow can be found in [5,15]. The effect of initial conditions on a precessing jet is studied for an orifice, smooth contraction nozzle and a pipe using hot wire measurements at the chamber exit [28]. The results show that the precession frequency is the highest for the orifice flow while for the pipe it is lowest. The Strouhal number of the orifice is double that of the pipe, and is 1.6 times the smooth contraction inlet.

The precession instability observed in the precessing jet is a different phenomenon from jet shear layer instabilities due to the fact that the precession frequency is two orders of magnitude lower than the frequency observed in a shear layer [9]. Therefore, a low frequency ($<$ 10 Hz) excitation of the precession phenomenon could be an alternative to manipulate the near field mixing of the precessing jet inside the chamber. The precession instability makes the flow extremely sensitive to the variations in the initial and boundary conditions. The unstable nature of the precessing jet provides a flow which can be controlled in a desired way by adding a minimum amount of energy using the actuation to excite the flow. That is why the precessing jet is an ideal fundamental flow to study active flow control. For this study, a precessing jet shown in Figure 1.1 is selected to investigate different stabilizing flow control strategies to provide a framework for feedback control of flow systems in the future.

1.2 Flow control

Flow control refers to the manipulation of a flow field in order to alter the flow towards a desired state. The objective of flow control varies ranging from drag reduction in airplanes to mixing enhancement in industrial burners [3,29]. Flow control is often classified into two major categories which are based on whether or not auxiliary power is used for actuation [3]. Manipulation of a turbulent free jet using different nozzle shapes is an example of passive control [30]. Using a pulsed micro-jet around an axisymmetric jet to alter its near field mixing is an example of Active Flow Control (AFC) [31].

AFC is also classified in two categories as shown in Figure 1.3. In predetermined control (i.e. open loop control) actuation is implemented regardless of the particular state of the flow whereas in reactive (closed loop) control, actuation is continuously adjusted based on a measured signal [3]. Feedback control of a round jet/diffuser in transitory stall [32] is an example of closed loop flow control. Reactive flow is further classified into two categories based on whether the measured and controlled variables are same or not; The former is the subject of feedback control whereas the latter refers to feedforward control. Reactive flow control often needs a model to predict the flow behavior to achieve robustness and performance goals [3]. Different models ranging from dynamical systems to physical models are utilized for feedback control. To develop an appropriate model for feedback control, the behavior of the flow under the predetermined control should be identified.

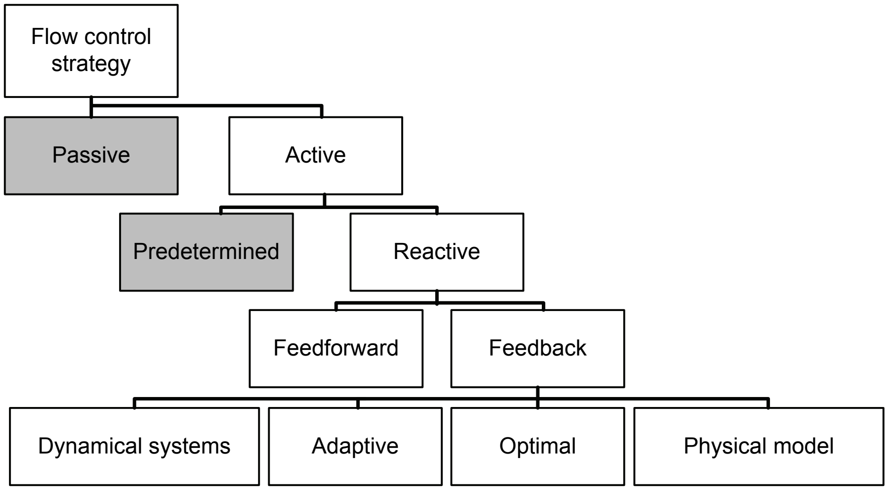

Figure 1.3: Classification of flow control strategies (reproduced from [3]).

Over the last century, from Prandtl's experiment in 1904 on boundary layer separation delay using suction [3], to the recent studies on feedback control of a high Reynolds number jet using plasma actuators [33], different control methods and several instruments have been used for flow control purposes. A summary of different flow control actuators and sensors along with their advantages and disadvantages can be found in [34]. A more detailed discussion of flow control sensors and actuators along with the contribution of MEMS technology to flow control can be found in [35,36]. A comprehensive review on closed-loop control of combustion with an emphasis on control techniques can be found in [37]. A review on open and closed-loop combustion control with an emphasis on control objectives and sensing and actuation strategies can be found in [38]. A detailed discussion on implementation of different control methods for stabilization and mixing control is given in [2].

In this study both passive control, by implementing a center body and varying the chamber length, and active control, by actuation through micro-jet pulsed injection are considered. This research deals with identification of the precessing jet using measurements at the chamber exit which can be used in future works for feedback control purposes. Although this study uses two measurement techniques, no feedback signal is used for actuation adjustment. Therefore, the current research is a predetermined active flow control. For this type of control it is essential to have an effective actuation (controllability) and be able to measure the phenomena of interest (observability). Based on the classification introduced in [34], the actuation method used in this research (micro-jet injection) and pressure sensors are categorized in the literature as *pulsed jet* and *piezoresistive dynamic pressure*, respectively.

1.3 Motivation and objectives

The objective of this research is to find appropriate sensors, actuators and control strategies to enhance the mixing in the precessing jet flow. The focus of this study is to identify and document the behavior of precessing jet under actuation. This is done by creating a phase diagram to describe flow response to the micro-jet actuation at different Reynolds number and actuation frequencies. This phase plane is later validated using Stereoscopic Particle Image Velocimetry (S-PIV).

The material of this thesis is organized into four chapters. Literature review on precessing jet and flow control is given in this chapter. The experimental setup along with the calibration of all instruments are detailed in Chapter 2. Chapter 3 describes different methods which are used to study the motion of a precessing jet within the actuation using pressure probes at the chamber exit. A new measure for the precessing jet location monitoring based on only four pressure probes is proposed in Chapter 3. This method is validated using S-PIV in Chapter 4. Detailed three component flow imaging using S-PIV for two Reynolds numbers is also documented in Chapter 4. Finally, conclusions and future work are discussed in the last chapter. Appendix A includes the drawings of all fabricated parts in this research. The custom code used to manage the actuation system and pressure measurements is introduced in Appendix B. Pressure and S-PIV data are analyzed using the codes listed in Appendix C. Appendix D contains a detailed discussion about the cross correlation method. The phase plane and direction analysis of all data set are produced in Appendix E.1 and E.2, respectively and average and RMS axial velocities captured by S-PIV are given in Appendix E.3.

Chapter 2

Experimental setup and measurement techniques

A precessing jet is used as the system for this flow control study due to the unstable and chaotic nature of the flow. This makes it an ideal case study for the implementation of flow control strategies. Actuation, either passive or active, and sensors are also needed for active flow control. Adding a center body and varying chamber length are the passive control approaches used while twelve micro-jets are the active control actuation used in this research. Four pressure sensors are placed at the chamber lip and are tested as potential sensors for feedback control. To use these pressure sensors for feedback control, their ability to measure the phenomena to be controlled (observability) needs to be validated. S-PIV is used for this purpose. In the following sections, each of these components related to the experiment setup are discussed in detail.

2.1 Flow facility

A schematic representation of the flow and measurement system including connections is summarized in Figure 2.1. The flow system is depicted using a blue color while the actuation is displayed by red. The blocks in black represent pressure measurement elements and green is for the S-PIV setup. A pump drives the working fluid in the flow system (blue elements). Twelve injectors are devoted to inject the working fluid which is supplied by a pressure vessel (red objects). The injectors are driven by an injector drive controller which receives commands from a DAQ card (red elements). Two separate DAQ cards are employed for analogue pressure signal acquisition and digital output commands for the actuation system. A DAQ card receives pressure data collected using four pressure sensors from a demodulator (black elements). A Programmable Time Unit (PTU) controls the trigger timing for the laser and cameras (green parts). Two thick black lines are the trigger signals from the actuation system to trigger the laser and cameras. PTU timing data is

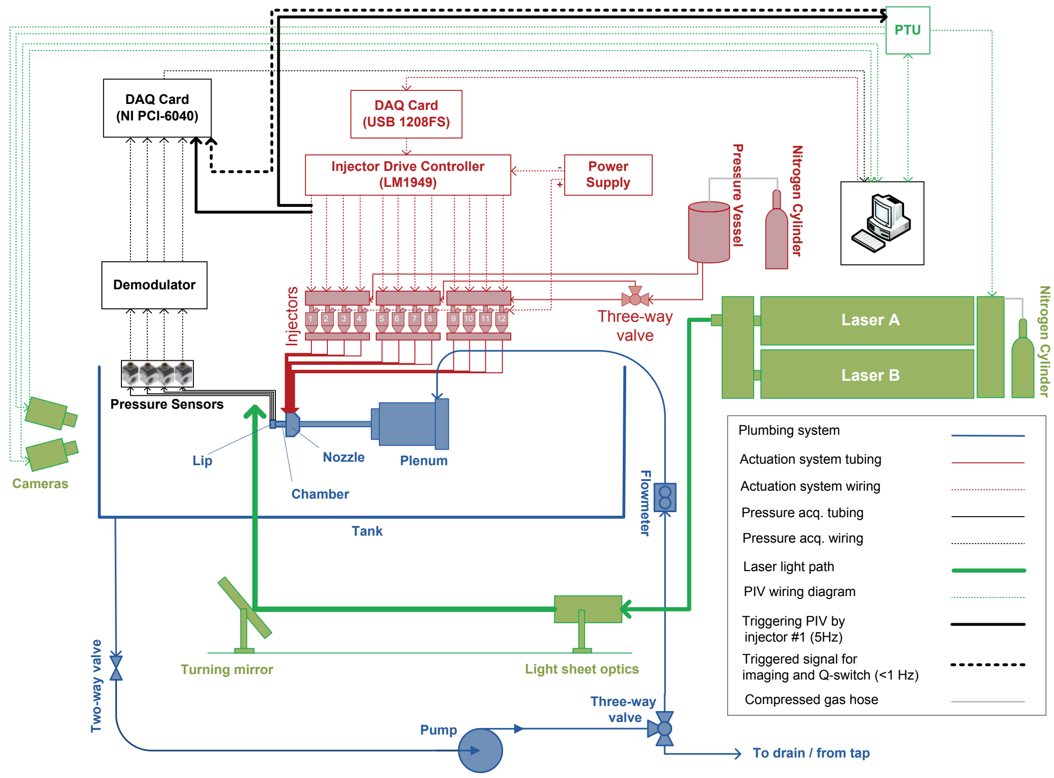

Figure 2.1: Schematic view of the flow facilities, actuation, pressure measurement and S-PIV systems.

also collected by the same DAQ card used for the pressure data acquisition which is shown by a thick black dash line in Figure 2.1.

The flow system is designed to circulate room temperature water as the working fluid ($\rho \simeq 998 \ \frac{\text{kg}}{\text{m}^3}$) in a closed-loop flow system. Water is driven by a progressive cavity pulseless pump (Model 33204, Moyno) and its speed can be controlled manually by a adjustable speed drive (Model ID15H201-E, Baldor). Figure 2.2 shows all components as setup in the lab.

The pump flow rate is calibrated using an acrylic tube rotameter (F-400, Blue White) over a range of ($\simeq$0.1-20 $\frac{\text{lit}}{\text{min}}$) with a maximum working pressure of 150 psi (±5 full scale accuracy). The pump flow rate versus pump rotational speed is shown in Figure 2.3.

After pumping, water passes a three-way valve and is filtered by a filtration unit (GXWH20F, SmartWater, GE), and then goes into the flowmeter (see Figure 2.1). The outlet of flowmeter supplies the inlet flow of the plenum. As shown in Figure 2.4, the plenum and pre-conditioner pipe are upstream of the nozzle and precessing jet in order to provide uniform and low fluctuation inlet conditions for the smooth contraction nozzle which eventually discharges

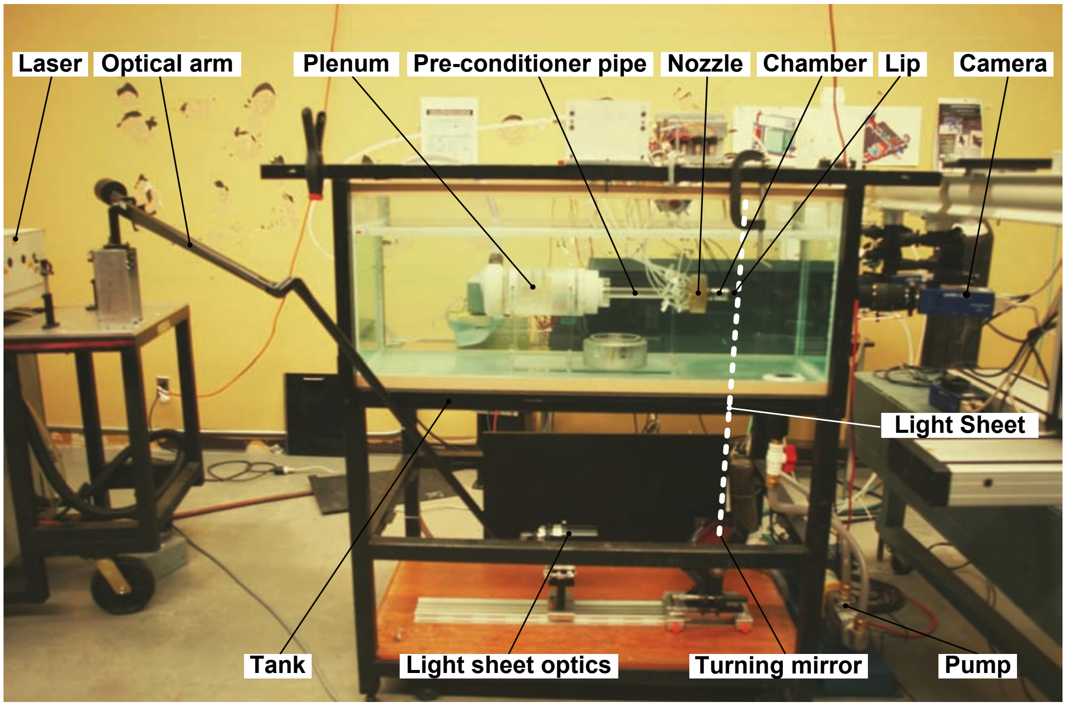

Figure 2.2: Photograph of the experimental setup, illustrating the flow facility and S-PIV system.

through the precessing jet into a tank. The different sections of the plenum are shown in Figure 2.4. A settling chamber, four stages of grid plates and a honeycomb grid are considered to decrease flow fluctuations. The smooth contraction of the plenum and a 20 cm pre-conditioner pipe serves to ensure the inlet flow of the nozzle is uniform [15]. As shown in Figure 2.5, the flow then exits the nozzle into the chamber and then discharges from the chamber over a small lip. For some of the experiments, a center body is present at the chamber exit. Finally the flow exits the chamber into a quiescent 200 l glass tank which has a pump inlet to return the fluid back to the pump.

Two different flow configurations are investigated. First a precessing jet without the center body as shown in Figure 2.6 is investigated. Second, a precessing jet with a center body is studied, as shown in Figure 2.7. The main nozzle, micro-jets and pressure ports are the same for both cases. The only difference is the inclusion of the center body in the second configuration. All important dimensions for each configuration are introduced in Figure 2.6 and Figure 2.7 and the values of these parameters can be found in Table 2.1.

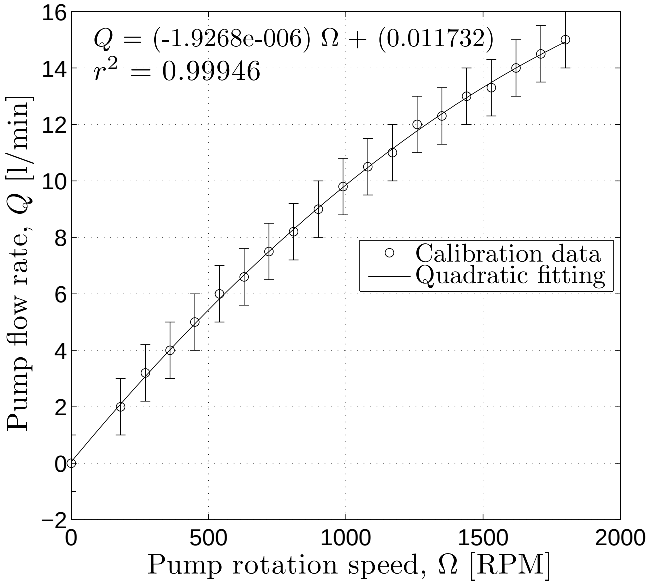

Figure 2.3: Pump calibration, flow rate in terms of rotational speed (RPM); uncertainty is calculated based on ±5 full scale accuracy of the rotameter and is identical for all test points.

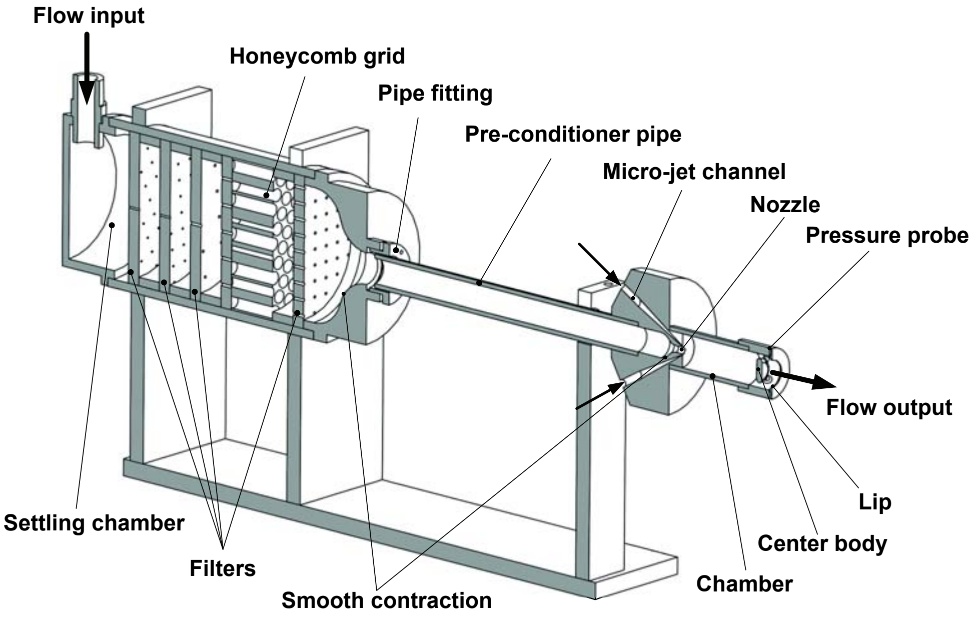

Figure 2.4: Sectioned view of the flow facilities.

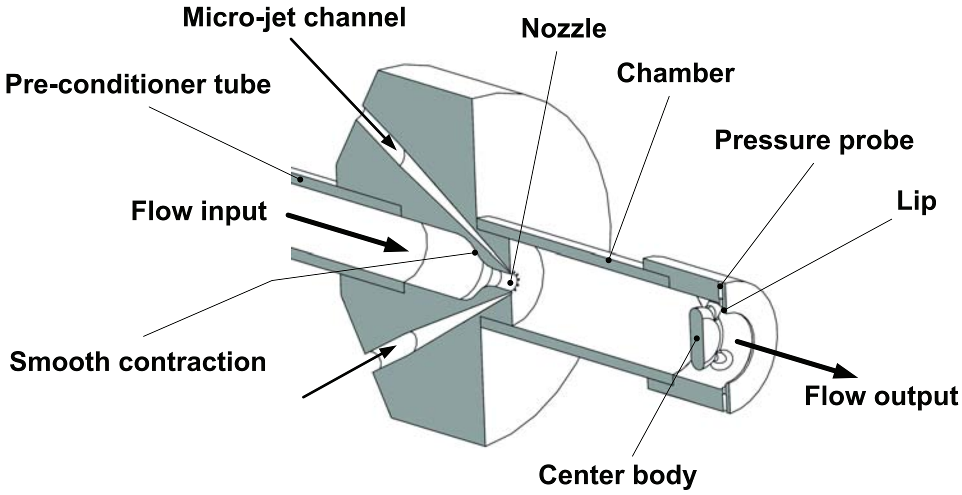

Figure 2.5: Sectioned view of the nozzle setup.

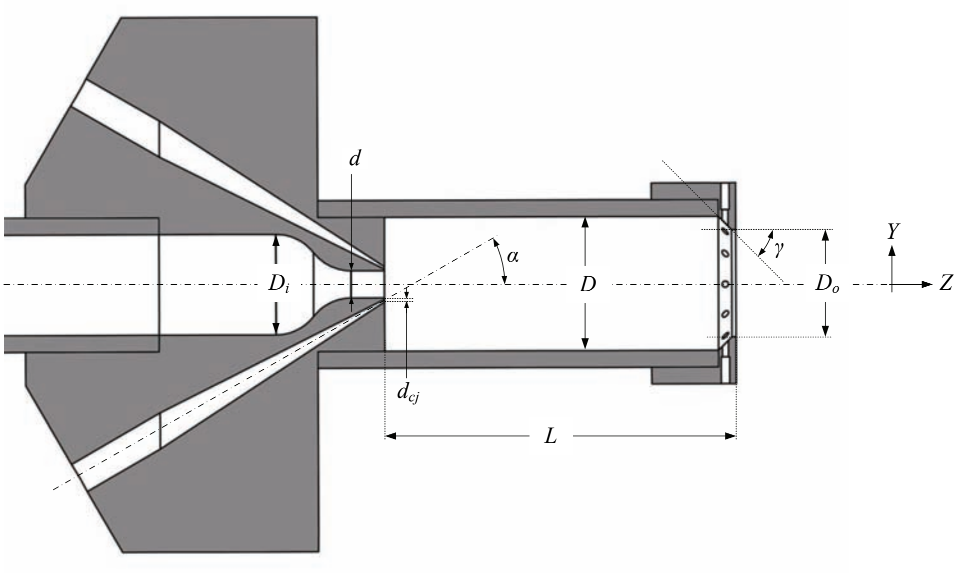

Figure 2.6: Schematic view of the precessing jet with the lip and without the center body, including the injection ports and the pressure probes.

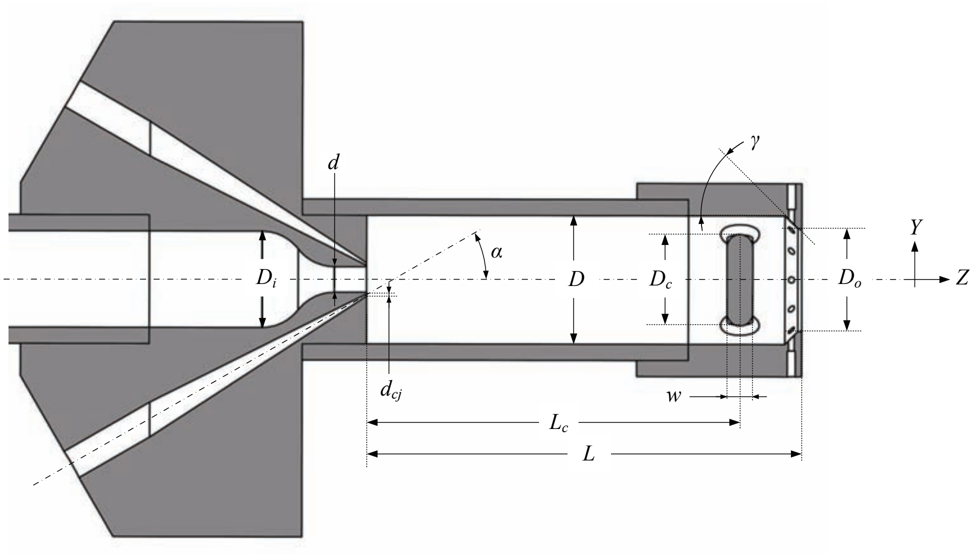

Figure 2.7: Schematic view of the precessing jet with the center body and the lip, including the injection ports and the pressure probes.

Table 2.1: Chamber dimensions

Dimension	**Value**
Pre-conditioner pipe diameter (D_i)	19.05 mm ($\frac{3}{4}$ in)
Chamber inlet diameter (d)	5.08 mm (0.2 in)
Chamber diameter (D)	25.4 mm (1 in)
Chamber length (L)	50.8 mm (2 in), 63.5 mm($2\frac{1}{2}$ in), 69.85 mm ($2\frac{3}{4}$ in), 76.2 mm (3 in), 88.9 mm ($3\frac{1}{2}$ in)
Micro-jet diameter (d_{cj})	0.508 mm (0.02 in)
Micro-jet injection angle (α)	30°
Center body diameter (D_c)	18.034 mm (0.71 in)
Center body thickness (w)	5.08 mm (0.2 in)
Center body distance (L_c)	L - 12.192 mm (0.48 in)
Chamber outlet diameter (D_o)	20.32 mm (0.8 in)
Lip deflection angle (γ)	45°

Due to the complexity of the geometry of the nozzle and lip and integrating twelve micro-jets into the system, they are fabricated using a rapid prototyping (RP) machine (Eden350V, OBJET, with a maximum print resolution of 16 μm) using FullCure720 material. This is a transparent, easy to remove[1] its gel-like support with relatively low water absorption (1.53%, ASTM:D570-98 24 Hr) which makes it an appropriate material to fabricate micro-channels for the application in the water tank. All models are designed using solid modeling tools (SolidWorks 2009, Dassault Systems) which produces files with the extension of "STL" which is an input into RP machine software. All drawings can be found in Appendix A.

Looking at the chamber and lip from the front view (directly into the jet along the Z axis), four pressure probes which are labeled from 1 at the top, increasing in clockwise (CW) direction are shown in Figure 2.8. Four center body mounts are used to hold the center body fixed in its position and are mounted 45° away from the vertical and the horizontal directions (see Figure 2.9(a)). This arrangement is selected to decrease the blocking effect of these bases on the pressure probes (see Figure 2.9(b)).

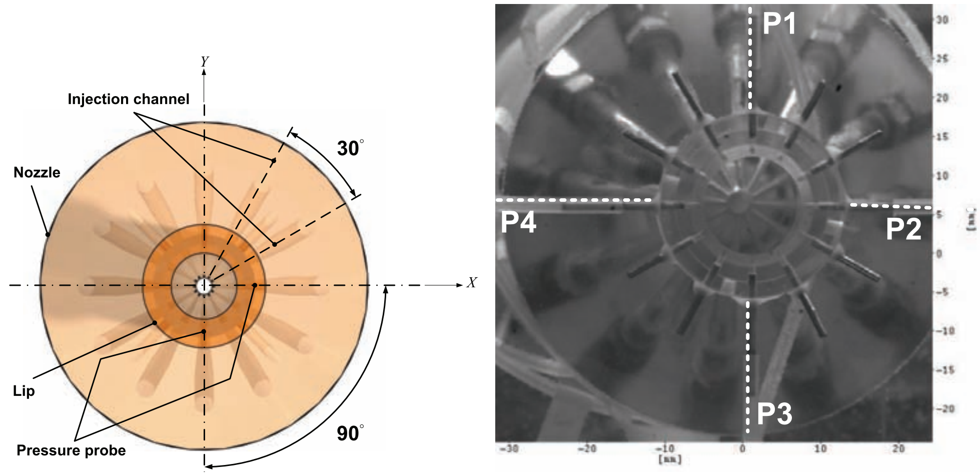

(a) (b)

Figure 2.8: Front view of the nozzle setup and the precessing jet without the center body, (a) illustrating the configuration of the injection ports with respect to each other as well as the pressure probes,(b) photograph of the same view, showing the labeling of the pressure probes.

---

[1] Two materials are used during fabrication by rapid prototyping technique. The part material is the base material of the part and the support material is utilized to assist the fabrication process which is later removed.

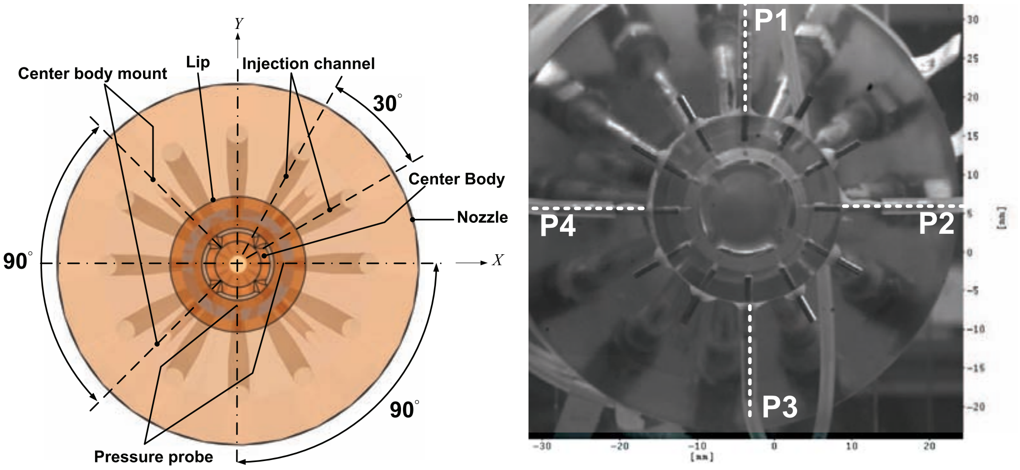

(a) (b)

Figure 2.9: Front view of the nozzle setup and the precessing jet without the center body, (a) illustrating the configuration of the injection ports with respect to each other and the bases of center body as well as the pressure probes,(b) photograph of the same view, showing the labeling of the pressure probes.

2.2 Flow control system

Both passive and active control of a precessing jet are utilized in this study. Passive control is applied in the following two ways: first, the geometry of precessing jet is modified by adding a center body near the chamber exit; second, the chamber length is varied from 50.8 mm(2 in) to 88.9 mm (3.5 in). Active control is performed using twelve micro-jets (with a diameter of 0.508 mm (0.02 in) around the main jet as shown in Figure 2.5. The micro-jets inject water through twelve micro channels and are fed through $\frac{1}{6}''$ PE (Polyethylene) tubes using twelve on/off injectors. The twelve on/off injectors are fuel injectors (INJL48, Disc High Impedance (Coil Resistance 12.2 Ω), Standard Motor Products) which are alternative fuel compatible to resist against rusting. The nominal flow rate of the fuel injectors is 492 $\frac{\mathrm{ml}}{\mathrm{min}}$ (48 $\frac{\mathrm{lb}}{\mathrm{hr}}$) for a pressure difference of 689 kPa (100 psi) across the injector. The pressure is maintained by a upstream pressure vessel (GE10P06CAG, 36 L, Smart Water Heater, GE) supplied by a nitrogen cylinder to keep the vessel pressure constant during injection.

The injectors are controlled by a custom injector driver circuit (LM1949) which receives signals from a DAQ card (USB 1208FS, Measurement Computing Corporation). Although the maximum sample rate of this DAQ card is 50 kHz, the digital output rate is limited by the operating software (CVI, Lab-Windows, National Instruments) to less than 20 Hz. A detailed description of the custom software graphical interface developed for this study is given in Appendix B. A photograph of configuration of the actuation system elements in the lab is given in Figure 2.10.

The range of values for passive and active control is given in Table 2.2. This results in a 7(Re)×5(Chamber length)×2(CW/CCW)×10(f)×2(CB/no CB) matrix of test conditions (=1400 test points) which are experimentally measured in this work using pressure measurement (note: the S-PIV measurements are taken in addition to the above described measurements but only for a small subset of these measurements).

Table 2.2: The range used for independent variables

Independent variable	**Value**
Reynolds number (×1000)	0, 14, 27, 38, 47, 55 and 62
Passive control	with CB and without CB
$\frac{L}{D}$	2, 2.5, 2.75, 3, 3.5
Actuation frequency	1 to 10 Hz (increment:1 Hz)
Actuation direction	CW and CCW

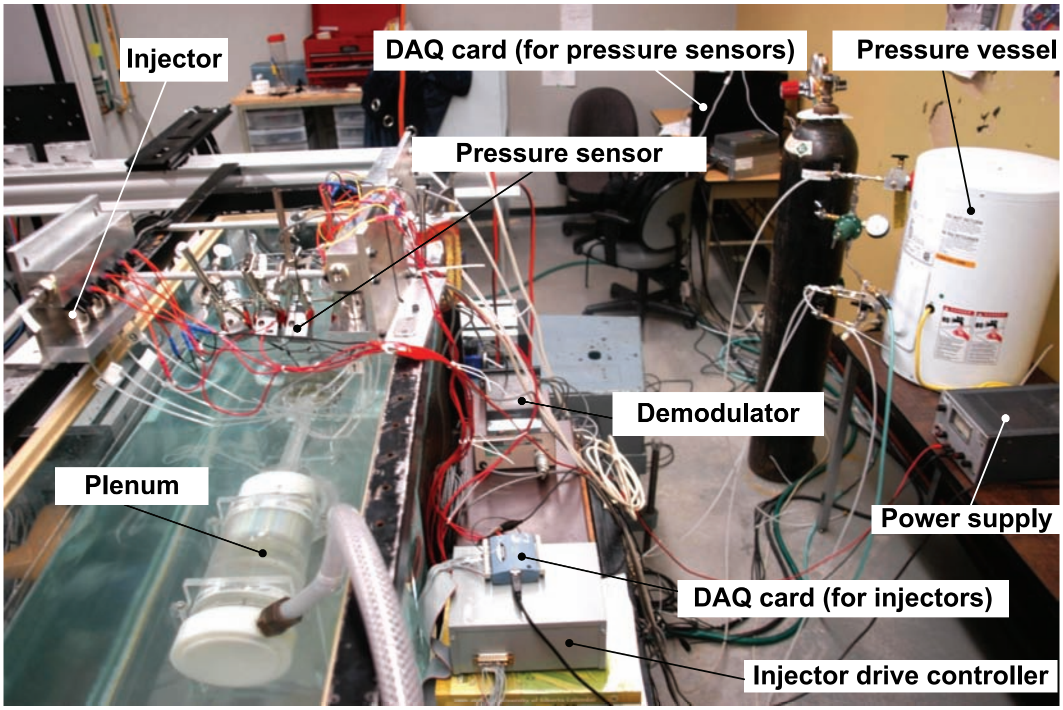

Figure 2.10: Photograph of the experimental setup, illustrating the actuation and the pressure measurement system.

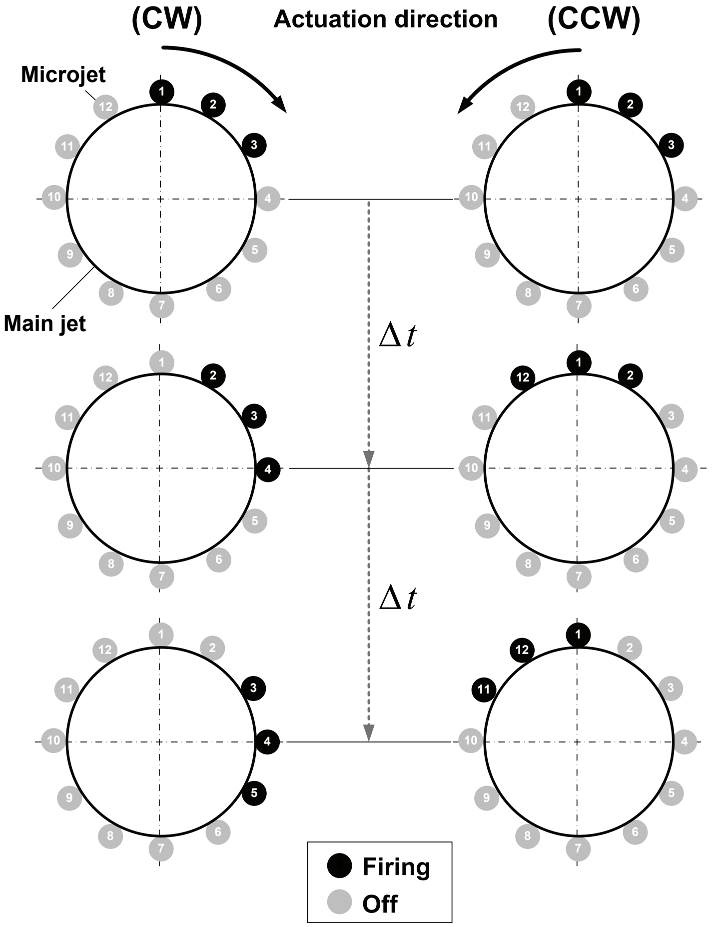

Figure 2.11: The firing pattern of the injectors in CW and CCW actuation with three injectors firing simultaneously (the direction of the flow, i.e. the positive Z axis, is out of the page).

With twelve micro-jet actuators, there are many combinations of which actuators can be turned on. Using three micro-jets simultaneously is found to be effective on the precessing jet and so this pattern is used in this study and is shown in Figure 2.11. The injectors are numbered from 1 starting on the positive Y axis and increasing in CW direction. In this pattern, three successive injectors (n=3, where n is the number of simultaneously injectors which are on) are always firing and this pattern rotates with a given frequency (f). So the successive pattern (of firing injectors) for CW actuation is:

...,1-2-3, 2-3-4, 4-5-6 ...

and for CCW actuation:

...,1-2-3, 12-1-2, 11-12-1 ...

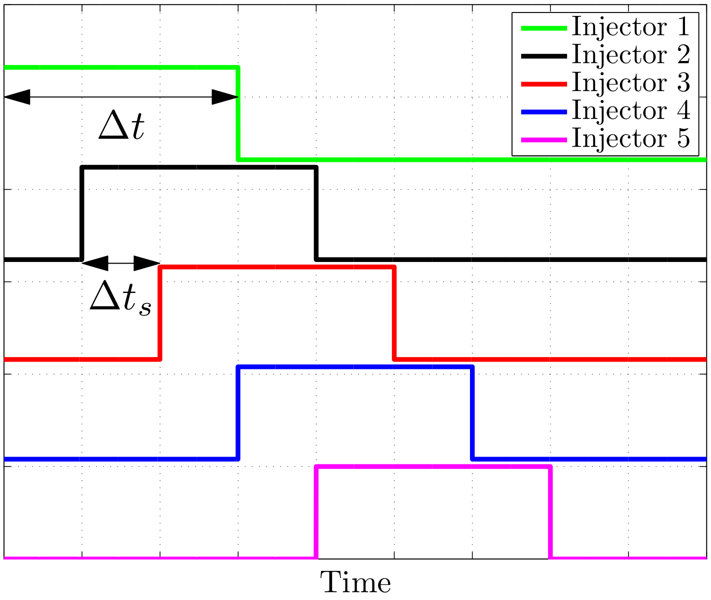

Figure 2.12: The definition of opening time (Δt) and switching time (Δt_s) for successive injectors' command signals.

while the rest of the injectors are turned off. Looking at Figure 2.12, the opening time (pulse width) of the injectors is given by:

$$\Delta t = \frac{n}{12f} \tag{2.1}$$

and the switching time between the injectors is:

$$\Delta t_s = \frac{1}{12f} \tag{2.2}$$

The opening time varies between 25 ms $\leq \Delta_t \leq$ 0.25 s for $1 \leq f \leq 10$ when $n = 3$.

Each of the twelve fuel injectors are calibrated for volume flow rate with this pattern using a 80 ml beaker and a stop watch. Figure 2.13(a) shows the result of the calibration for CW actuation which gives an average flow rate of ($446 \pm 25\ \frac{\text{ml}}{\text{min}}$) and Figure 2.13(b) gives the injectors flow rate for CCW actuation of ($445 \pm 27\ \frac{\text{ml}}{\text{min}}$). To evaluate the strength of actuation comparing to the main flow two different parameters are introduced in the literature. The most common parameter is flow rate ratio defined as:

$$r_m = \frac{\sum_{i=0}^{n} \dot{m}_{cj,i}}{\dot{m}} \tag{2.3}$$

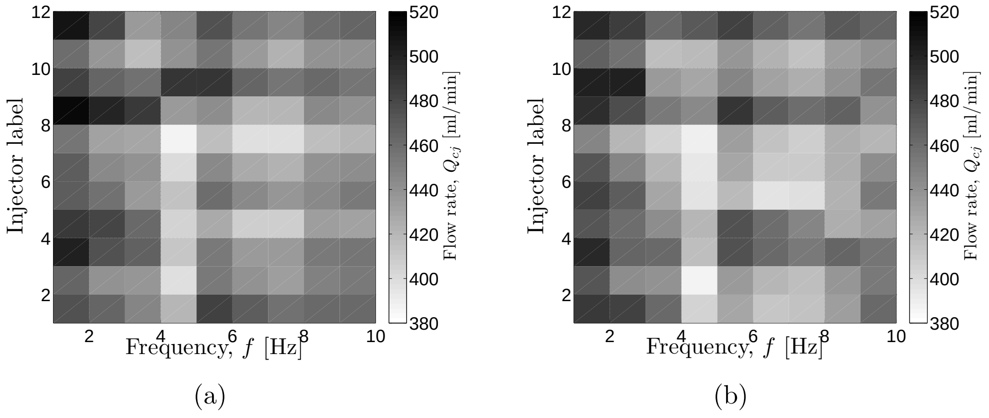

(a) (b)

Figure 2.13: Calibration of the twelve injectors versus actuation frequency at (a) CW, (b) CCW.

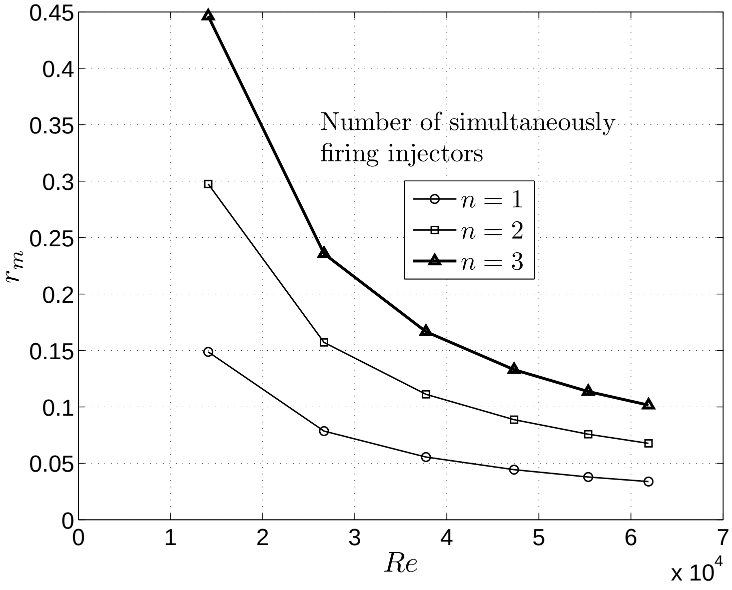

Figure 2.14: The mass flow rate ratio of the micro-jets to the main jet in terms of Reynolds number of number and the number of simultaneously firing injectors during actuation.

Since the firing pattern shown in Figure 2.11 has three actuators on all the time, the result is always a constant flow rate. As shown in Figure 2.14, the ratio of the injection to the main jet flow rate varies between $0.1 \le r_m \le 0.45$ for $14,000 \le Re \le 62,000$.

Another parameter which is used to compare the strength of actuation is momentum coefficient (C_μ) which is defined by Equation 2.4:

$$C_\mu = \frac{\sum_{i=0}^{n} U_{c_{j,i}}^2 d_{c_{j,i}}^2}{\frac{1}{2} U^2 d^2} \tag{2.4}$$

Figure 2.15 shows the variation of momentum coefficient with respect to Reynolds number for three simultaneously firing injectors. This ratio decreases from $C_\mu \simeq 13$ at low Reynolds number ($Re = 14,000$) to $C_\mu \simeq 0.7$ for high Reynolds number ($Re = 62,000$).

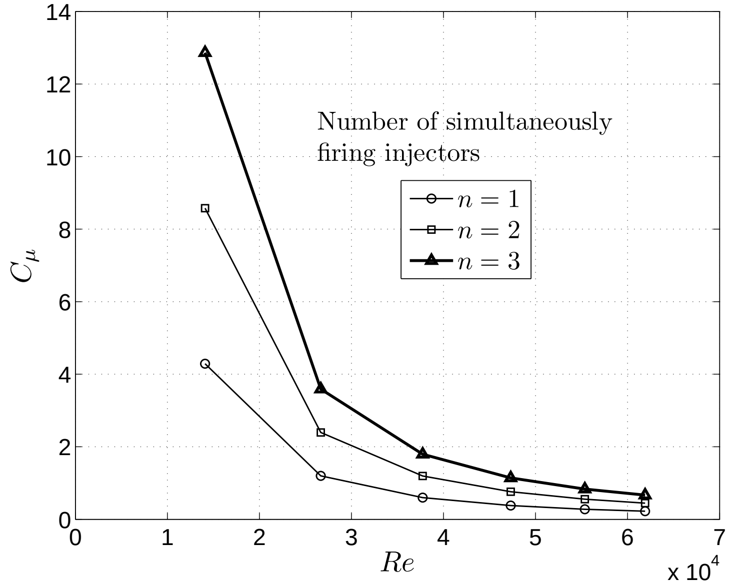

Figure 2.15: The momentum coefficient of the micro-jets to the main jet in terms of Reynolds number and the number of simultaneously firing injectors during actuation.

As discussed in Chapter 1, the dimensionless parameter which is used to study the behavior of the precessing jet is Strouhal number which is the dimensionless frequency of either the precessing jet or the actuation. Actuation Strouhal number can be defined as:

$$St = \frac{f.d}{U_i} \tag{2.5}$$

where U_i is the average axial velocity at the nozzle exit and d is the nozzle diameter (= 5.08 mm (0.2 in)) and f is the frequency of actuation (i.e. rotation of actuation pattern). All test points in this research are plotted with frequency versus Reynolds number and corresponding Strouhal number in Figure 2.16. As shown in Figure 2.16, all experiments are designed to be conducted around St of the precessing jet which is reported in the literature~ 0.003 [20].

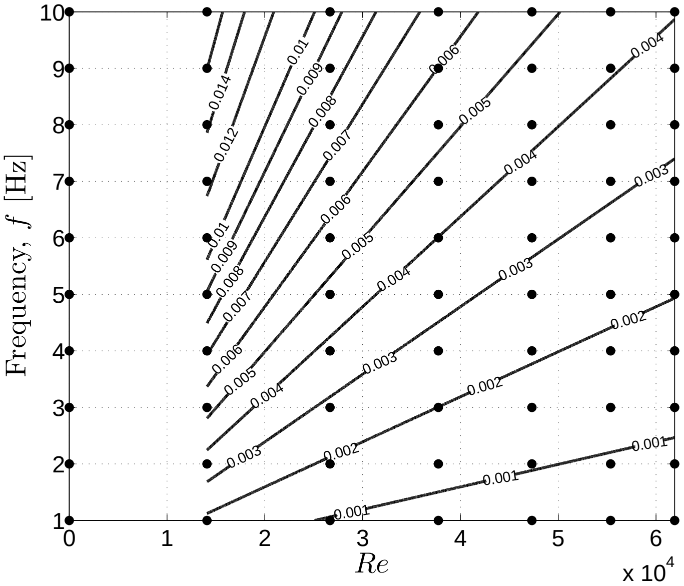

Figure 2.16: Measured test points in Reynolds number and frequency plane; the test points in this plane are conducted twenty times (=5 × 2 × 2), for all $\frac{L}{D}$ (5), with and without center body (2) and actuation directions (CW and CW) (2), respectively.

2.3 Pressure measurement

In order to study the behavior of this complex fluidic system under control as well as to evaluate the actuation effectiveness, the flow is investigated using two different measurement techniques. Pressure measurement is able to monitor the transient behavior of this flow while S-PIV provides detailed information about the velocity field. Pressure data has the potential to be used as a feedback signal in order to develop future closed-loop control. However, characterizing the flow field at the chamber exit using only four discrete pressure measurements needs to be verified by detailed S-PIV velocity vector field to make sure the results of pressure processing corresponds to the actual precessing jet behavior.

A precessing jet has been studied using pressure measurement with several pressure probes located in different points [9]. To observe the bi-stable behavior of the jet, the probes are located near the exit plane of the chamber. Therefore, in this research, the probes are mounted on the body of the lip at the exit plane of the chamber (see Figure 2.17). These probes are located with 90° difference with respect to each other while the probe 1 is located at the top position as shown in Figure 2.8(b) and 2.9(b).

Each of the probes are connected through $\frac{1}{16}''$ PE tubes to pressure sensors

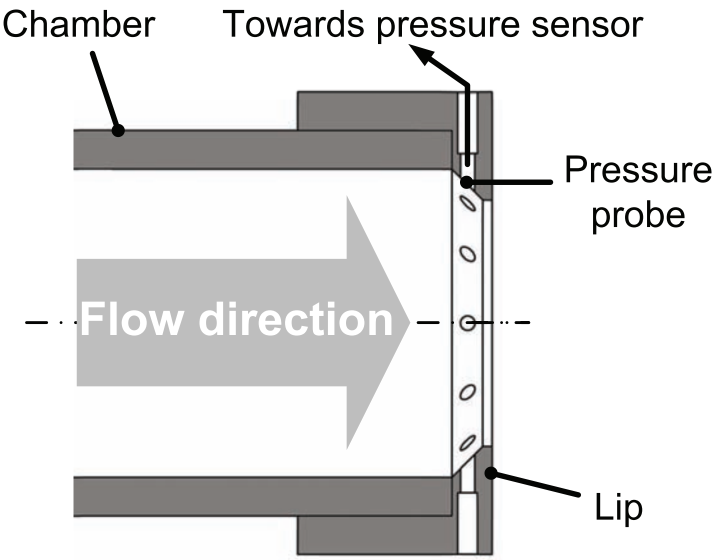

Figure 2.17: Configuration of the pressure probes on the lip.

(DP15, Validyne) with a diaphragm dash range number of 32 (2 psi), and a sampling rate of 3 kHz and ±25% FS accuracy. A NI DAQ card (PCI-MIO-16E-4, now referred as NI PCI-6040) acquires data from the pressure sensors. Taking the natural frequency of the precessing jet to be in the range of 4-7 Hz and the frequency associated with switching time up to 120 Hz ($\Delta t_s^{-1} = 12 \times 10 s^{-1}$) into account, a sample rate of 1 kHz for the acquisition of pressure data is chosen.

A pressure calibrator (DPI610, Omega) with a maximum pressure of 207 kPa (30 psig) and a resolution of 6.89 Pa (0.001 psi) is employed to calibrate the four Validyne pressure sensors. As shown in Figure 2.18, an increment of 1.4 kPa (0.2 psi) is used for the calibration of all pressure sensors in the range shown in Table C.2. In order to use this calibration, straight lines are fitted on the calibration data by linear regression with r^2 values larger than 0.999. Figure 2.18 shows the calibration result for each of the sensors and the slope of calibration curves are compared in Figure 2.19. The calibration is repeated from the negative pressure to the positive values to make sure no hysteresis is present which sometimes results in different behavior in two directions, so it is highly recommended to calibrate the sensors in both directions.

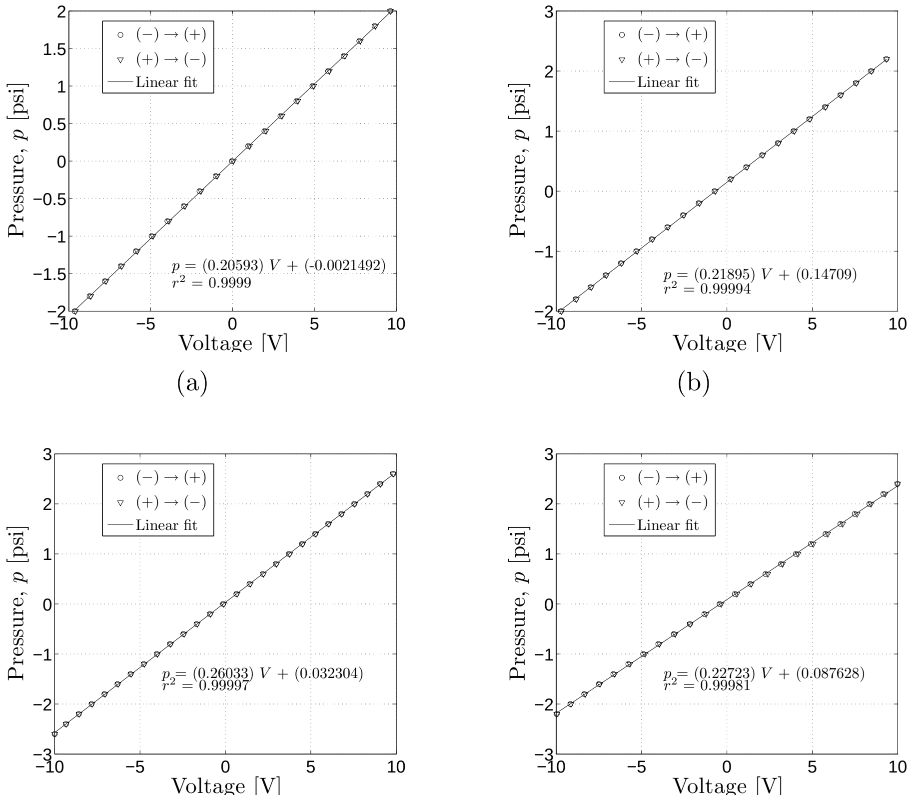

(a) (b)

(c) (d)

Figure 2.18: Calibration of the pressure sensor (a) 1, (b) 2, (c) 3, (d)4. (○: calibration from negative to positive pressure, ▽: calibration from positive to negative pressure).

Table 2.3: Linear fitting on the calibration data of the pressure sensors in psi as a function of voltage

Sensor	Linear regression, p psi	r^2	[Min.,Max] pressure psi
1	0.205931 v−0.002149	0.999	[-2.0,+2.0]
2	0.218945 v+0.147093	0.999	[-2.0,+2.2]
3	0.260327 v+0.032304	0.999	[-2.6,+2.6]
4	0.227227 v+0.087628	0.999	[-2.2,+2.4]

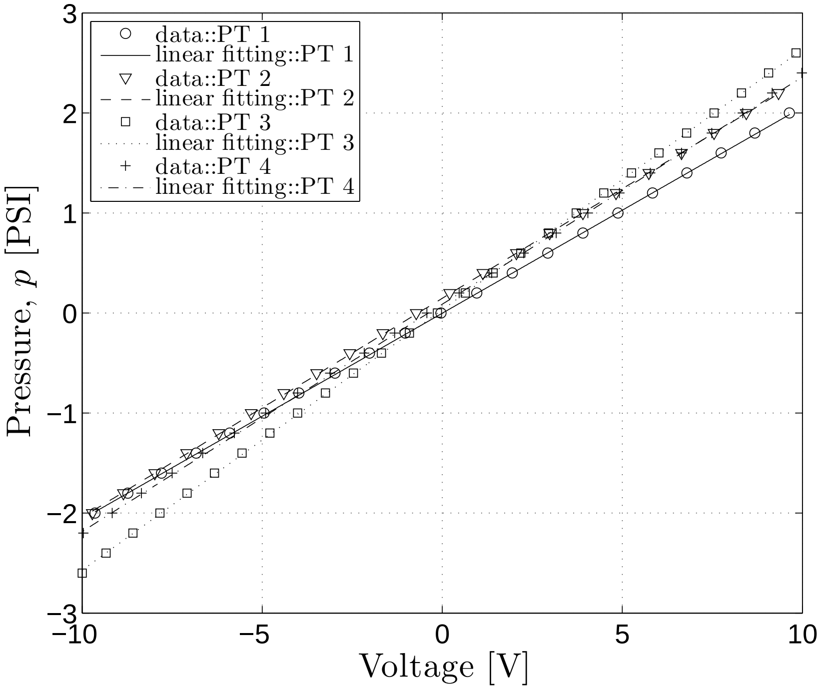

Figure 2.19: Comparison of the calibration curves for four pressure sensors.

2.4 Stereoscopic Particle Image Velocimetry (S-PIV)

Detailed flow behavior of the precessing jet can be revealed by looking at its velocity vector field. Particle Image Velocimetry makes it possible to study the flow through velocity vector field. Due to the three dimensionality of the precessing jet, S-PIV is chosen to obtain three components of the velocity field in a two dimensional plane downstream of the chamber exit. This section provides detailed information about S-PIV setup and image processing required to obtain the velocity vector field.

Figure 2.20 demonstrates the S-PIV procedure. In this technique, two cameras are employed to take two snapshots (usually called a frame) from the flow (seeded with particles) within a short controlled time interval. Then these two frames are cross correlated inside a small region (which contains a few particles, so-called interrogation window). The highest peak of the cross correlation corresponds to the overall displacement of the particles at the given interval. Having the displacement and the time interval, in-plane velocity vector can be calculated inside the selected interrogation window. Taking into account that these vectors are from cameras which look at the flow in different directions, the out-of-plane velocity component can be found by projection. More details about S-PIV and its procedure can be found in [39].

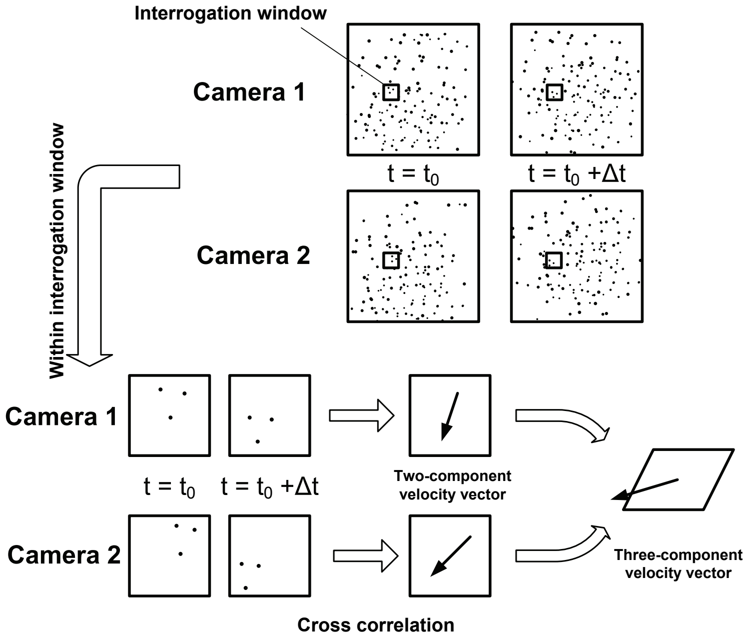

Figure 2.20: Procedure of velocity vector field computation in S-PIV.

2.4.1 S-PIV setup, calibration and self calibration

The light sheet created for S-PIV is usually aligned with a plane on which the maximum velocity components are located and there is no strong out-of-plane velocity. However, the plane on which the three dimensional large scale structure of the precessing jet appears is the chamber exit plane, which is perpendicular to the jet flow. The out-of-plane velocity (axial velocity) on this plane is the largest velocity component and is largely responsible for the dynamic pressure captured by the pressure sensors in the probes on the chamber lip. Therefore, unlike the conventional S-PIV setup, a camera arrangement shown in Figure 2.21 is used to capture the phenomena happening in the chamber exit plane. A similar arrangement has been used by [40] to study laminar, transient and turbulent pipe flow using S-PIV. Figure 2.22 illustrates the S-PIV components and their arrangements with respect to the tank and the plenum. A photograph of all S-PIV components in the laboratory can be found in Figure 2.2.

The flow is initially seeded by 18±2 μm hollow glass non-porous spheres (60P18, Potters Industries) with a density of 0.6±0.05 $\frac{\text{gr}}{\text{ml}}$. Obtaining five particles inside the finest interrogation window is a rough estimate for the amount of particles that should be added. To illuminate the particles, a dual-cavity Nd:YAG laser (PIV-400-10, Spectra Physics) is used. This laser delivers up to 400 $\frac{\text{mJ}}{\text{pulse}}$ at a frequency-doubled output wavelength of 532 nm (green light) and an operating frequency (repetition rate) of 10 Hz. An optical arm (Haas Laser Technologies Inc.)(see Figure 2.2) serves to transfer the laser beam to optics (LaVision GmbH) by which the thickness and the width of the laser light sheet can be adjusted. The light sheet generated through this optics turns upwards by a turning mirror and in this way illuminates a sheet right after the chamber exit plane; Figure 2.2 and Figure 2.22 show the light sheet trajectory through all optical devices. As shown in Figure 2.21, images are collected using two LaVision FlowMaster cameras (Imager Pro X 4M, LaVision GmbH) which are mounted on a three dimensional traverse (Feed Axis LES5, IselGermany). These cameras are high-resolution (2048 × 2048 px), with a dynamic range of 14-bit, double-frame CCD with an imaging frequency at full frame of 14.7 fps. The cameras equipped with a 105 mm lens (f/2.8 EX DG Macro, SIGMA) with Scheimpflug adapters. The cameras are located at a downstream distance from the lip of 0.32 m and looking at the flow at 16° (camera 1) and 14° (camera 2) angles with respect to the chamber axis (see Figure 2.23-top view).

The region of interest in this research is limited to the near field of the lip exit to observe the behavior of the flow as discharges from the chamber into the environment. Therefore, each camera looks at the flow only through the field of view shown in Figure 2.24.

Figure 2.23 (side view) illustrates the relative location of the plenum and

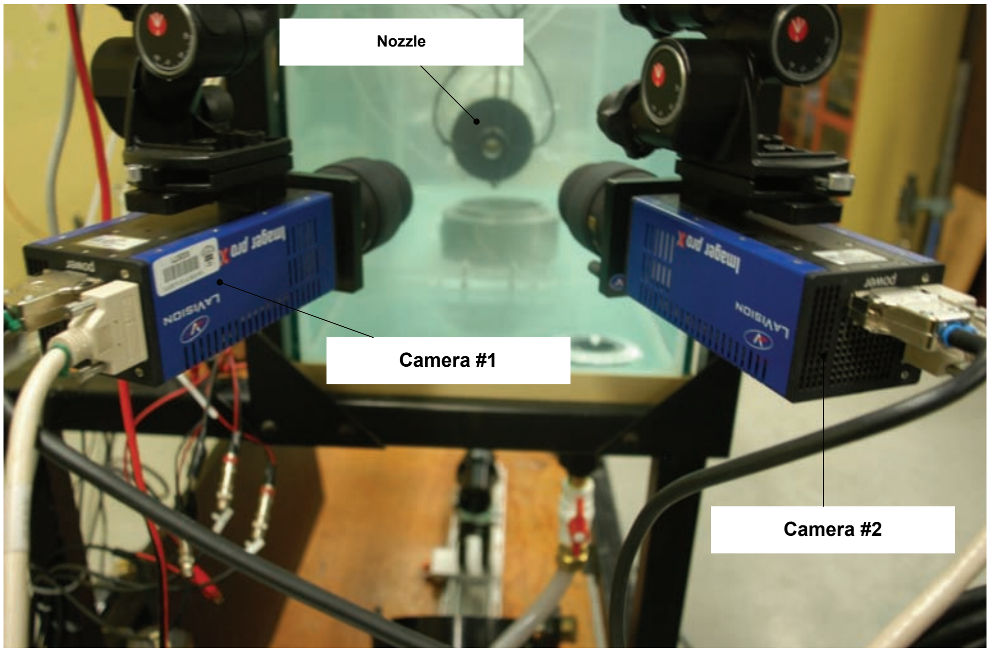

Figure 2.21: Configuration of the cameras with respect to each other and the nozzle.

the nozzle with respect to the tank and also the exact location of the light sheet with respect to the lip (blown up view). The plenum is positioned in the middle of the tank width such that the lip is 46d away from the right side of the tank. Due to the rapid decay of the precessing jet in the downstream, this distance is far enough to ensure no impinging jet effect appears [10]. To avoid the laser sheet reflection by the chamber and the chamber lip, a small gap (~4 mm) is set for the light sheet to the exit plane of the lip.

The most critical parameters in S-PIV design, particularly when it comes to strong out-of-plane velocity component, are light sheet thickness and time step between laser flashes. Selection of these two parameters should satisfy the following two criteria: first, the in-plane displacement of particles between two snapshots should be one-quarter of the interrogation window size; second, the out-of-plane particle displacement between two laser flashes should be one-quarter of the light sheet thickness. Using a thinner light sheet or a longer time step results in particles escaping from the illumination region which in turn creates missing (blank) spaces in final velocity vector field. Therefore, the procedure taken in this research is to begin with relatively large time step and decrease it until a few (less than 1 %) blank regions appear in the final vector field. This is a practical way to find the threshold time step for a given light sheet thickness. Using a thickness of 4 mm for the light sheet, the optimal time step is found to be 80 μs, for low Reynolds number tests and 55 μs for

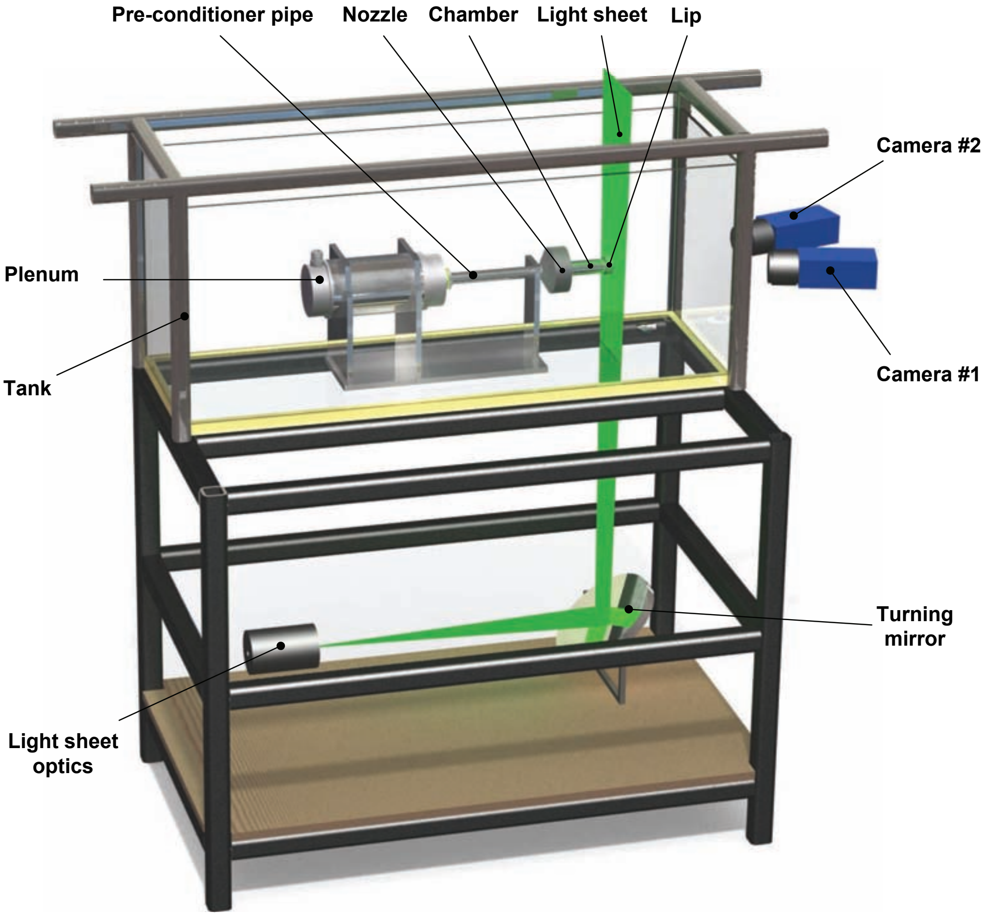

Figure 2.22: S-PIV components.

high Reynolds number tests. An alternative way to find the optimal time step for a given light sheet thickness can be found in [15].

A 3-D (two level) calibration plate with a dimension of 106×106×12 (Target Type 11, LaVision GmbH) is mounted in the front of the lip to calibrate the cameras. Initially, a pinhole model is applied to calculate the cameras physical parameters and then polygon calibration (3$^{\text{rd}}$ order polynomial) is done as the more robust calibration mapping due to the strong distortion in this arrangement. The average deviation of the dewarped mark positions on the target is around 0.3 px for both cameras; using self-calibration, this value decreases to less than 0.05 px. The detail procedure of self-calibration for S-PIV can be found in [41].

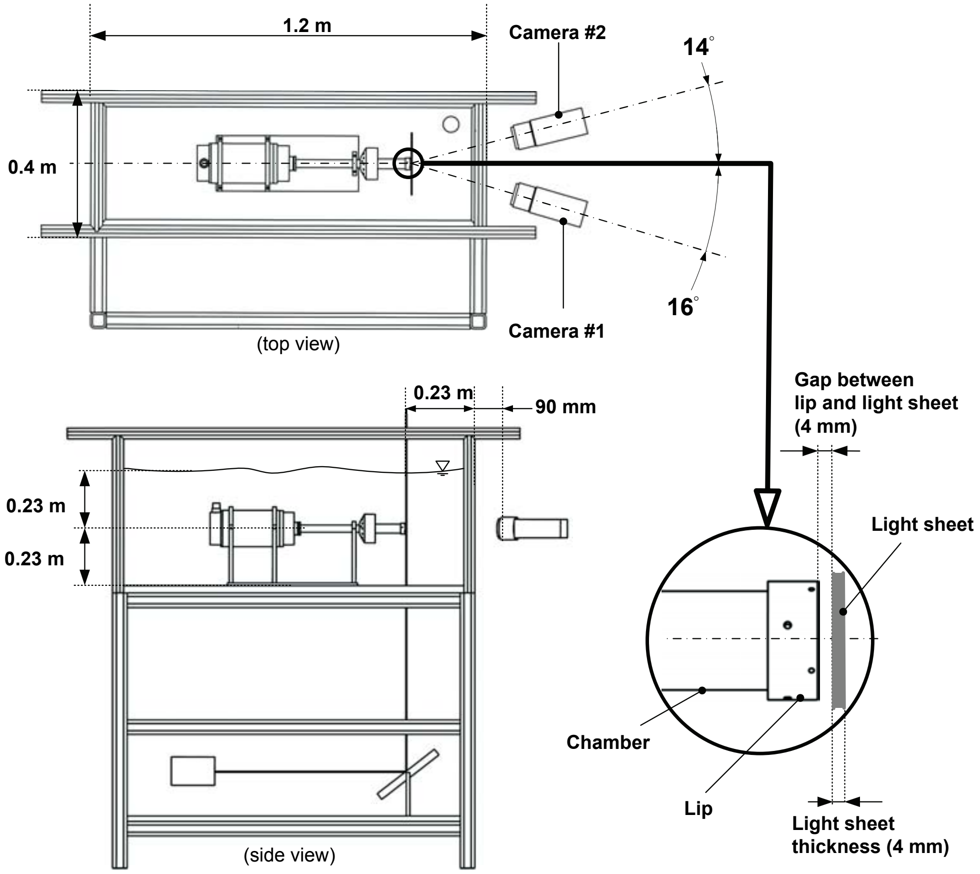

Figure 2.23: S-PIV experimental setup.

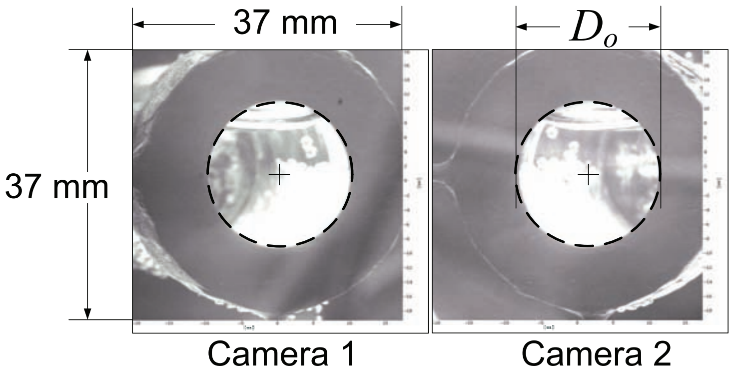

Figure 2.24: Field of view; the dash line shows the boundaries of the outlet diameter of the chamber (D_o=20.32 mm (0.8 in)).

2.4.2 S-PIV velocity vector field computation

Velocity vector field computation consists of image pre-processing, vector field correlation and vector field post-processing. A detailed description of all these procedures is summarized in Figure 2.25.

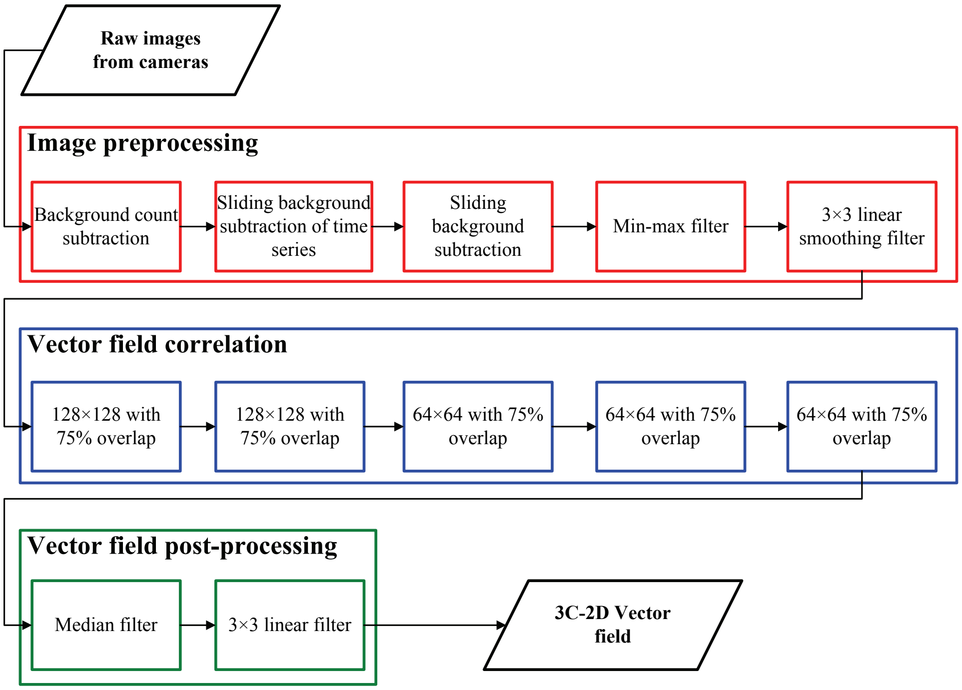

Figure 2.25: S-PIV processing algorithm (reproduced from [15]) .

Background count subtraction compares the intensity of each image over the all images and subtracts their minimums from each of them. In sliding background of time series (which is a different function from the background count subtraction in the software), the same procedure is taken for a limited number of successive images. Using these filters, the background noise over different images are removed; sliding background subtraction subtracts the minimum intensity of the surrounding pixels of each pixel to remove any high intensity reflection or noise in the background of each image. Min/Max filter normalizes the light intensity over the whole images and eventually a 3×3 linear smoothing filter is used to make all particles circle and big enough to be captured through cross correlation. The detailed description of each processing can be found in [15].

Two-pass cross correlation with large window size (128×128 px) with 75% overlap and three-pass with a small window size of (64×64 px) with 75% overlap are taken to calculate velocity vectors. Cross correlation process begins with a large window size (128 px) in order to get the main stream of the flow over the interrogation window; then the vector calculated over these large windows is used as the initial value for the small window size correlations (64 px). The velocity vector field is further processed with a median filter which replaces each vector with the median value of all surrounding vectors (with some conditions) and finally the vector field is smoothed with a 3×3 smoothing filter. All these pre-processing, processing and post-processing steps are done using a commercial code (DaVis 7.4, LaVision GmbH). By extracting the velocity vector field from DaVis software, further processes are carried out using MATALB R2009a. In Appendix C, all MATLAB codes developed in this research are described. The obtained velocity vector field contains three velocity components, namely (U, V, W) which are used in the following chapters to extract more information about the instability of the fluidic system.

Chapter 3

Pressure data analysis (triggering with single injector)

Active flow control requires that the actuation method produces a desired response in the flow. It is thus essential to quantify the effect of the micro-jet actuation on the precessing jet. To measure the flow, four pressure sensors at the chamber exit are used. This chapter describes different methods by which pressure signals are treated to extract information about the flow behavior. Sensitivity analysis of the flow and actuation parameters, in order to experimentally determine a phase diagram illustrating the flow states over the entire range of independent variables, is examined. This chapter begins with description of pressure data preprocessing, then three methods (successful or unsuccessful) to analyze the pressure data are introduced, and finally the influence of different parameters on the flow behavior are investigated.

3.1 Preprocessing of pressure data

The raw data collected with pressure sensors is time series of the voltages generated at four pressure taps located on the periphery of the chamber lip with 90° seperation. As shown in Figure 3.1, data is collected in two stages: when the pump is off, the sensors are only subject to hydrostatic pressure; then with the pump running, a portion of dynamic pressure corresponding to the velocity component perpendicular to the tap interface, shown by $\overrightarrow{V_n}$ in Figure 3.2, is added to hydrodynamic pressure. Figure 3.3 illustrates the position of pressure sensors and their probes with respect to free surface. Having atmospheric pressure at the free surface, pressure can be written as:

$$p_0^c = p_{atm.} - \rho g h_0 \tag{3.1}$$

where p_0^c is the no flow pressure collected before running the pump and h_0 is the height of the mounted pressure sensor with respect of the level of water in

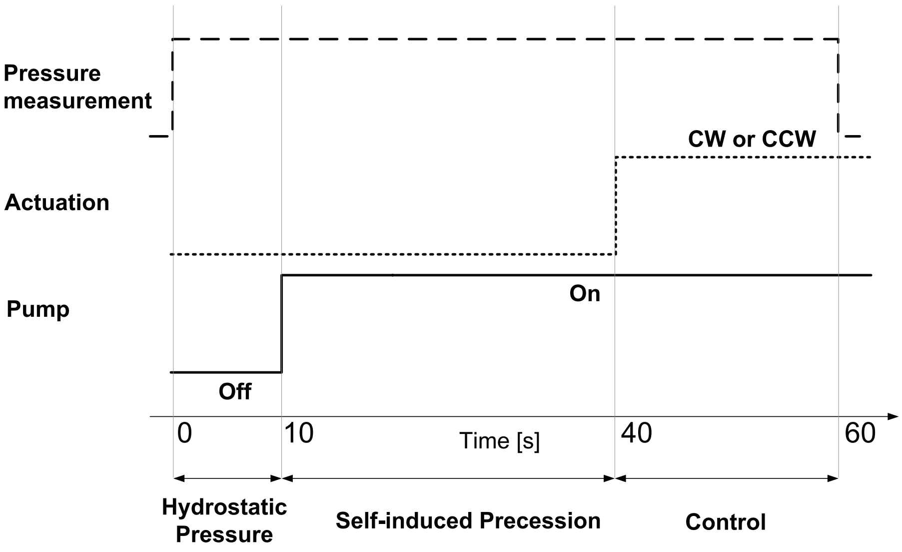

Figure 3.1: Timeline for pump, pressure measurement and actuation operations used for the all test conditions.

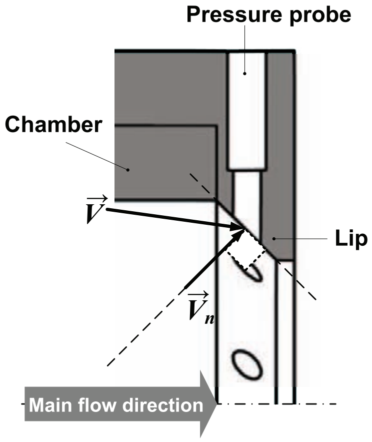

Figure 3.2: Configuration of the pressure probe with respect to the flow (for a larger view see Figure 2.17).

the tank as shown in Figure 3.3. To investigate the transient behavior of the precessing jet, no flow pressure is subtracted from the portion of total pressure using:

$$p = p^c - p^c_0 \tag{3.2}$$

where p^c is the measured pressure and p is the portion of dynamic pressure. Since the order of fluidic precession phenomenon in this study is less than 10 Hz, all pressure data are filtered by low pass filter using 100 Hz to re-

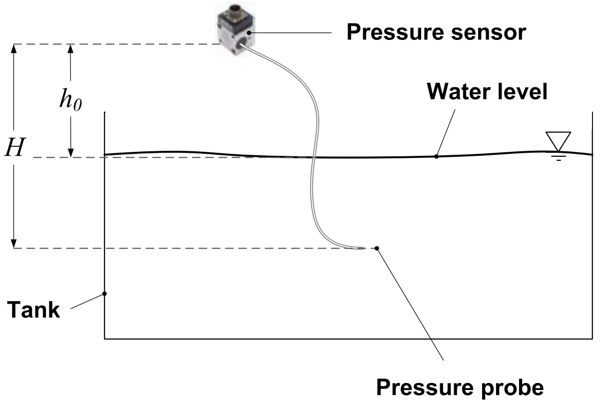

Figure 3.3: The location of pressure sensor and its probe with respect to the water level in the tank.

move high frequency noise. Figure 3.1 illustrates the experimental procedure conducted to collect all data at 1400 test points introduced in Table 2.2 in Chapter 2.

Figure 3.4(a) and Figure 3.4(b) show an example of the preprocessed pressure data (no flow pressure subtracting and filtering) collected by the pressure sensor 2 before and with actuation, respectively. The stabilizing effect of the actuation can be observed by comparing Figure 3.4(a) and Figure 3.4(b).

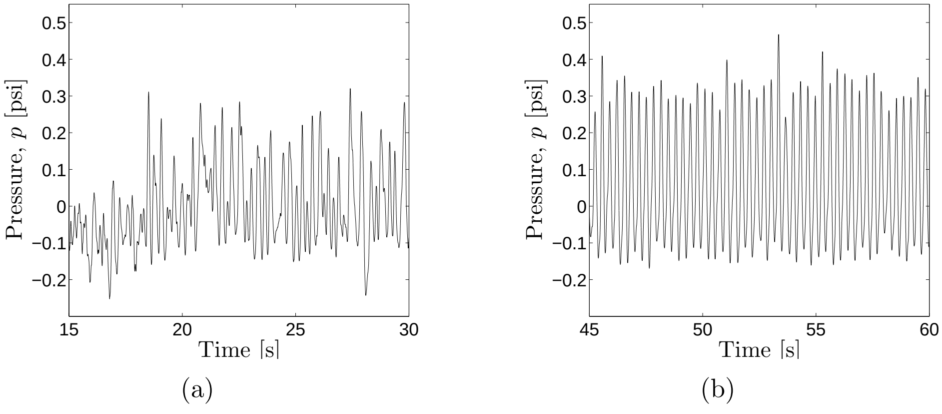

(a) (b)

Figure 3.4: An example of pressure data collected by the pressure sensor 2, after subtracting no flow pressure and filtering for a chamber without the center body at $\frac{L}{D} = 2.5$ and $Re = 47,000$ with (a) no actuation (b) CW actuation of $f = 3$ Hz.

3.2 Fast Fourier Transform analysis

FFT analysis is a standard analysis method for a phenomenon with a periodic behavior. As the first step, the mean value of each signal is subtracted. Then discrete Fourier transform of all four dynamic pressure (p) signals using FFT algorithm is calculated without windowing. Finally, the modulus of discrete Fourier transform is studied to find the buried frequencies in the system.

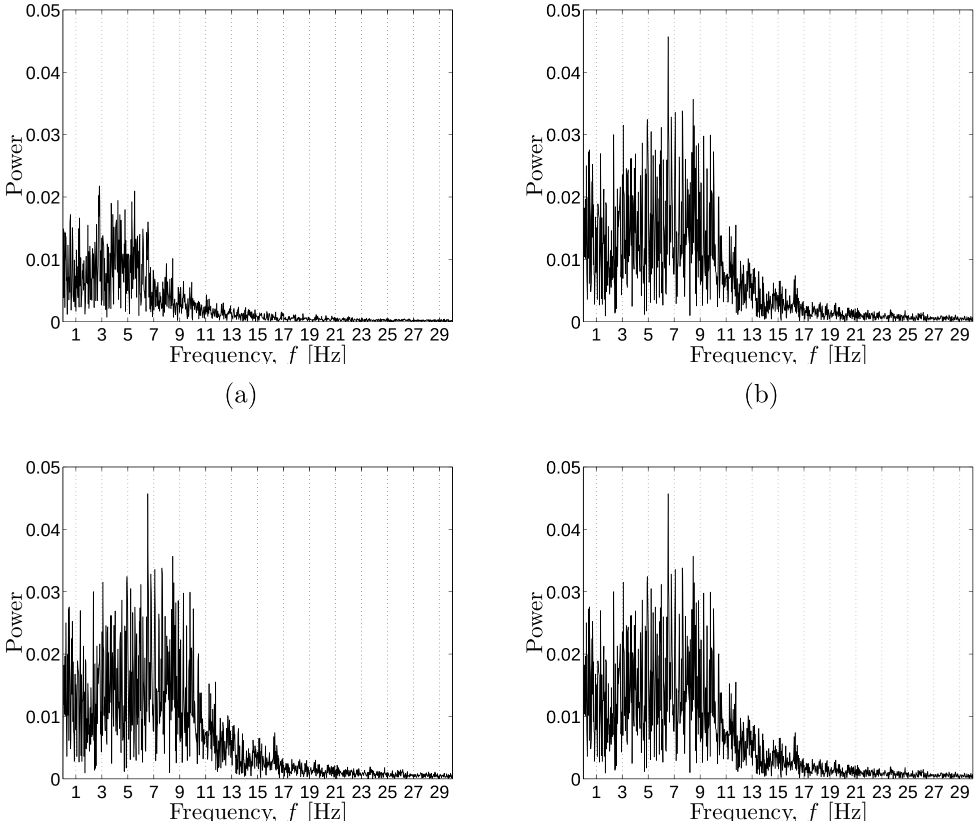

(a) (b)

(c) (d)

Figure 3.5: Power spectra of the pressure data obtained at $\frac{L}{D} = 2.75$, $Re = 55,000$ without center body, no actuation for the pressure sensor (a) 1, (b) 2, (c) 3 and (d) 4.

Figure 3.5 is an example of power spectra of all pressure signals before firing the injectors. Figure 3.5 has a chamber length of $\frac{L}{D} = 2.75$ (as shown in Figure 2.6), a main jet Reynolds number of $Re = 55,000$ based on the nozzle inlet diameter (d) and the four pressure sensors are located as described in Chapter 2.

The results are not promising since there is no dominant peak in the frequency domain. The continuous spectra signature over a limited range of frequencies can be an indicator of chaotic nature of the flow as shown in Figure 3.5) [42]. Nevertheless, there is a hope to observe different behavior when turning to the actuated flow, since the actuation may affect the spectra of the pressure signal as shown in Figure 3.6.

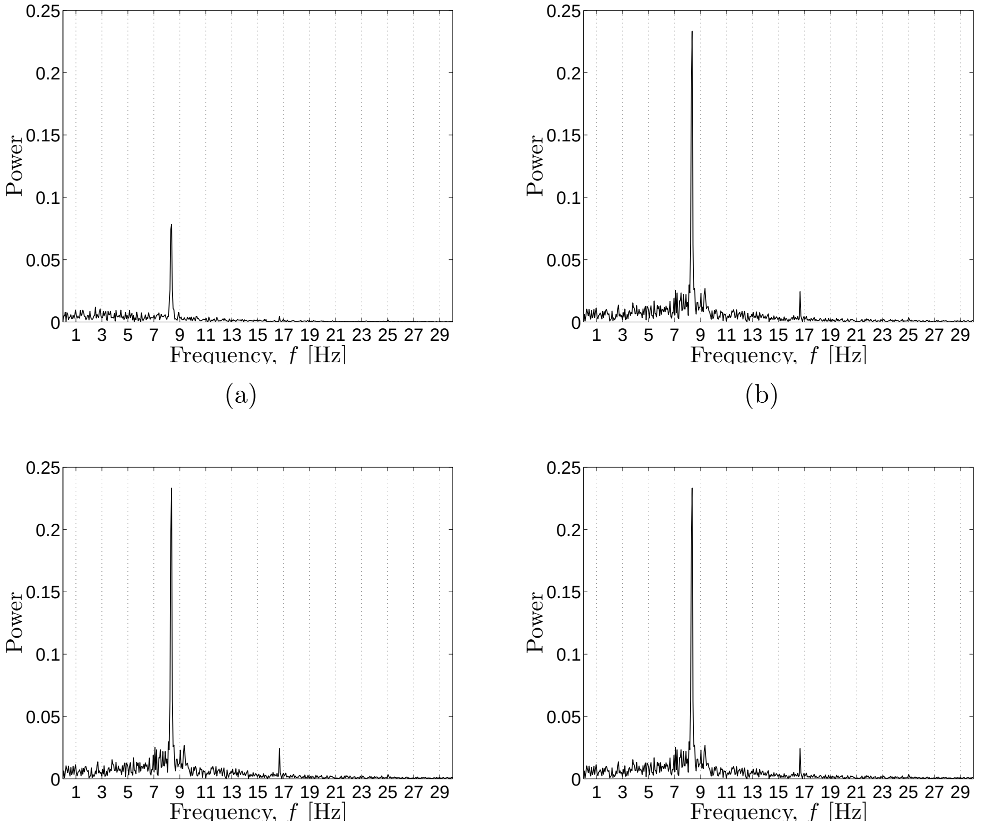

(a) (b)

(c) (d)

Figure 3.6: Power spectra of the pressure data obtained at $\frac{L}{D} = 2.75$, $Re = 55,000$ without center body during CCW actuation with $f = 8$ Hz for the pressure sensor (a) 1, (b) 2, (c) 3 and (d) 4; (in this case, the actuation can change the precession direction).

Figure 3.6 shows the spectra of the pressure signals for the same flow conditions as Figure 3.5 except now the actuation is turned on with $f = 8$ Hz. The flow rate through each micro-jet is described in Chapter 2 and shown in Figure 2.13. The actuation excites an inherent frequency of 8 Hz in the system which is reflected in its spectra shown in Figure 3.6. Changing the actuation frequency to $f = 3$ Hz for the same flow condition results in the pressure power spectra in Figure 3.7 which does not exhibit a distinct peak. Despite the actuation, this flow exhibits chaotic behavior.

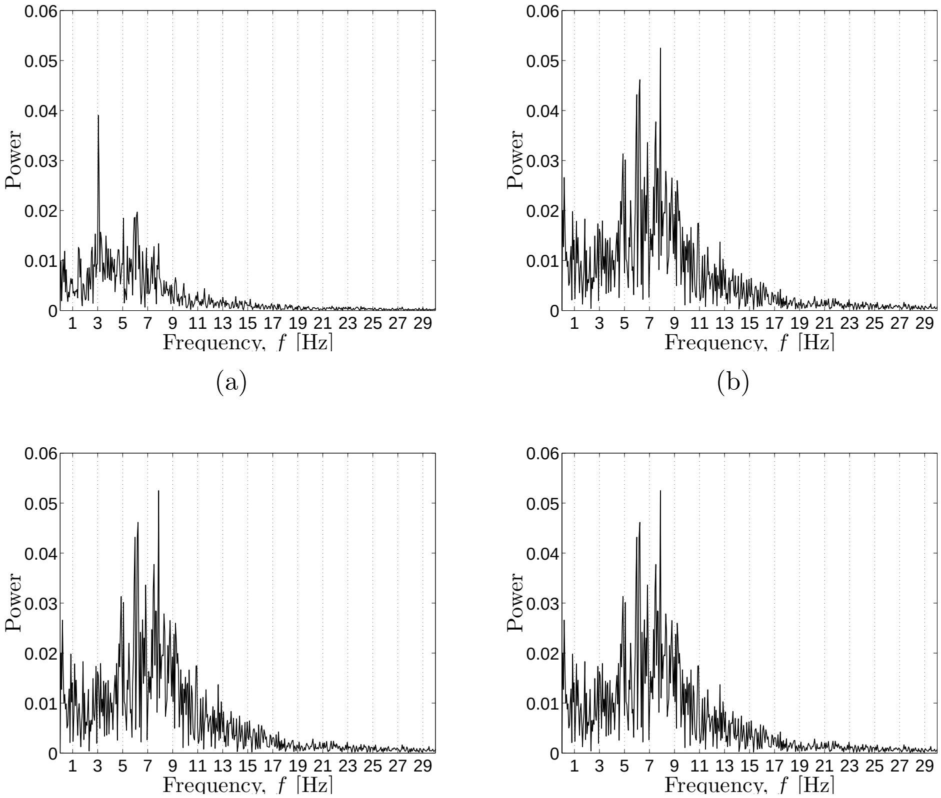

(a) (b)

(c) (d)

Figure 3.7: Power spectra of the pressure data obtained at $\frac{L}{D} = 2.75$, $Re = 55,000$ without center body during CCW actuation with $f = 3$ Hz for the pressure sensor (a) 1, (b) 2, (c) 3 and (d) 4; (in this case, the actuation can change the precession direction).

In the next sections, a method will be introduced to find the precession direction. Using this method, it is found that only if the actuation succeeds in forcing the flow to follow the actuation direction, then a single spike appears in power spectra (Figure 3.6). Otherwise the flow still behaves in a chaotic fashion with the resulting full spectra shown in Figure 3.7.

Efforts to find a measure using FFT methods (spectrogram) to investigate actuation effectiveness are confounded by noise and the non-periodic (chaotic) pressure signals. Since the standard FFT is a common method, it is worth trying initially, but the complexity of the precessing jet flow has made it essential to look at other more successful methods in the subsequent sections.

3.3 Cross correlation

As the precessing jet rotates, each pressure sensor sees the high velocity region of the jet after Δt_i from passing the previous sensor. The delay between the signals of two successive sensors can be calculated using cross correlation. Summing them all up, the frequency of precession can be found as:

$$f_p = \frac{1}{\sum_{i=1}^{4} \Delta t_i} \tag{3.3}$$

As shown in Figure 3.8, cross correlation is calculated for four pressure signals within a specific window size. For example, Figure 3.8 shows four dynamic pressure signals within three windows which are used for cross correlation.

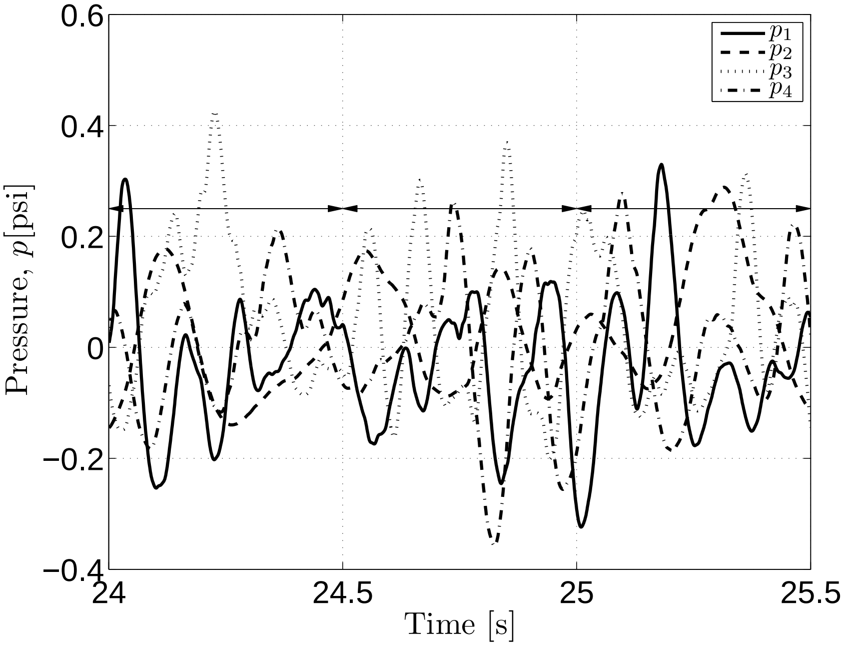

Figure 3.8: An example of pressure data used for cross correlation at $\frac{L}{D} = 2.5$, $Re = 47,000$ and no actuation and without center body.

The cross correlation can also be used to determine the direction of precession. Correlation of (p_1, p_2) is positive if p_1 advances with respect to p_2, otherwise it is negative. Since the sensor number increases in CW direction, obtaining negative value means that p_1 advances p_2, so precession is in CW direction. Figure 3.8 shows a section of the four pressure signals for 1.5 s. The corresponding cross correlation plot is given in Figure 3.9. The lag of maximum peaks of all four cross correlations of adjacent pressure signals are negative in Figure 3.9 indicating a CW direction of precession during this 1.5 s window resulting in f_p = 3.8 Hz CW. Both the frequency and direction of precession vary with time for this flow condition; so cross correlation window size (time interval) strongly influences the results.

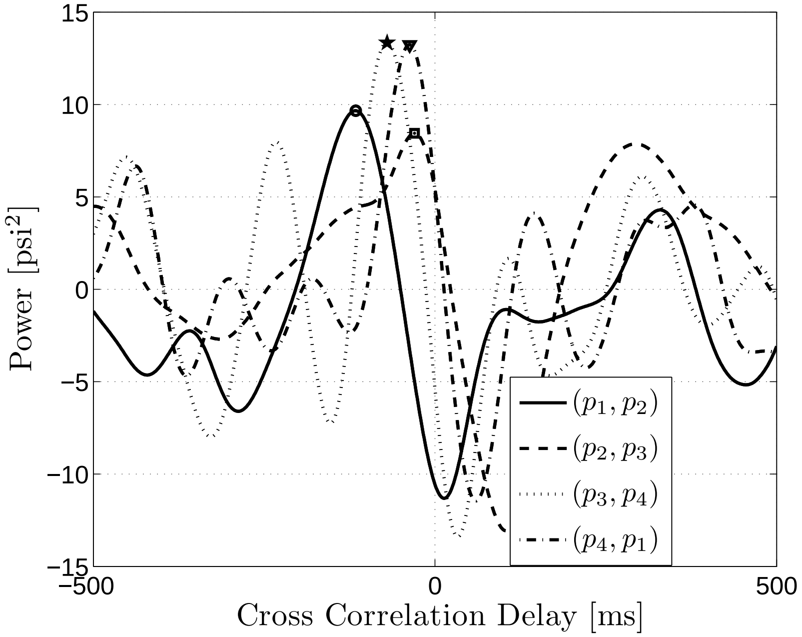

Figure 3.9: Cross correlation of the example pressure signals (Figuere 3.8) with the corresponding peak locations ($\frac{L}{D}$ = 2.5, Re = 47,000 and no actuation and without center body).

The precession frequency (f_p) obtained by cross correlation within different window sizes for this flow condition is given in Figure 3.10. The pump, micro-jet actuation and pressure measurement schedule is as in Figure 3.1. The cross correlation window is selected at an interval when the actuation (with a frequency of 5 Hz in CCW) is activated (at t=40 s). For the small window sizes (e.g. 0.2 s), the fluctuations of the precession frequency are large which makes it difficult to interpret. However, for large cross correlation window sizes, e.g. 5 s, the precession frequency is much smoother than with short intervals. After actuation (starting at t = 40 s), the window size of 5 s correctly determines f_p = 5 Hz with positive sign which is the indicator of CCW direction. Since the entire actuation time is 20 s (from t = 40 s to t = 60 s), the precessing frequency is extracted from four cross correlation window (when the window size is 5 s). A more detailed discussion about the cross correlation method can be found in Appendix D.

To use the cross correlation method to analyze a precessing jet, it is needed to find an appropriate window size for each signal. While large window sizes decrease the temporal resolution of the results, small windows can not capture the precession distinctly. This behavior is also attributed to the quasi-flapping motion of the precessing jet in which the jet passes (jumps) over a pressure probe without being captured with the corresponding pressure sensor. The window size selection problem along with difficulties in peak selection discussed in Appendix D cause the cross correlation method to fail to monitor the precession phenomenon. The next section introduces another method to process the pressure data using a phase plane representation.

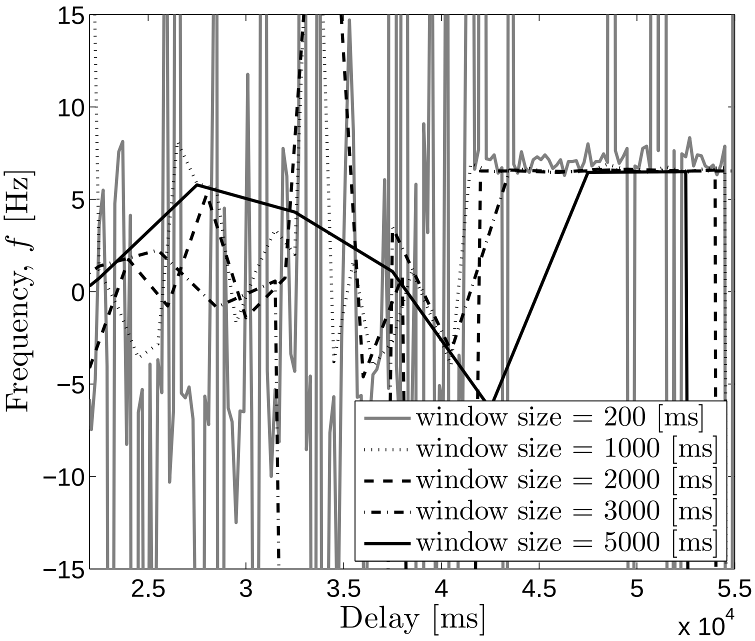

Figure 3.10: The sensitivity of the cross correlation results to the selected window size.

3.4 Phase plane method

Another approach to characterize the motion of a precessing jet is to determine the location of the high velocity region of the jet at the chamber exit. Being able to determine the relative location of the jet high velocity region using four pressure probes at the chamber exit would allow real-time monitoring of the precessing jet. To do this, a phase plane at the chamber exit is constructed by mapping the pressure data in a plane made up of a y axis, the difference between first and third sensors ($y = p_1 - p_3$) versus a x axis, the difference between second and fourth sensors ($x = p_2 - p_4$), as shown in Figure 3.11.

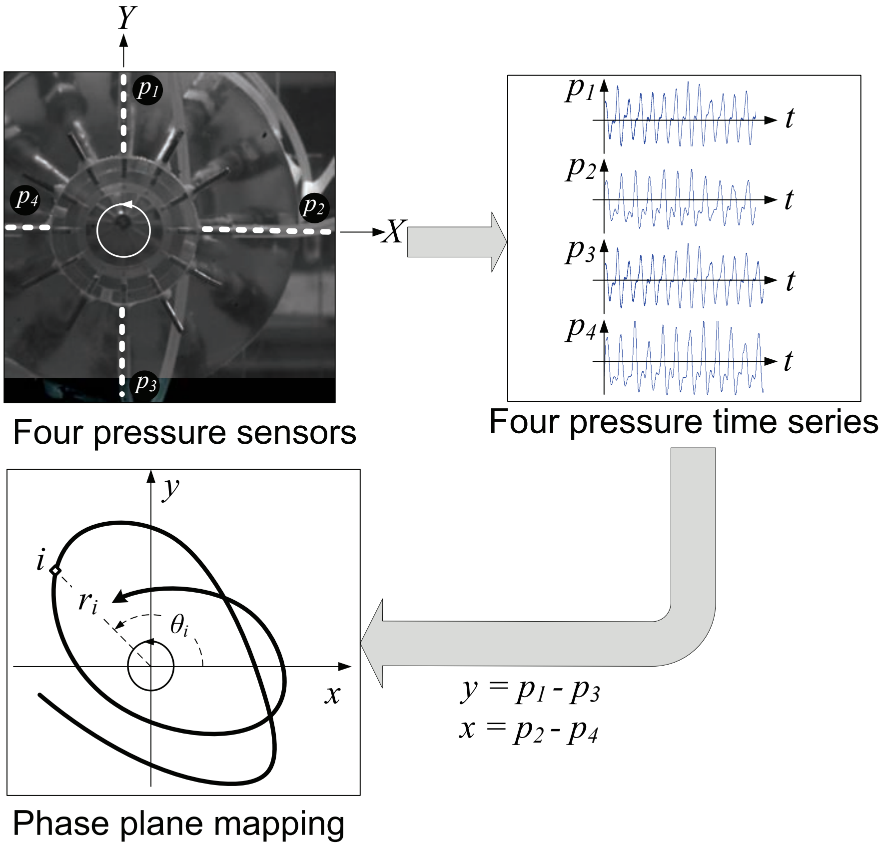

Figure 3.11: Location of four pressure probes on the periphery of the chamber without center body and the schematic phase plane representation of the relative location of jet high velocity region with respect to the probe locations over time; the direction of the curve at the phase plane mapping box shows time marching direction.

A description of chaotic motion in confined jet flows is given in [43]. Also the concept of *limit cycle* is used to study the transient nature of the precessing jet by plotting in-plane velocity components in a Cartesian coordinate [19].

The current research benefits from another similar tool developed based on pressure data. A more detailed study on chaotic behavior of excited axisymmetric jet which led to a phase diagram depicting flow states with respect to actuation can be found in [44] and [45].

The length of the curve in phase plane increases with time and a comparison with the top photograph in Figure 3.11 confirms that this mapping maintains the same (CW/CCW) rotation defined earlier. The radius of this curve can be interpreted as the radial distance of the jet high velocity region from the chamber axis. It is assumed that this trajectory mimics the trajectory of the high velocity region of the precessing jet at the chamber exit. This assumption is investigated in Chapter 4 using S-PIV at the chamber exit.

An example data set analyzed in this manner is shown in Figure 3.12(a) which represents the phase plane data for a test condition without center body and before actuation. Adding a center body (Figure 3.12(b)) increases the dynamic pressure observed by the probes and more importantly, the jet spins in a more stable fashion around the chamber axis. Figure 3.12(c) and Figure 3.12(d) show the effect of CCW actuation (f=6 Hz) for the chamber without and with center body, respectively. The stabilizing effect of this actuation and the center body is revealed by this phase plane representation of the precessing jet. The phase plane representation of all data sets (1400) can be found in Appendix E.1.

In order to find the direction of precession over time, two different methods were initially examined. Two displacement vectors of three successive points ($\overrightarrow{D}_i$ and $\overrightarrow{D}_{i+1}$) in the phase plane are defined in Figure 3.13. In the first method, the cross product of these two vectors are calculated:

$$
\begin{aligned}
\overrightarrow{D}_i \times \overrightarrow{D}_{i+1} &= \begin{vmatrix} \overrightarrow{i} & \overrightarrow{j} & \overrightarrow{k} \\ x_i - x_{i-1} & y_i - y_{i-1} & 0 \\ x_{i+1} - xi & y_{i+1} - yi & 0 \end{vmatrix} \\
&= \underbrace{\left[(x_i - x_{i-1})(y_{i+1} - y_i) - (y_i - y_{i-1})(x_{i+1} - x_i)\right]}_{R_i} \overrightarrow{k}
\end{aligned}
\tag{3.4}
$$

Looking at the flow from the jet downstream view (along the Z axis), the sign of this cross product is the direction of precession with a positive value representing CCW direction and a negative value is CW direction. This method can fail to correctly calculate the precession direction if the curvature of the phase plane curve changes frequently despite a constant precessing direction. For instance, as shown in Figure 3.14, the direction of precession is always CCW, but the first method result shows that its direction varies frequently due to change in curvature.

In the second method, the integration of phase plane curve is calculated

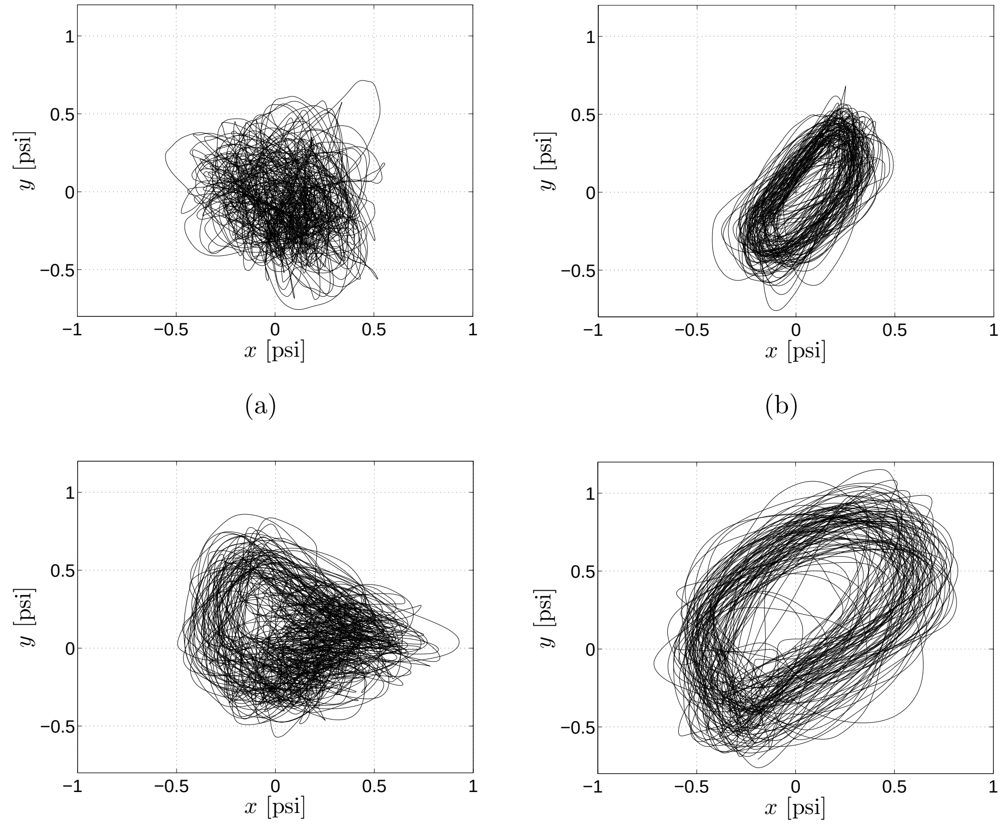

(a) (b)

(c) (d)

Figure 3.12: Phase plane data obtained at $\frac{L}{D} = 2.5$, $Re = 47,000$ and CCW actuation of $f = 6$ Hz without center body (a) no actuation (b) actuation, with center body (c) no actuation (d) actuation. The effect of passive control, i.e. adding the center body (left to right); the effect of active control, i.e. turning on the CCW actuation (up to down).

for each time step (see Figure 3.13):

$$\Delta s_i = \frac{1}{2}[(x_{i+1} - xi)(y_i + y_{i+1})] \tag{3.5}$$

then the integration of this curve from initial time is calculated:

$$S(t_n) = \sum_{i=0}^{n} \Delta s_i \tag{3.6}$$

Looking at Figure 3.15, the positive and negative slopes of S correspond to CW and CCW precession, respectively. This method is used in this study to investigate the direction of precession over time.

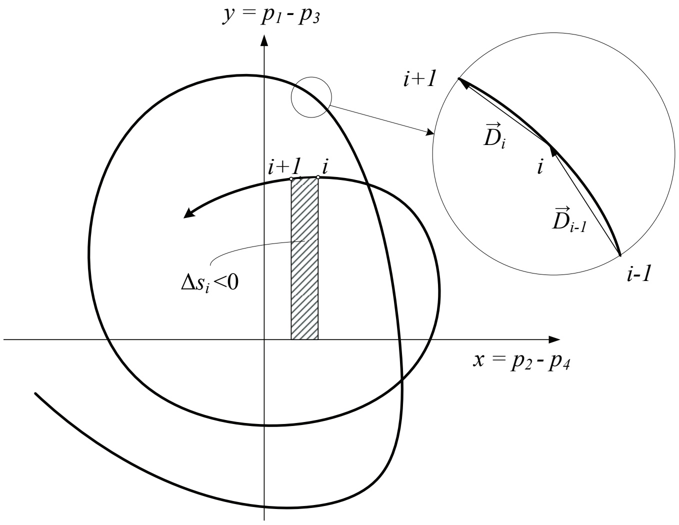

Figure 3.13: Integration and cross-product methods to calculate the direction of precession based on phase plane mapping.

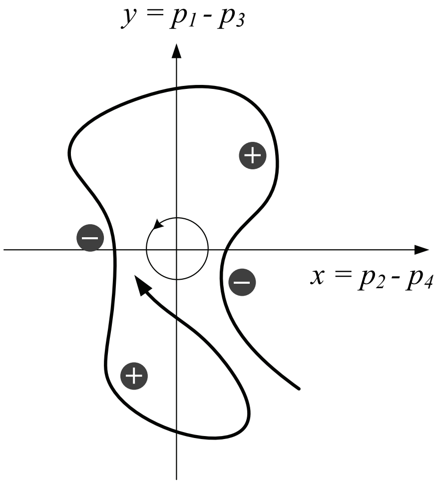

Figure 3.14: CCW precession with positive and negative curvatures. The negative curvatures cause Equation 3.4 to fail to calculate the precession direction.

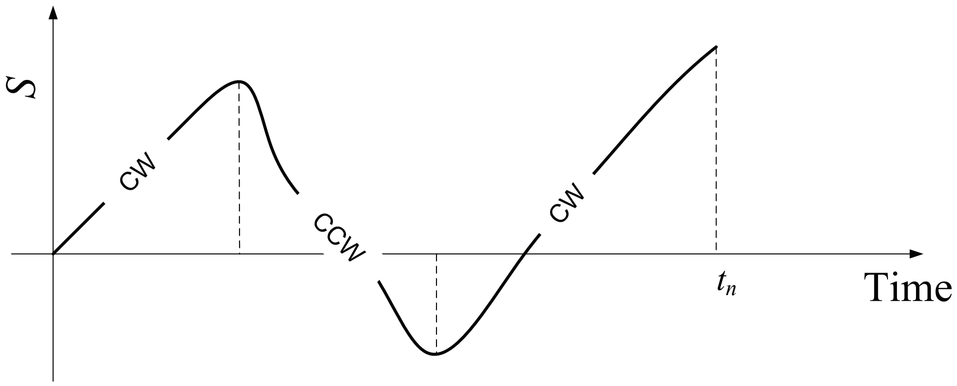

Figure 3.15: Schematic representation of S value versus time; the slope of S indicates the direction of the precession such that the positive and negative S values show CW and CCW precession, respectively.

3.5 Phase plane direction analysis

This section describes several experiments conducted to understand the behavior of processing jet under control. The test procedure for the first experiment is given in Figure 3.16. The direction analysis, using Equations 3.5 and 3.6, of this experiment for several Reynolds numbers are shown in Figure 3.17. Increasing Reynolds number increases the dynamic pressure and thus the pressure difference for a precessing jet. This, in turn, causes a larger x and y values in the phase plane and so Δs_i in Equation 3.5 is larger, resulting in a larger slope in Equation 3.6. More importantly, Figure 3.17 indicates that the jet precession in this setup has a preferred direction before actuation (first 40 s) which is CW (the flow is actuated CCW direction by the prior knowledge of this preferred CW direction). At t = 40 s, the CCW actuation is activated and the direction of precession switches to CCW in low Re. However, at high Reynolds numbers, precession resists switching directions ($Re \geq 55,000$), and at $Re = 62,000$, the actuation cannot affect the precession direction.

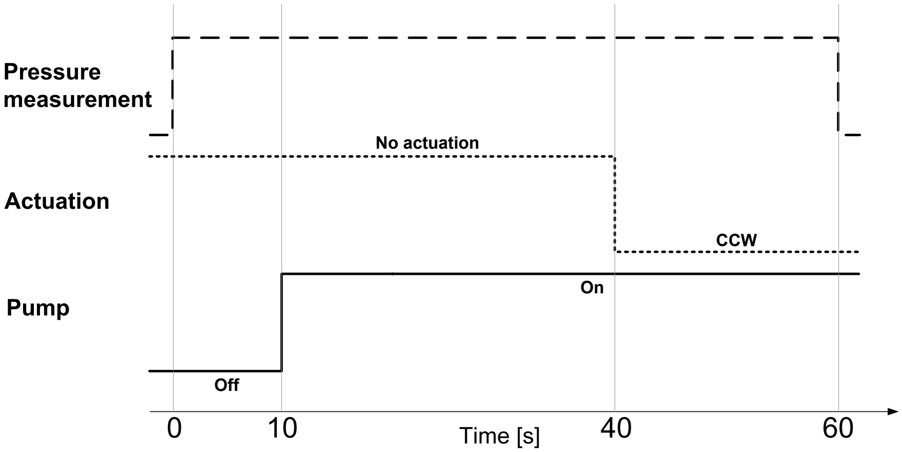

Figure 3.16: Timeline for pump, pressure measurement and actuation operations.

By increasing Reynolds number, the actuation is unable to affect the precession direction, in particular, reversing the preferred direction. This gives rise to two questions. *Can the preferred direction of precession be reversed?* and *If the direction can be reversed, is the response of the actuated jet similar to the original jet?*

To answer these questions, an experiment is designed to initially disturb the flow in the reverse of the preferred direction before running the flow as shown in Figure 3.18. Here, the micro-jet actuation is turned on 10 s before running the pump. The results are shown in Figure 3.19 (scenario-b) and show that the initial CCW actuation (beginning at 10 s, i.e. 10 s before the main jet is turned

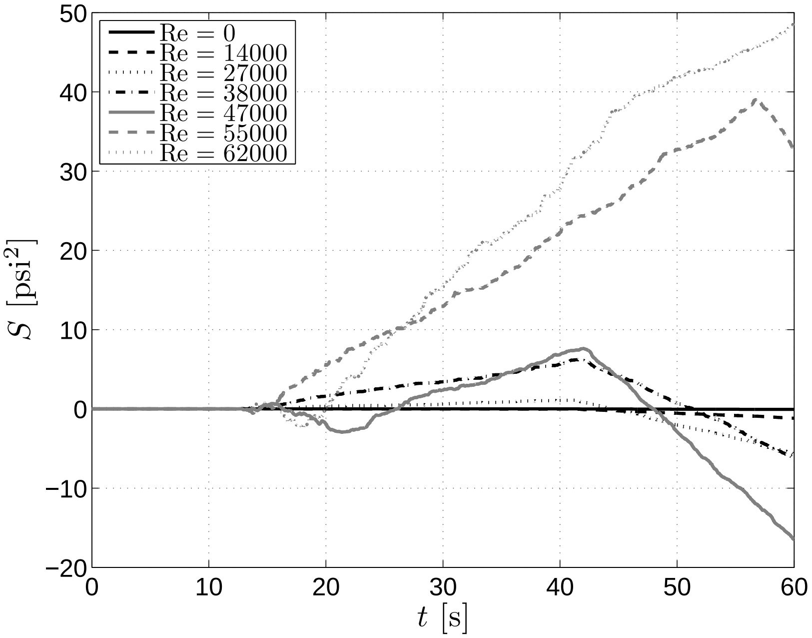

Figure 3.17: Direction analysis for the CCW actuation of the flow with the chamber length $(\frac{L}{D})$ of 2.5 at $f = 6Hz$; CW is the preferred direction of precession; also it shows the effect of Reynolds number on actuation effectiveness, i.e. the ability to change the precession direction.

on) leads to CCW precession. If the same actuation is applied once the main jet is on, it does not affect the precession direction (Figure 3.19 (scenario-a)). However, actuation by scenario-b (Figure 3.19) in the preferred CW direction at 35 s does cause this flow to switch to CW direction. Consequently, for this case, the behavior of precessing jet strongly depends on its initial states.

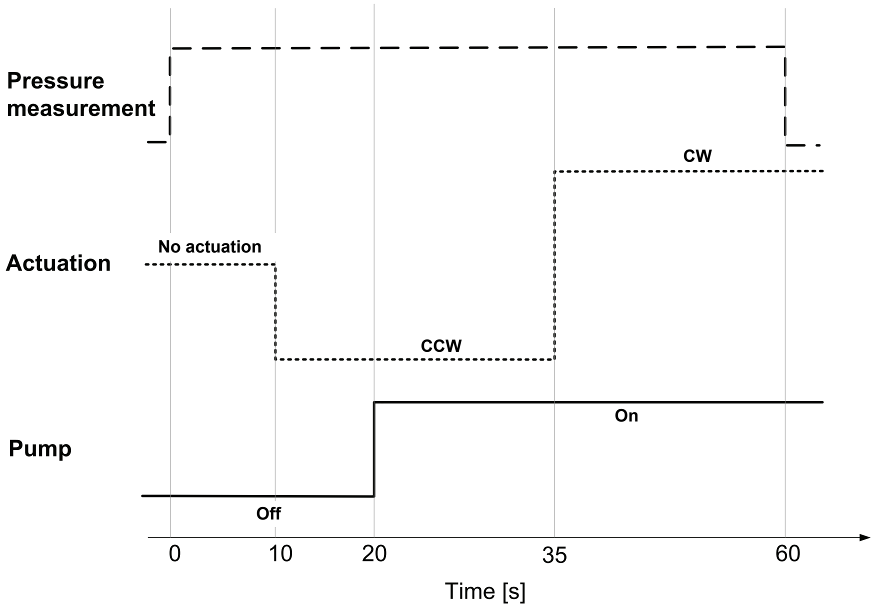

Figure 3.18: Timeline for pump, pressure measurement and actuation operations to study the effect of initial actuation; the flow is actuated initially with CCW before running the pump and after 20 s the actuation is switched to CW direction.

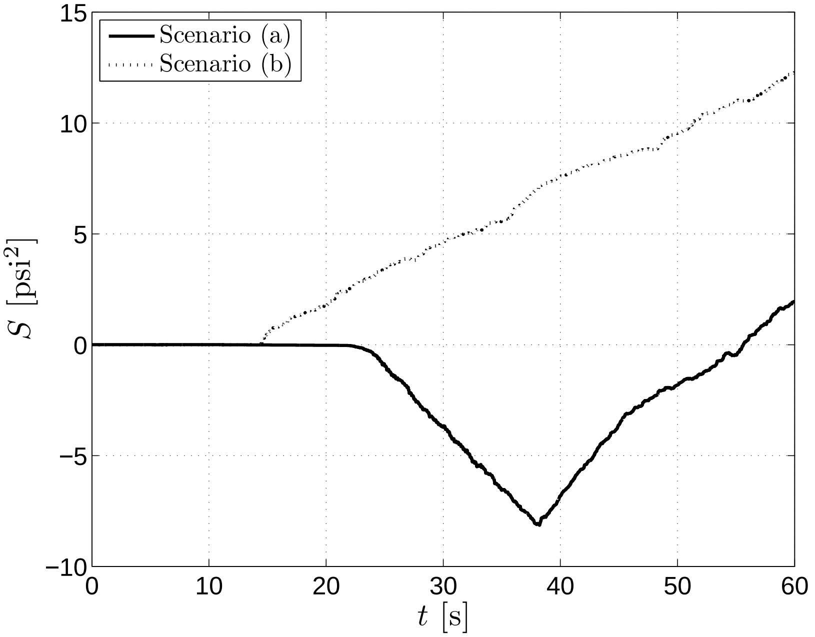

Figure 3.19: Direction analysis for the actuation of the flow with the chamber length ($\frac{L}{D} = 2.5$), $Re = 62,000$ at the frequency ($f = 5$ Hz); the effect of initial disturbance on the ability of actuation to change the preferred direction of the precession. Scenario (a): Figure 3.16, Scenario (b): Figure 3.18.

The ability to control precession at a Reynolds number range where control is marginal is investigated by frequently switching the actuation direction. Figure 3.20 shows the actuation pattern designed for this purpose. The result in Figure 3.21 shows that the precession can be controlled for $Re = 47,000$ regardless of the precession history (for the given test conditions). By increasing Reynolds number, the ability to manipulate the flow decreases such that at $Re = 55,000$, the flow does not follow the actuation.

To show the difficulty in controlling precession direction at $Re = 62,000$ (highest Reynolds number), 35 tests are conducted for a longer time interval with the actuation shown in Figure 3.22. The results for the 35 cases are shown in Figure 3.23. The switching time (if there is one) of direction does not seem to have an obvious correlation with the location of the jet at the start of the actuation.

The first and easiest measure to assess the effectiveness of actuation is to see whether the precession follows the actuation direction or not. However, this method does not offer any quantitative measure to compare different flow and actuation conditions. Nevertheless, this information can be used to get an idea about the behavior of the flow under control. The direction analysis of all data sets collected in this research is documented in Appendix E.2.

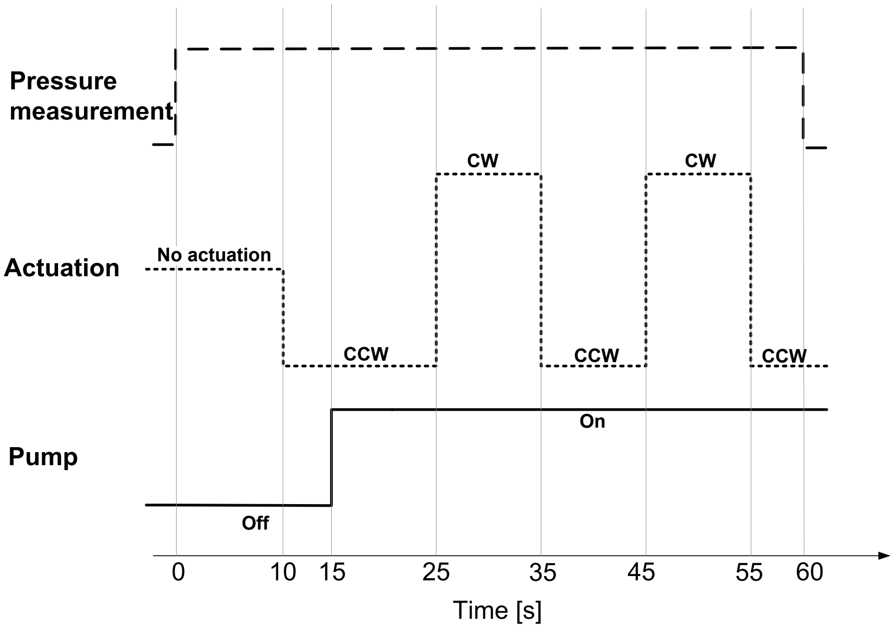

Figure 3.20: Pump, pressure measurement and actuation operations versus time used to study the effectiveness of active control in the actuation with frequent direction switching with the result in Figure 3.21.

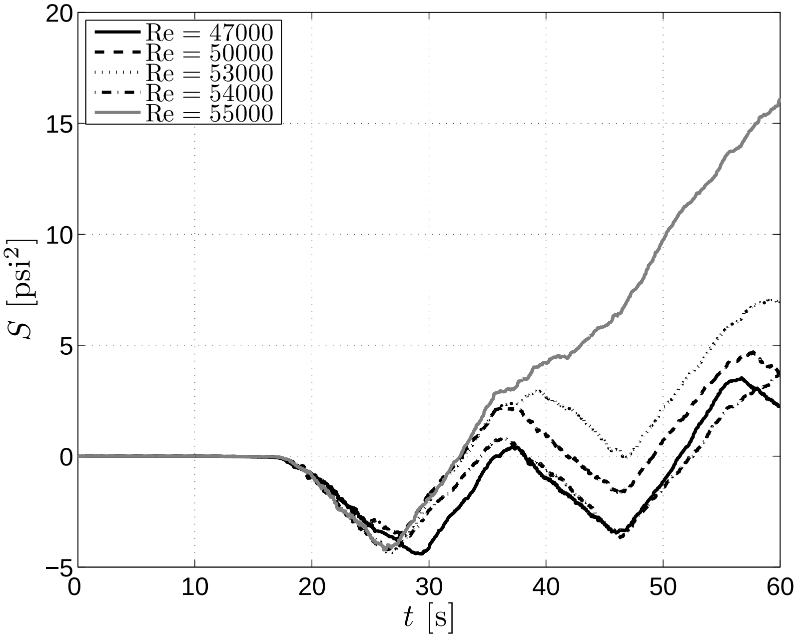

Figure 3.21: Direction analysis for the actuation of the flow with the chamber length ratio ($\frac{L}{D}$ = 2.5) at the frequency (f = 5 Hz); the influence of Reynolds number on the control of the precession direction by the actuation with frequent direction switching.

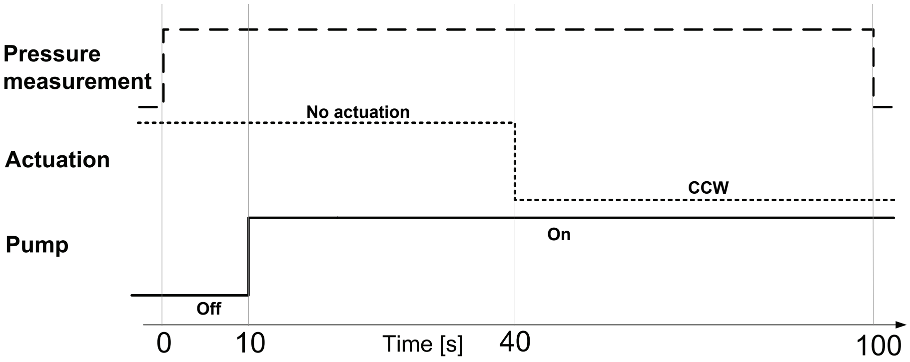

Figure 3.22: Timeline for pump, pressure measurement and actuation operations, the actuation time is 1 min.

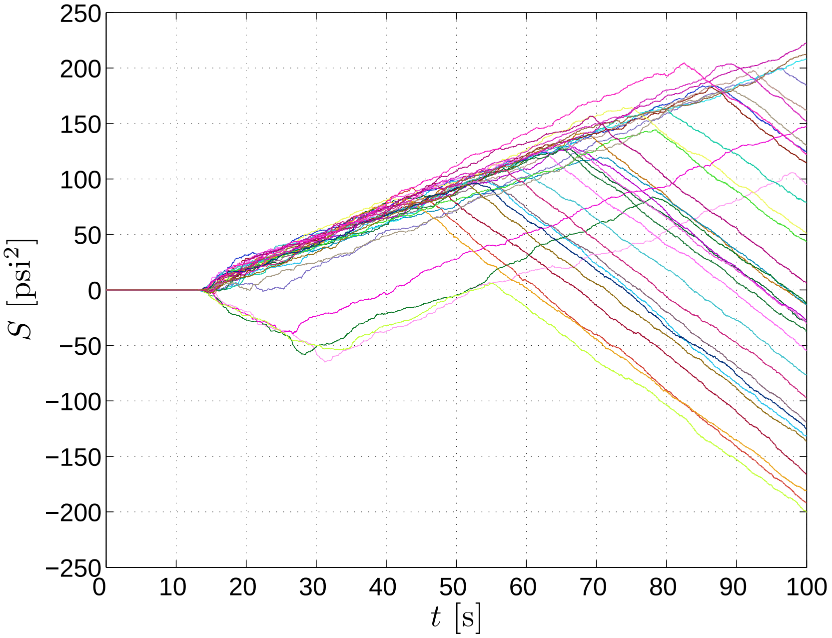

Figure 3.23: Direction analysis for the actuation of the flow with the chamber length ratio ($\frac{L}{D} = 2.5$), $Re = 62,000$ at the frequency ($f = 5$ Hz); CCW actuation of the flow for 34 times to study the precession direction switching time. Negative slope corresponds to CCW rotation and this flow is actuated using CCW actuation; therefore, it is expected to see all curves get negative slope after 40 s; however, as shown in the figure, the switching to CCW occurs quite arbitrarily.

3.6 Phase plane radius analysis

The radius (r) and phase angle (θ) in the $x = p_2 - p_4$, $y = p_1 - y_3$ phase plane are defined in Figure 3.11. As discussed in Chapter 1, axial and precessing modes are the two dominant modes reported for this flow. In axial mode, all the pressure probes measure almost the same pressure, so the radius of phase plane remains near zero. For a precessing flow, the value of r increases. The value of r, since it is an indicator of dynamic pressure, increases with Reynolds number. It is expected to observe a decrease in r as the chamber length increases, analogous to the pressure drop in a pipe flow. The phase plane data for the center body (top row in Figure 3.24) and without the center body (bottom row in Figure 3.24) as a function of five chamber lengths $2 \le \frac{L}{D} \le 3.5$ is plotted in Figure 3.24. For both the center body and without the center body cases, r does decrease as $\frac{L}{D}$ increases (with one exception for $\frac{L}{D} = 2$ with center body). To see these effects over the entire range of test points, a measure of the average value $\bar{r}$ is calculated for all Reynolds numbers and chamber length ratios ($\frac{L}{D}$):

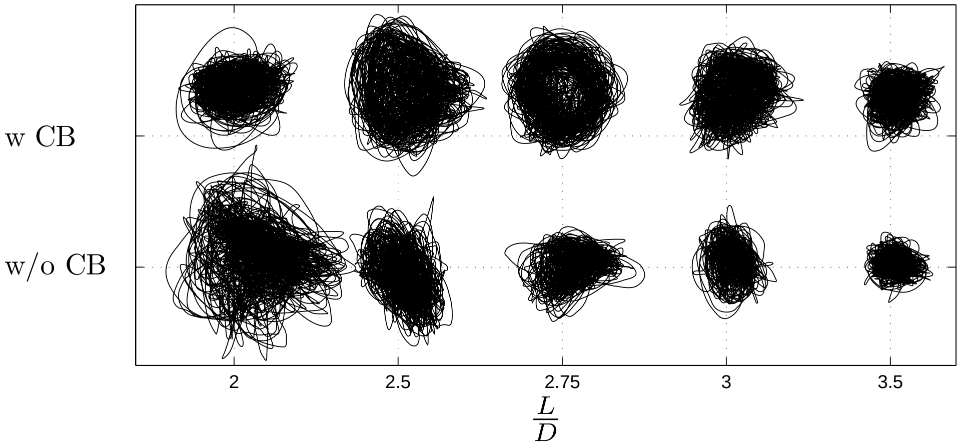

Figure 3.24: The influence of chamber length on the phase plane representation for the chamber at Re=62,000 and no forcing micro-jet. Top row with center body. Bottom row without center.

$$\bar{r} = \frac{1}{n}\sum_{i=0}^{n} r_i \tag{3.7}$$

First, focusing on the precessing jet without actuation, at each Reynolds number and $\frac{L}{D}$ value, an average of 20 test points is calculated. To see the phase plane behavior and to remove the dynamic pressure effect on $\bar{r}$ value due to Reynolds number, $\bar{r}$ is normalized by the dynamic pressure corresponding to the inlet velocity of the main jet at the nozzle inlet. R_n is defined as:

$$R_n = \frac{\bar{r}}{\frac{1}{2}\rho U_i^2} \tag{3.8}$$

R_n values as a function of chamber length for six Reynolds numbers and with and without center body are plotted in Figure 3.25. As expected, without the center body, all curves are grouped together and R_n decreases as $\frac{L}{D}$ increases. With the center body, the different Reynolds number lines are not as closely grouped. For $\frac{L}{D} = 2$, R_n is smaller than for $\frac{L}{D} = 2.5$ and here it is speculated that this might be due to a strong axial mode cavity oscillation at $\frac{L}{D} = 2$.

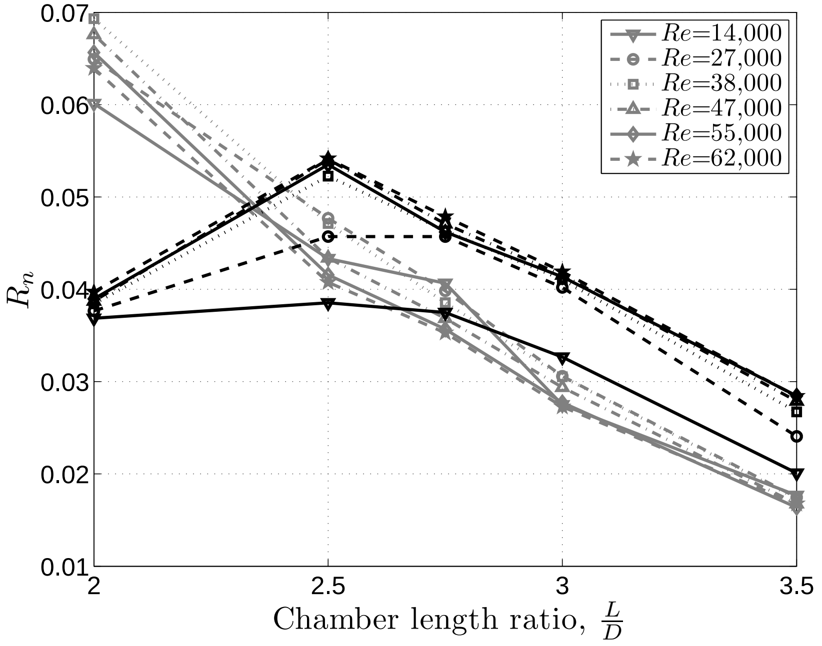

Figure 3.25: The influence of chamber length on the dynamic pressure normalized value.(gray: without center body, black: with center body).

To investigate the effect of the center body on r value compared to without the center body, the difference between R_n without and with center body ($R_{n,\text{CB}}$) are compared using $\tilde{R}$:

$$\tilde{R} = \frac{R_{n,\text{CB}} - R_n}{R_n} \tag{3.9}$$

This comparison is shown in Figure 3.26, plotting the influence of chamber length and Reynolds number versus $\tilde{R}$. The relative effectiveness of the center body generally increases for all chamber lengths and Reynolds numbers.

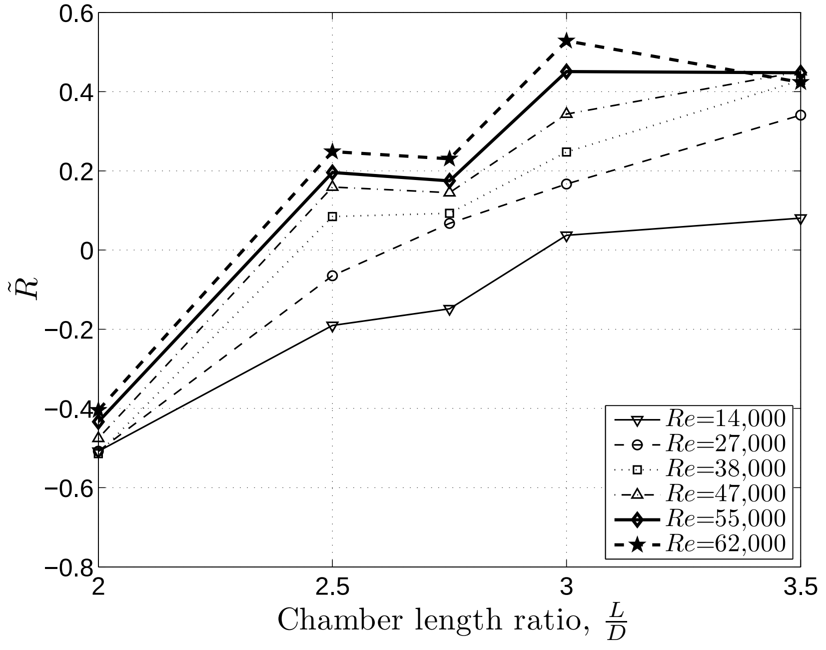

Figure 3.26: The influence of chamber length on relative increase of mean value of phase plane radius by adding a center body (passive control).

3.7 Phase plane phase analysis

The ultimate objective of the pressure data analysis is to determine a measure to evaluate the actuation effectiveness on the precession phenomenon. This measure should be able not only to evaluate the actuation effectiveness at each test point, but also to compare the actuation effectiveness over the entire range of test points. Different parameters are examined ranging from the maximum peak of FFT spectra to R_n for this purpose. More complicated ideas are left for further studies (particulary chaos parameters such as Lyapunov exponent and correlation dimension [44]). More chaotic tools to study this flow can be found in [42]. In this section, a measure is introduced and a phase diagram is developed based on it.

During the experiments, the command signal of the injector 1 is collected. It is used as a trigger for the pressure data providing data which is synchronous with the actuation pattern. A sample of the injector 1 signal along with the voltages of the pressure sensors are shown in Figure 3.27. The triggered data, at the start of injector 1 command is denoted by ”•” in Figure 3.27 and is stored separately. A typical data set has between 20 to 200 trigger points for the actuation frequency f = 1 Hz to f = 10 Hz, respectively. These triggered data points are then displayed on a phase plane in Figure 3.28 for two different

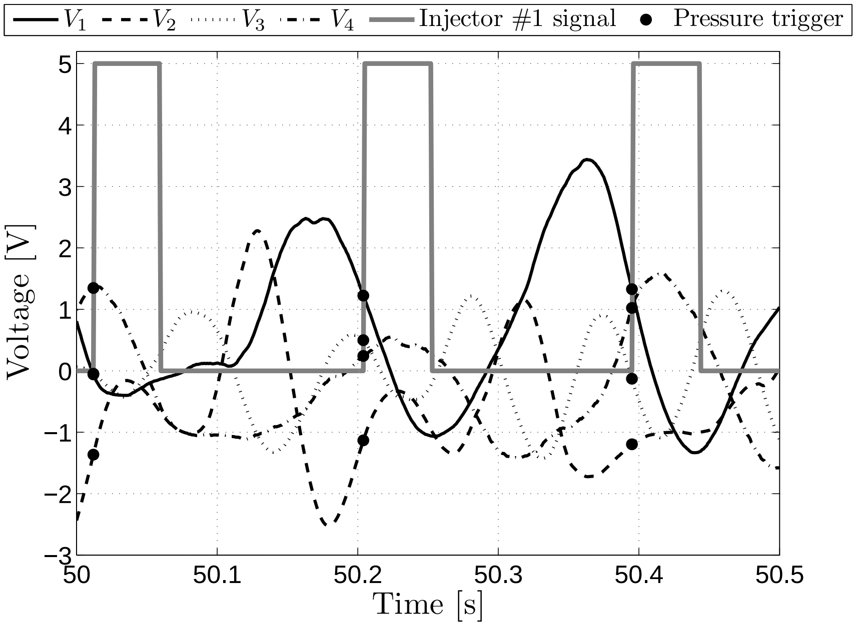

Figure 3.27: A sample of the voltage signal along with the signal of injector # 1; the injector signal is used to sample the corresponding pressure data.

test points. High actuation effectiveness where the flow follows the actuation faithfully is shown in Figure 3.28(a). A test point where the actuation is unable to manipulate the precessing jet properly is shown in Figure 3.28(b).

To quantify these observations, the standard deviation of the phase angle (θ_{STD}) of these points from their centroid is selected (shown in Figure 3.28 by ⧫) and this gives a measure of scattering of these points in azimuthal direction. This value is calculated for all test points and is given in $Re - f$ plane for all chamber lengths from Figures 3.29 to 3.33. The results of chamber without center body are given at the top and with center body at the bottom while right and left plots are actuated in CW and CCW direction, respectively. The colorbar is θ_{STD} and darker values indicate that θ_{STD} increases. Therefore, bright regions represent where the actuation stabilizes the flow precession.

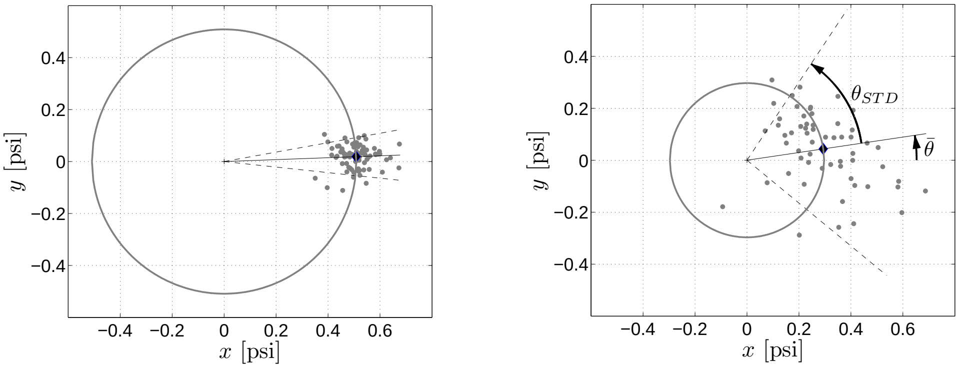

(a) (b)

Figure 3.28: The phase plane representation of the triggered pressure data and the standard deviation of their phase with respect to their centroid point (shown in figures by ⧫) at $\frac{L}{D}$=2, without center body, CW actuation for (a)Re=27,000, f=4 Hz and (b)Re=38,000, f=3 Hz.

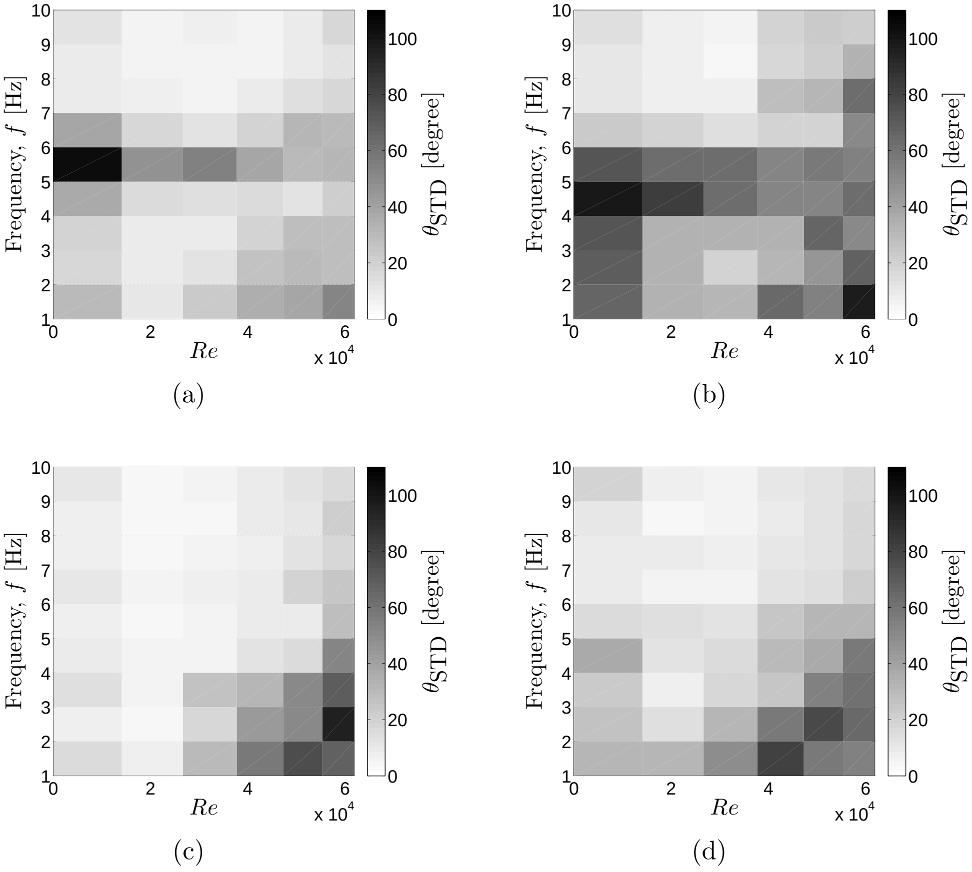

(a) (b)

(c) (d)

Figure 3.29: The influence of frequency and Reynolds number on STD of phase of the triggered pressure data at the chamber length $\frac{L}{D}$=2. Without center body, (a) CW, (b) CCW actuation. With center body, (c) CW and (d) CCW actuation.

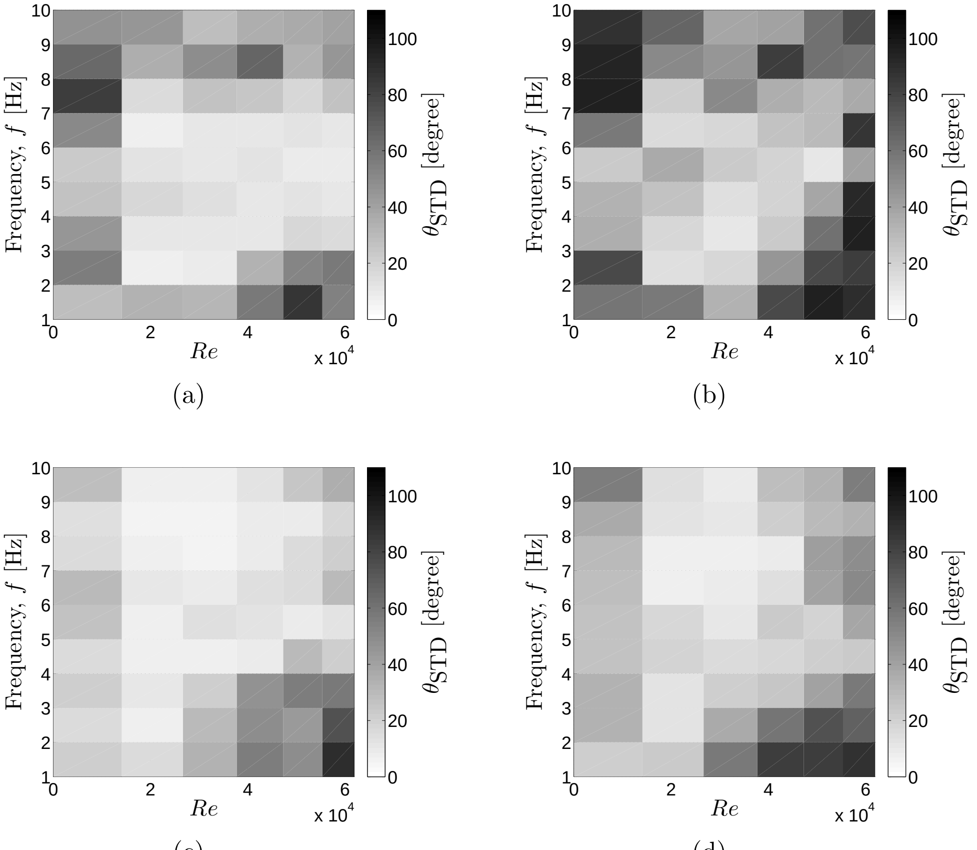

(a)

(b)

(c)

(d)

Figure 3.30: The influence of frequency and Reynolds number on STD of phase of the triggered pressure data at the chamber length ratio $\frac{L}{D}$=2.5. Without center body, (a) CW, (b) CCW actuation. With center body, (c) CW and (d) CCW actuation.

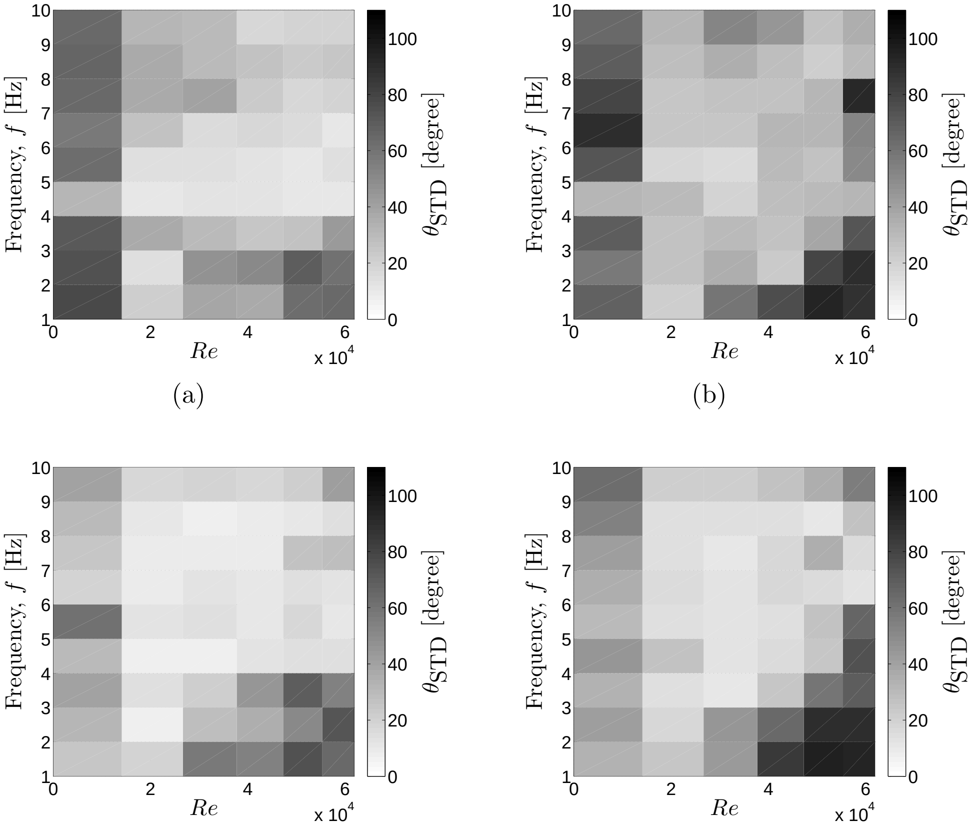

(a)

(b)

(c)

(d)

Figure 3.31: The influence of frequency and Reynolds number on STD of phase of the triggered pressure data at the chamber length ratio $\frac{L}{D}$=2.75. Without center body, (a) CW, (b) CCW actuation. With center body, (c) CW and (d) CCW actuation.

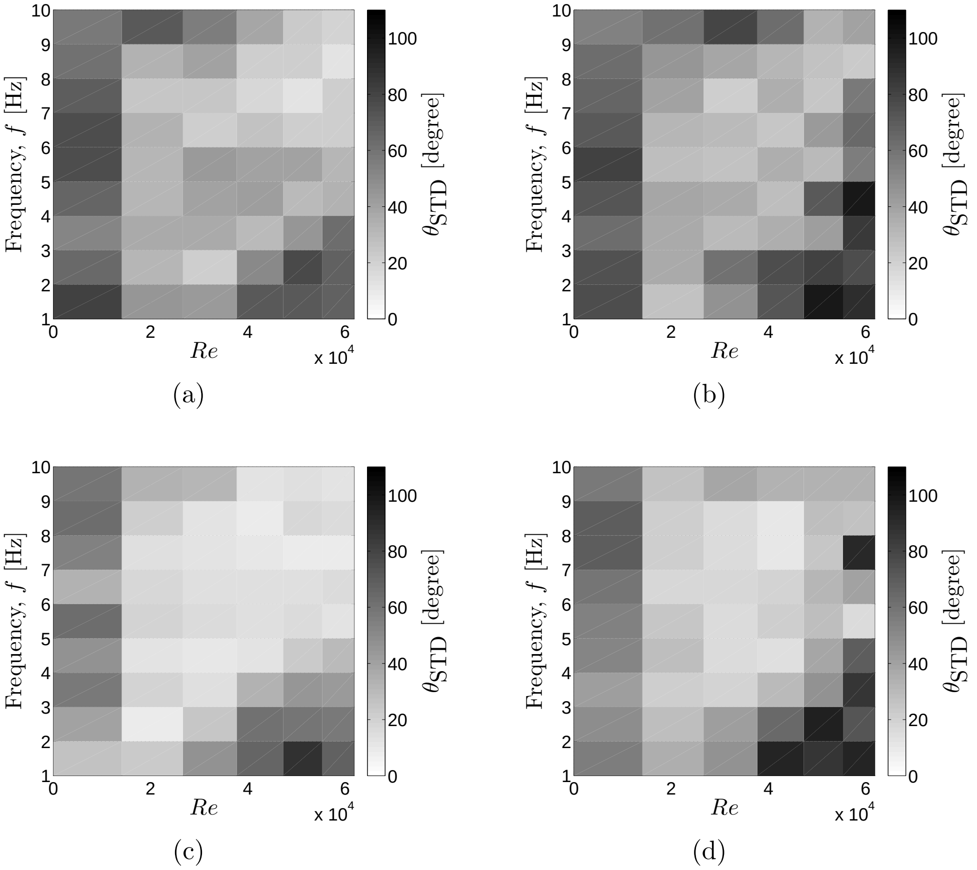

(a) (b)

(c) (d)

Figure 3.32: The influence of frequency and Reynolds number on STD of phase of the triggered pressure data at the chamber length ratio $\frac{L}{D}$=3. Without center body, (a) CW, (b) CCW actuation. With center body, (c) CW and (d) CCW actuation.

All diagrams have an similar pattern such that the deviation (θ_{STD}) increases at the right bottom and and left top corner in $Re - f$ plane. In other words, low frequency actuation is not able to manipulate flow at high Reynolds number and vise vera. Having a similar θ_{STD} pattern in the $Re - f$ plane allows to average all (5(Chamber length) × 2(CW,CCW)) ten diagrams (Figure 3.29 to 3.29) resulting in general phase-diagram for actuation effectiveness on a precessing jet shown in Figure 3.34. Strouhal number corresponding to the actuation frequency (Equation 2.5) is also plotted in Figure 3.34. Again, the light zones indicate the effective actuation on controlling the precessing jet while dark zones indicate poor actuation effectiveness. As expected, the Strouhal number range in which the flow can be effectively actuated matches with $0.002 \leq St_d \leq 0.006$ associated with the natural Strouhal number of the precession (based on the nozzle diameter (d)). This is a region in $Re - f$ plane

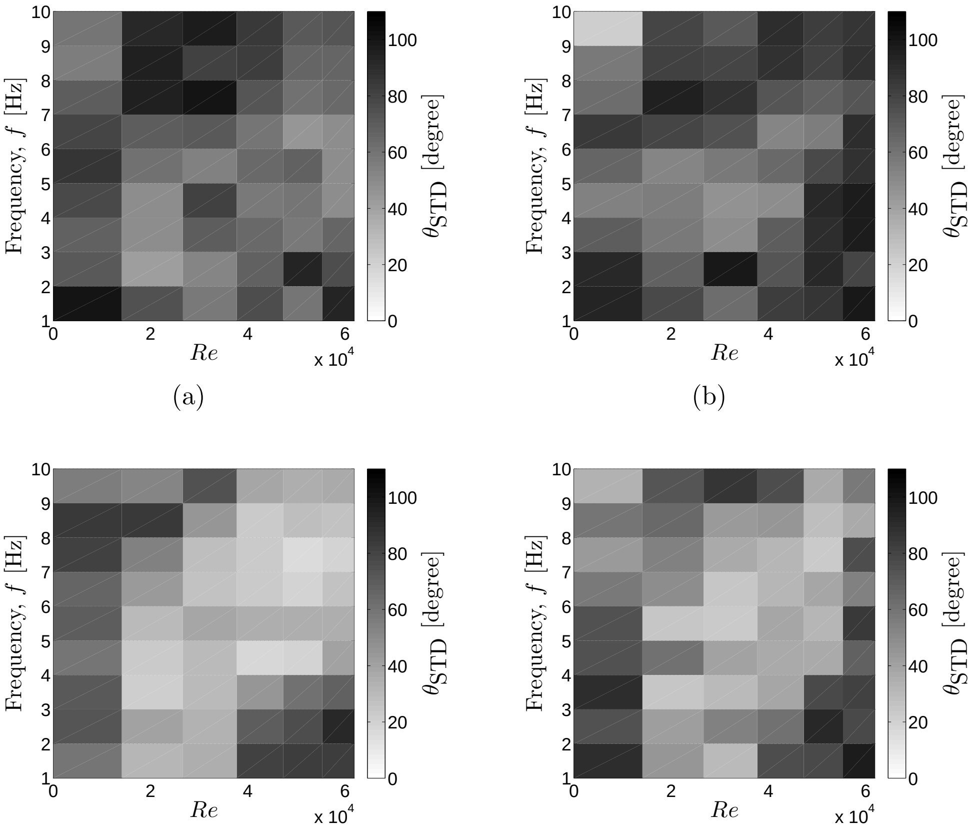

(a) (b)

(c) (d)

Figure 3.33: The influence of frequency and Reynolds number on STD of phase of the triggered pressure data at the chamber length ratio $\frac{L}{D}$=3.5. Without center body, (a) CW, (b) CCW actuation. With center body, (c) CW and (d) CCW actuation.

where the actuation can control the precession of the jet. Figure 3.34 can also be used as a basis for closed-loop control system designs as it shows actuation effectiveness range in the $Re-f$ plane for both CW and CCW actuation for $2.0 \leq \frac{L}{D} \leq 3.5$ and with and without the center body.

By increasing chamber length, θ_{STD} increases indicating that actuation effectiveness for long chambers is lower than short ones. This observation can be also confirmed by Figure 3.35. Looking more carefully at Figures 3.29 to 3.33, there are slight differences in θ_{STD} (color intensity) between with center body and no center body and between CW and CCW actuation. Having a center body decreases the deviation (θ_{STD}) indicating better control effectiveness with the center body. This effect can also be observed by comparing the overall intensity in Figure 3.34(a) and Figure 3.34(b). The deviation of CW is less that CCW actuation confirming the already observed CW preferred direction.

To examine the general trends of the influence of each of the frequency and Reynolds number independently, all Reynolds numbers in Figure 3.34 are averaged and plotted versus frequency as an actuation parameter in Figure 3.36. This figure shows that a particular band of frequencies (4-8) Hz are more effective on precession control compared to the frequencies outside of this range.

The same procedure is taken for f and Figure 3.37 demonstrates the influence of Reynolds number on precession control. At zero flow (Re=0), the deviation is significantly more than other low Reynolds numbers indicating that when the pump is turned off (Re=0), the actuation effectiveness is low. That is because the actuation has to provide not only the momentum required for precessing but also the momentum for discharging from the chamber. However, increasing Reynolds number, the deviation increases and the ability to drive the precession by actuation attenuates.

Another interesting observation based on Figure 3.37 is that the deviation of the chamber without center body under CW actuation does not decrease the actuation effectiveness for the range of $14,000 \leq Re \leq 62,000$. This can be attributed to the fact that the preferred direction of the precessing jet is more stable; so, increasing the Reynolds number does not destabilize the flow significantly compared to CCW actuation in which the precession is destabilized by forcing to change the precession direction. This effect is more obvious in the chamber without the center body because the stabilization effect of the center body is not present.

As discussed in this chapter, the phase plane representation reveals the direction and stability of the precessing jet under actuation. The direction of precession is found by integration on this plane and the the standard deviation of the phase of triggered pressure data is used for stability analysis. The stability analysis is led to a phase diagram which shows the stabilization effect of the actuation indicating the actuation in the Strouhal number corresponding to the natural Strouhal number of the precessing jet is more effective. Monitoring the flow using the phase plane can be utilized to setup a feedback control on the precessing jet in order to either stabilize or destabilize the jet precession.

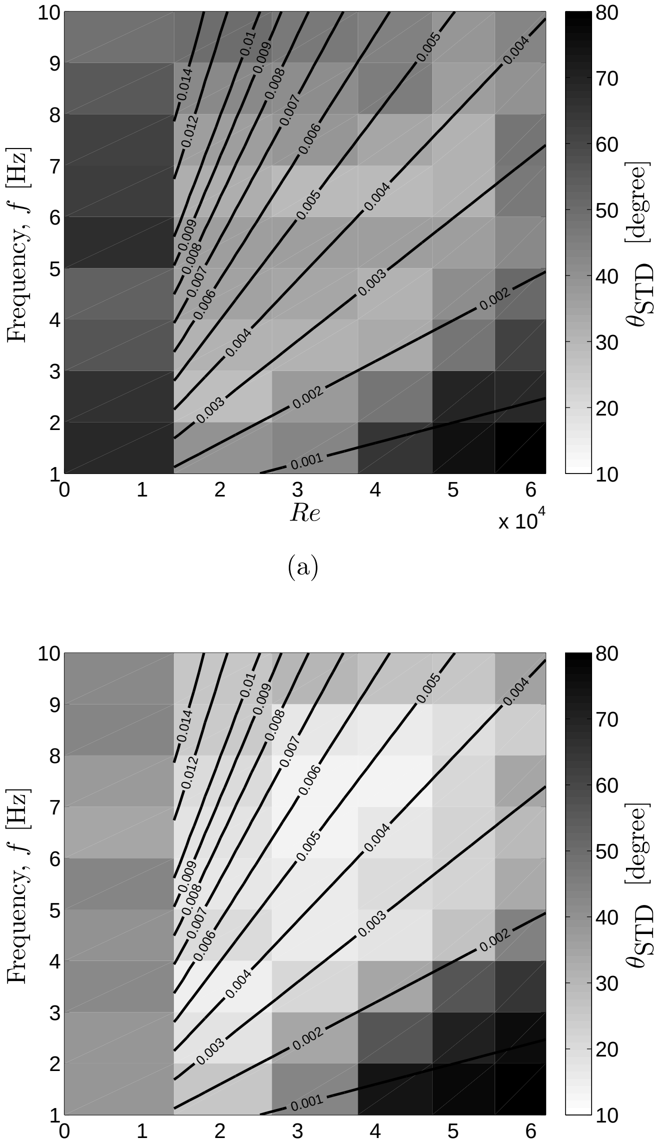

(a)

(b)

Figure 3.34: The influence of frequency and Reynolds number on STD of phase of the triggered pressure data averaged for $2.0 \le \frac{L}{D} \le 3.5$ and actuation direction for (a) without center body and (b) with center body; the contour lines show St_d on Re-f plane.

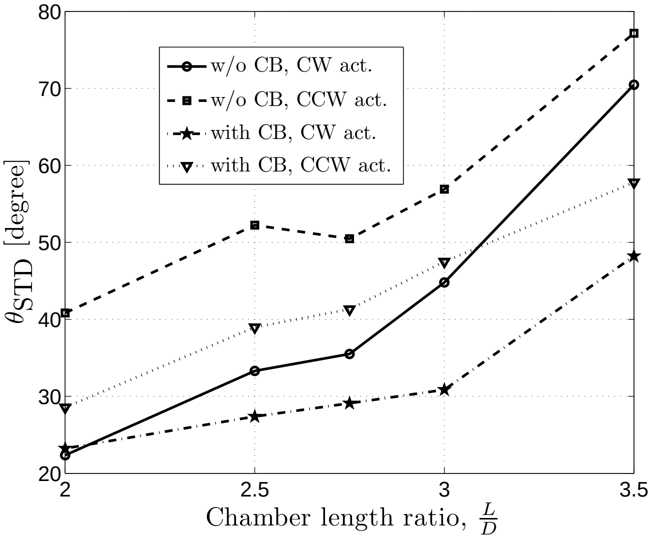

Figure 3.35: The influence of chamber length ratio ($\frac{L}{D}$) on STD of phase of the triggered pressure data averaged for all frequencies and Reynolds numbers (24).

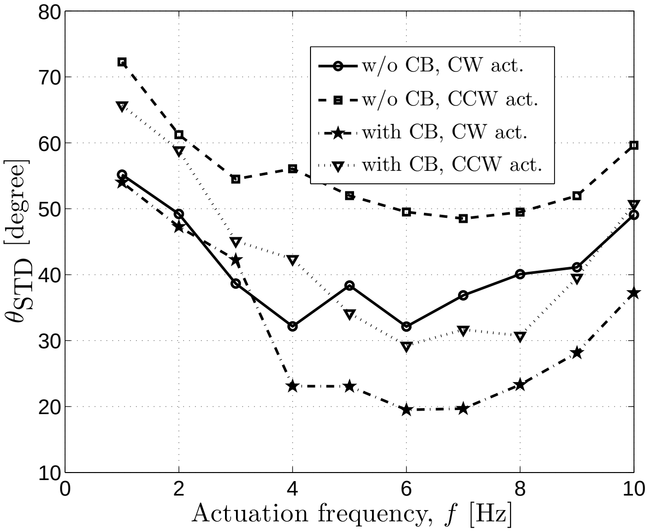

Figure 3.36: The influence of frequency f on STD of phase of the triggered pressure data averaged for all Reynolds number of and chamber lengths (23).

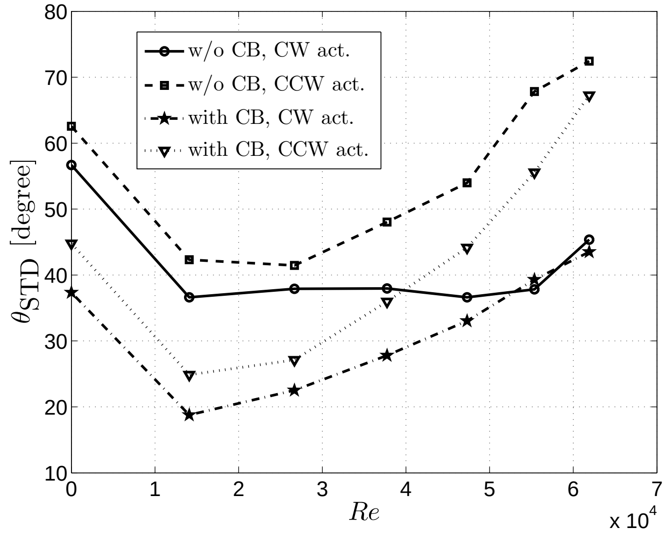

Figure 3.37: The influence of Reynolds number of on STD of phase of the triggered pressure data averaged for all frequencies and chamber lengths (22).

Chapter 4

Validation of pressure processing by S-PIV

The phase plane mapping introduced in Chapter 3 provides a tool to investigate a precessing jet under active flow control. However, no evidence is given so far to ensure this mapping simulates the actual behavior of the precessing jet. To do this, the pressure data analysis from Chapter 3 must be compared with another method. Use of S-PIV is the focus of this chapter to study the behavior of precessing jet flow at the chamber exit and then to compare the results with pressure data. This chapter contains the results of S-PIV measurements compared with pressure data. To compare the results of two methods, the centroid of precessing jet is defined using the velocity vector field and then the centroid phase is compared to the phase of precessing jet in the phase plane. The next section presents S-PIV results and then a comparison of S-PIV results with the pressure measurements is given.

4.1 S-PIV at the nozzle exit

The S-PIV hardware limits image acquisition to less than 1 Hz. However a transient study of this flow requires a sampling rate of at least 100 Hz. An alternative is to study the flow using phase-locked images. A Phased-lock S-PIV measurement system requires a trigger signal from the periodically forced flow which varies in phase about the forcing period. For this flow, possible trigger signals are the actuation input to the micro-jet solenoid injectors or the measured pressure signal output at the chamber exit. The trigger of each of the twelve injectors is chosen here and provides twelve phases for phase-locked S-PIV.Thick black lines in Figure 2.1 (Chapter 2) illustrate the trigger signals for phase-locking purposes. A chamber with a length ratio ($\frac{L}{D} = 2.5$) without center body at $Re = 38,000$ and $Re = 62,000$ is selected for S-PIV measurement. This flow is actuated at a frequency of 5 Hz in both CW and CCW directions (Table 4.1).

To take care of any possible asymmetry in the flow, each of the twelve injectors are individually used to trigger S-PIV system within different experiments. Therefore, 48 tests (12 × 2 × 2)(trigger, Reynolds number, actuation direction) are conducted. For these 48 tests, the four pressure sensors are also sampled at 1 kHz and stored. To acquire 100 trigged images, considering the sampling rate of S-PIV measurement is 1 Hz, and 30 s delay to avoid initial actuation effects and to start triggering, the actuation interval is set 130 s as shown in Figure 4.1. Figure 4.2 shows the moment when S-PIV receives the trigger signal from injector # *i* (*i*=5 is used as an example). At this moment,

Table 4.1: Test Conditions for pressure signals with S-PIV

Independent variable	**Value**
Reynolds number	38,000 and 62,000
Chamber length	2.5
Passive control	without center body
Actuation frequency	5 Hz
Actuation pattern	
(# of simultaneously firing injectors)	3
Actuation direction	CW and CCW

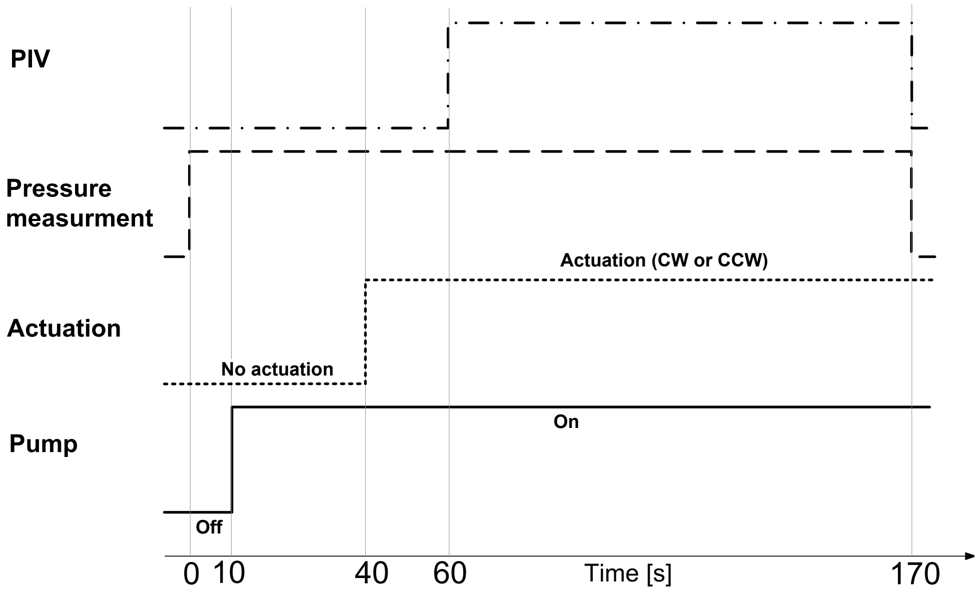

Figure 4.1: Timeline for pump, pressure and PIV measurements and actuation operations.

the injector $\#i$ receives a command to start to open while the injector $\#(i-3)$ for CW pattern and injector $\#(i+3)$ for CCW pattern are commanded to close (see Figure 4.2). To have a definition of triggering state, when the injector $\# i$ is triggered, injectors $\# (i-1),(i-2),(i-3)$ and $\# (i+1),(i+2),(i+3)$ are selected for CW and CCW patterns, respectively. These are chosen since injector 2 in CW and injector 8 in CCW actuation of Figure 4.2 have not yet had a chance to turn off. The injection line is defined as shown in Figure 4.2 as a reference phase of the location of the actuation for comparison with the location of jet obtained by S-PIV and pressure data and is the opposite side of the center of the active injectors. The angle of the centroid of the precessing jet (θ) and the relative angle between the injection line and the centroid (β) are depicted graphically in Figure 4.3. The angle β represents the phase lag of the jet compared to the actuation.

To study any asymmetry effect or preferred deflection of the precessing jet as it discharges into the tank, 1000 images are taken randomly without actuation for low ($Re = 38,000$) and high ($Re = 62,000$) Reynolds numbers. Figure 4.4(a) and 4.4(b) show the average value of out-of-plane velocity (W) for $Re = 38,000$ and $Re = 62,000$, respectively. The solid black circle is the location of the chamber exit and "+" is the center of the chamber. The corresponding out-of-plane RMS velocity (w') is shown in Figure 4.4(c) and 4.4(d). Both figures confirm that while there is a symmetry about the y-axis, the precessing jet is deflected slightly upwards. This effect is a biased shift of the precessing jet from the chamber axis due to an asymmetry in the geometry which will also appear later with actuation. A conditional averaging method developed recently [15] finds the centroid of the high velocity region in the jet (see Figure 4.3) for each image and then rotates the entire flow field by $(90^\circ-\theta)$ where θ is the centroid phase to line up all the image centroid phases. This rotation of all instantaneous flow fields and then averaging reveal the kidney-bean shape of precessing jet as shown Figure 4.4(e) and 4.4(f). Here, the phase of the precessing jet is not known as there is no forcing.

Twelve trigger signals coming from each of the injectors are examined next. Figures 4.5 to 4.8 illustrate an example of instantaneous flow field for all twelve triggers with in-plane velocity vector field in right and out-of-plane velocity in left for high Reynolds number ($Re = 62,000$) at CW actuation. One hundred instantaneous velocity fields are collected for each test condition.

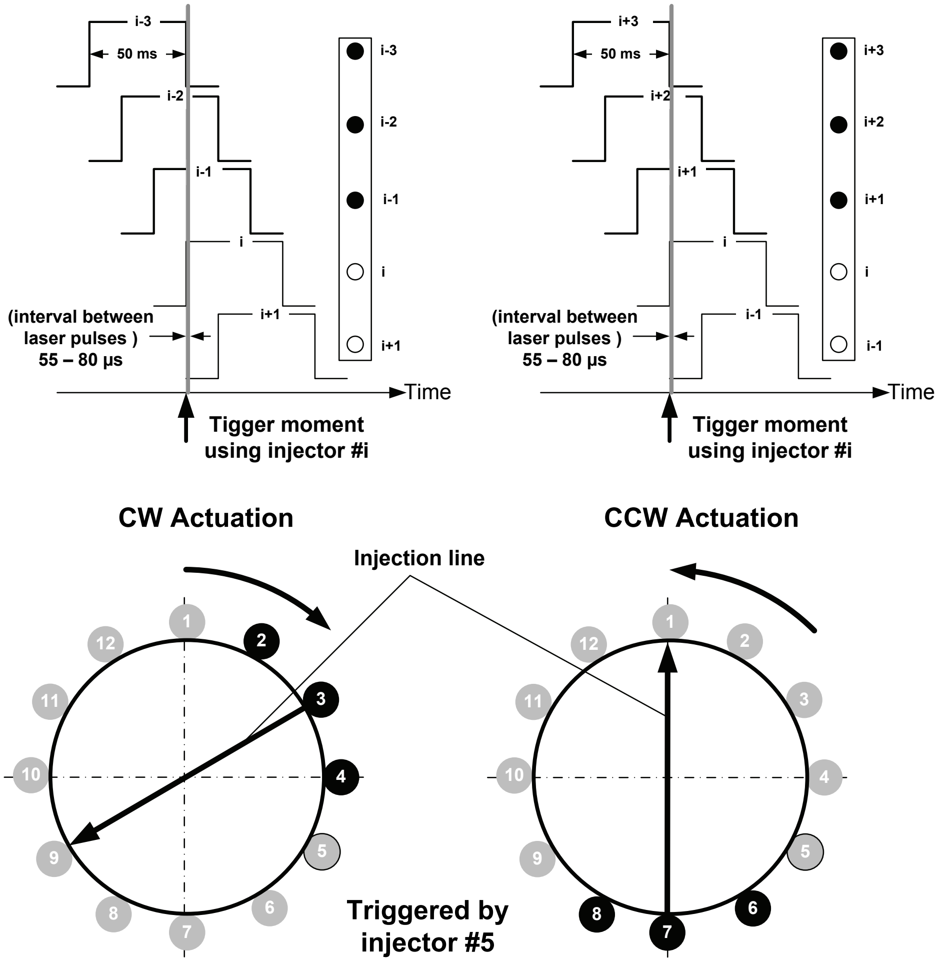

Figure 4.2: The actuation pattern in terms of the label of triggered injector at the time of sending the trigger signal to S-PIV system.

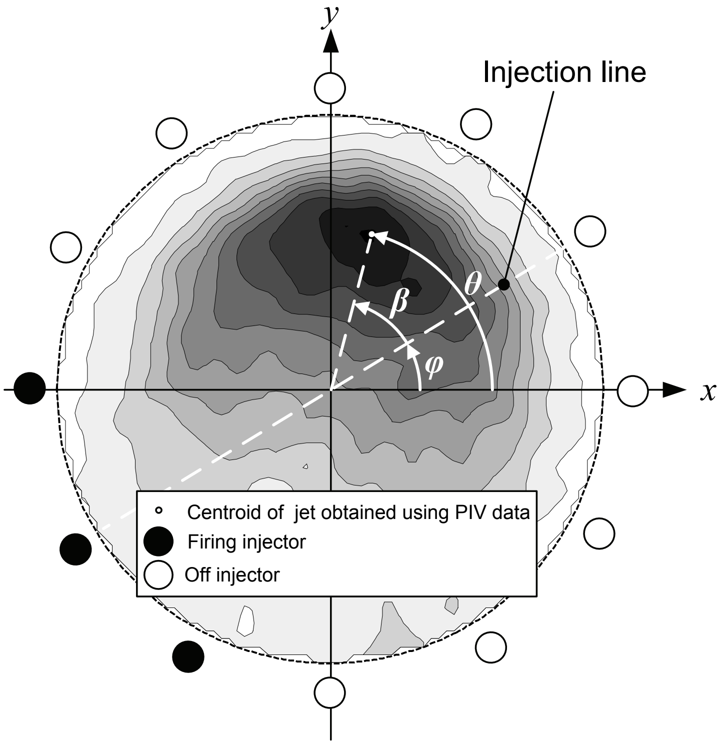

Figure 4.3: The definition of phase and lag between the centroid of jet obtained by S-PIV data and the injection line.

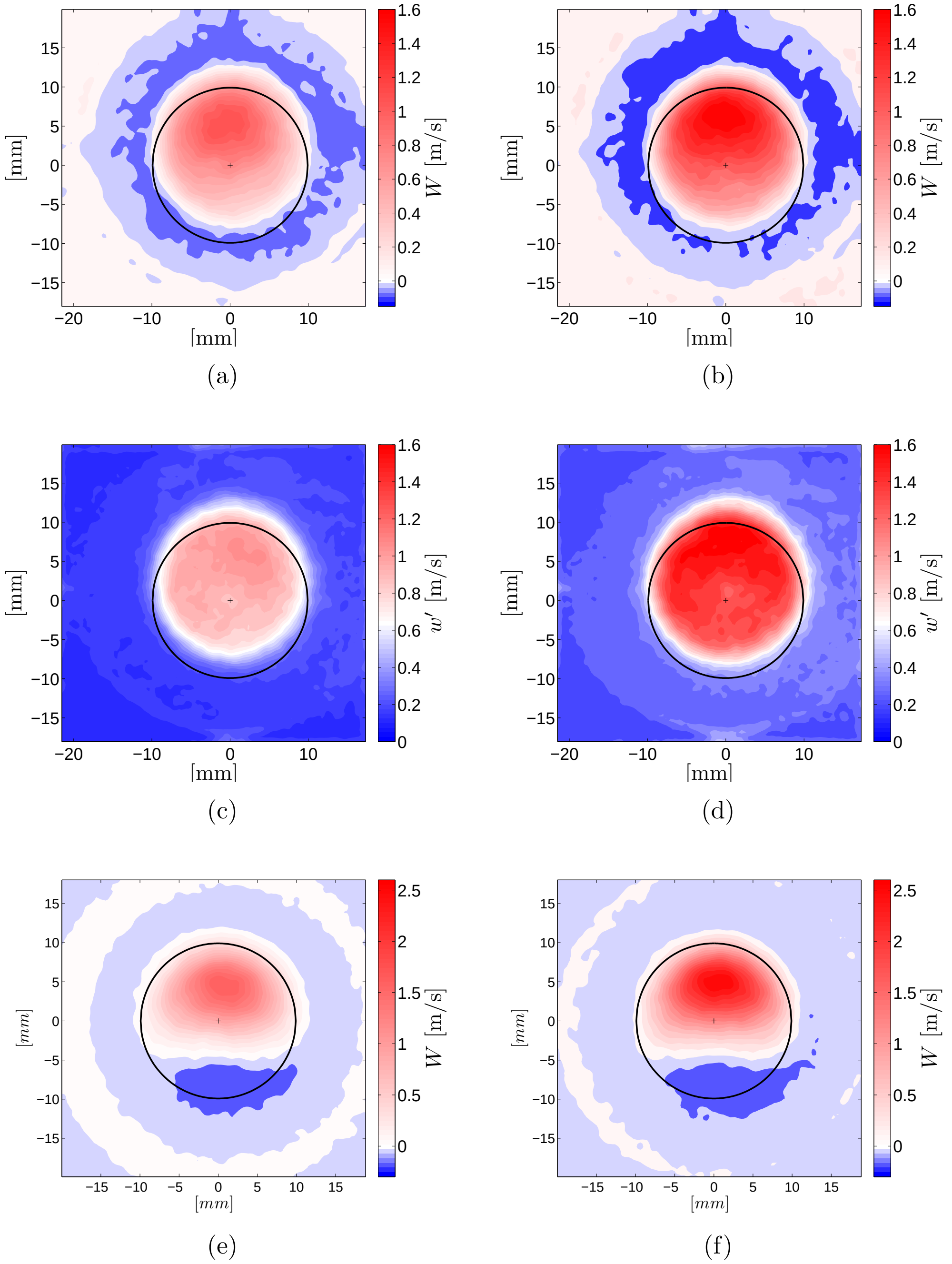

(a) (b) (c) (d) (e) (f)

Figure 4.4: Outflow velocity of a chamber with a length ratio $\frac{L}{D}$ = 2.5 and without the center body, (a) average value (W) at Re=38,000 (b) average value (W) at Re=62,000 (c) RMS value (w') at Re=38,000 (d) RMS value (w') at Re=62,000 (e) conditional average (W) at Re=38,000 (f) conditional average (W) at Re=62,000.

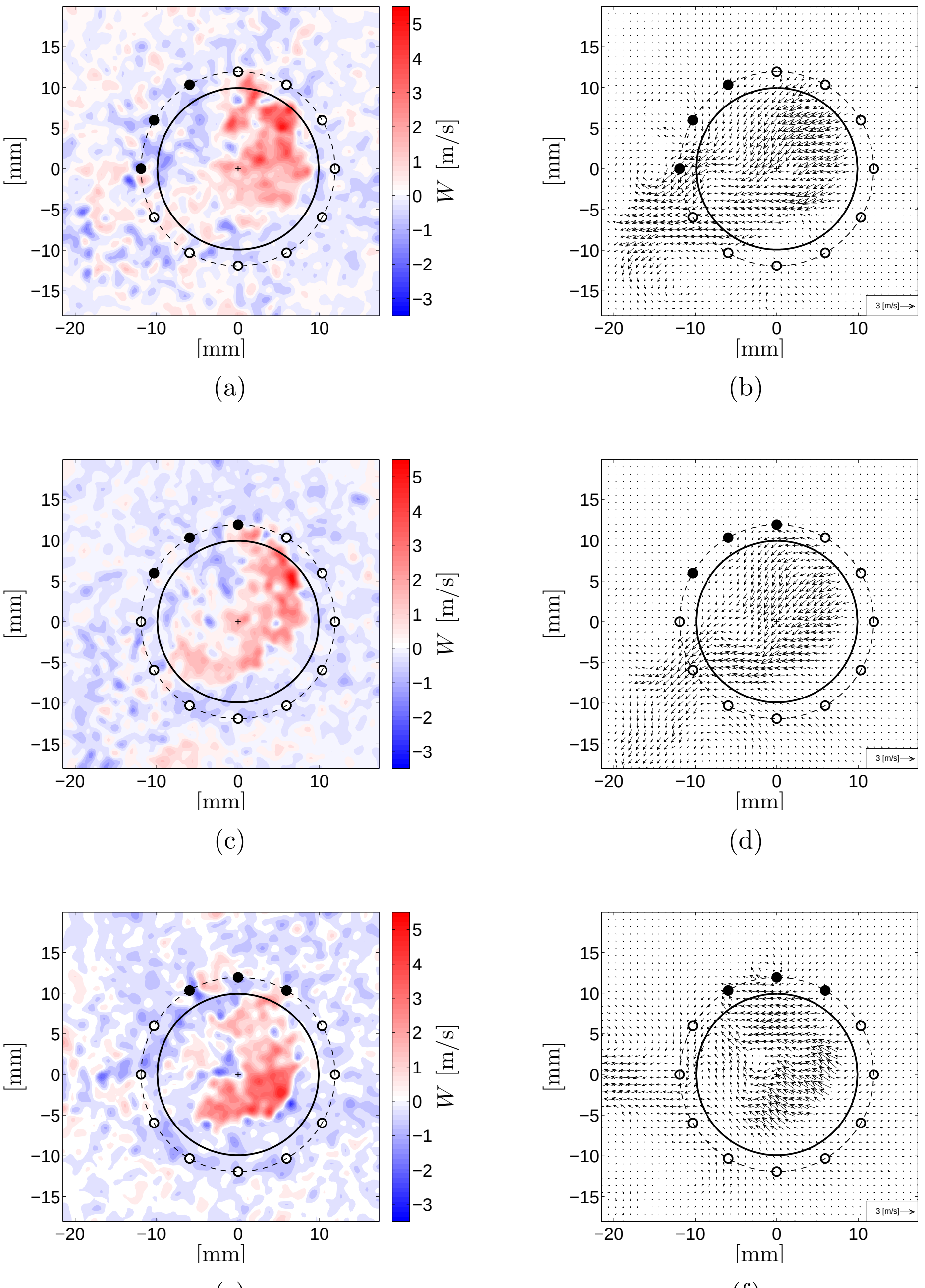

(a) (b)

(c) (d)

(e) (f)

Figure 4.5: Instantaneous outflow (out-of-plane) velocity and in-plane velocity vector field of a chamber with a length ratio $\frac{L}{D}$ = 2.5 and without the center body at Re=62,000 with CW actuation, triggered by injector (a) & (b) 1 (c) & (d) 2 (e) & (f) 3.

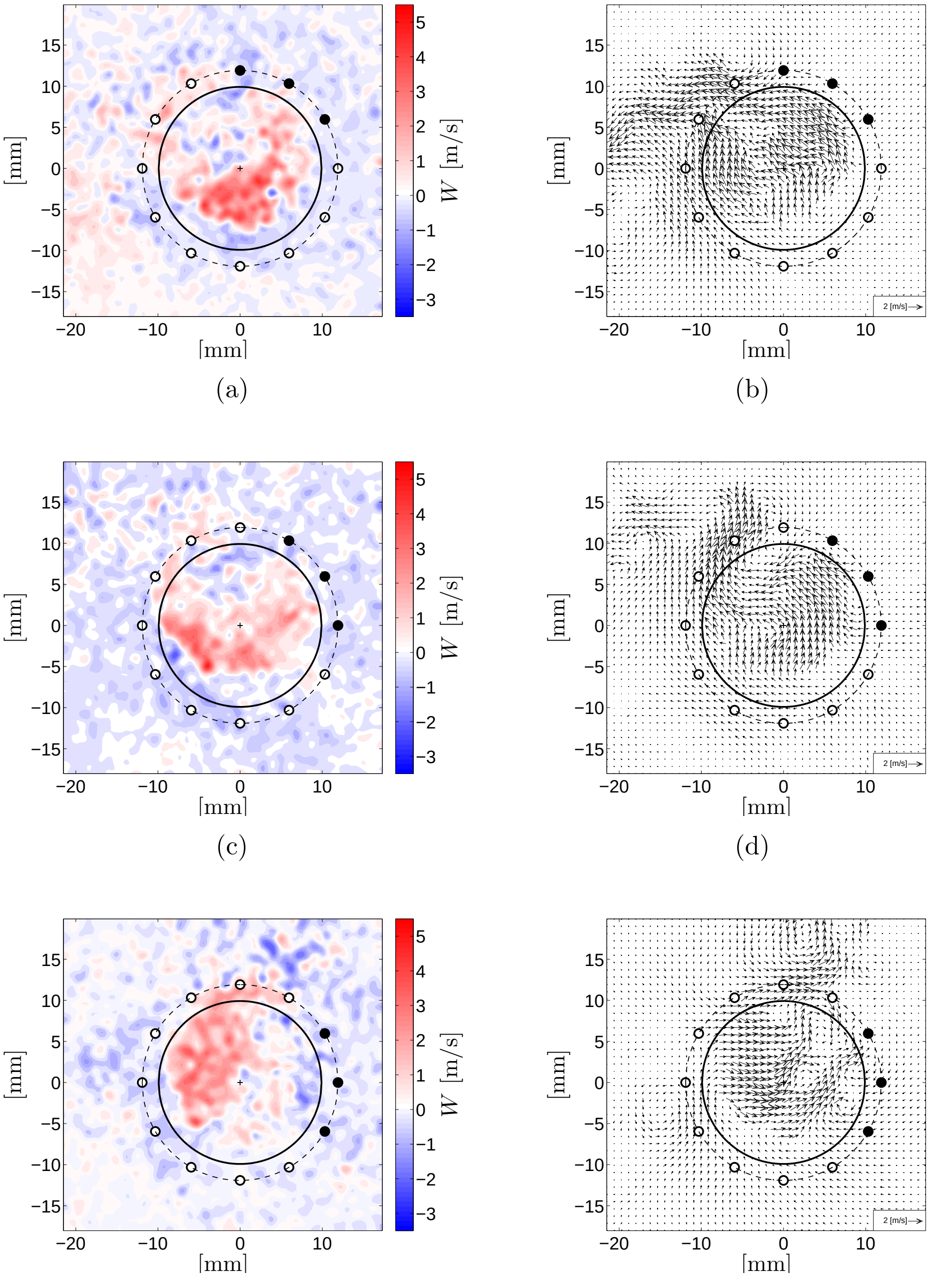

(a) (b)

(c) (d)

(e) (f)

Figure 4.6: Instantaneous outflow (out-of-plane) velocity and in-plane velocity vector field of a chamber with a length ratio $\frac{L}{D}$ = 2.5 and without the center body at Re=62,000 with CW actuation, triggered by injector (a) & (b) 4 (c) & (d) 5 (e) & (f) 6.

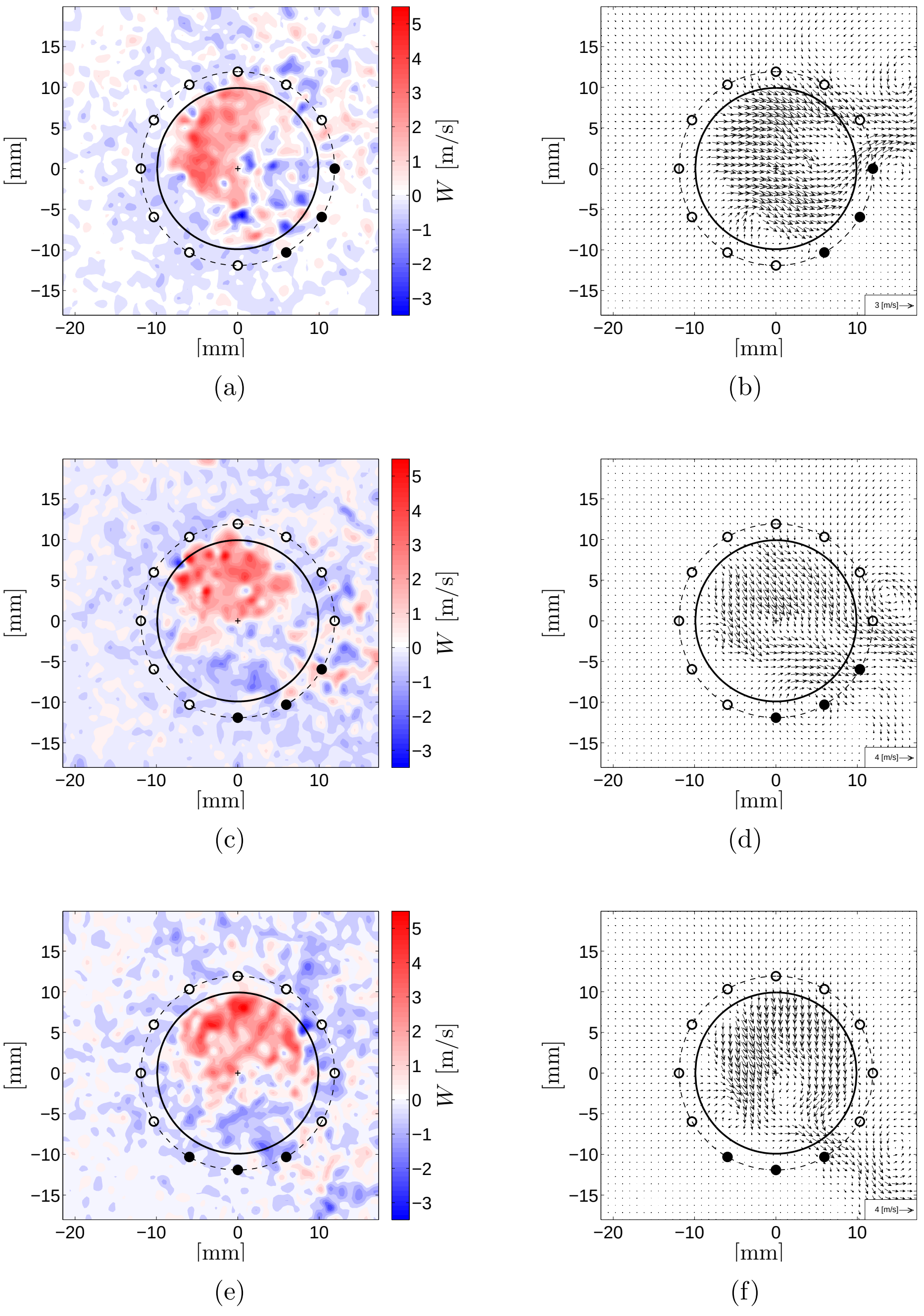

(a) (b) (c) (d) (e) (f)

Figure 4.7: Instantaneous outflow (out-of-plane) velocity and in-plane velocity vector field of a chamber with a length ratio $\frac{L}{D}$ = 2.5 and without the center body at Re=62,000 with CW actuation, triggered by injector (a) & (b) 7 (c) & (d) 8 (e) & (f) 9.

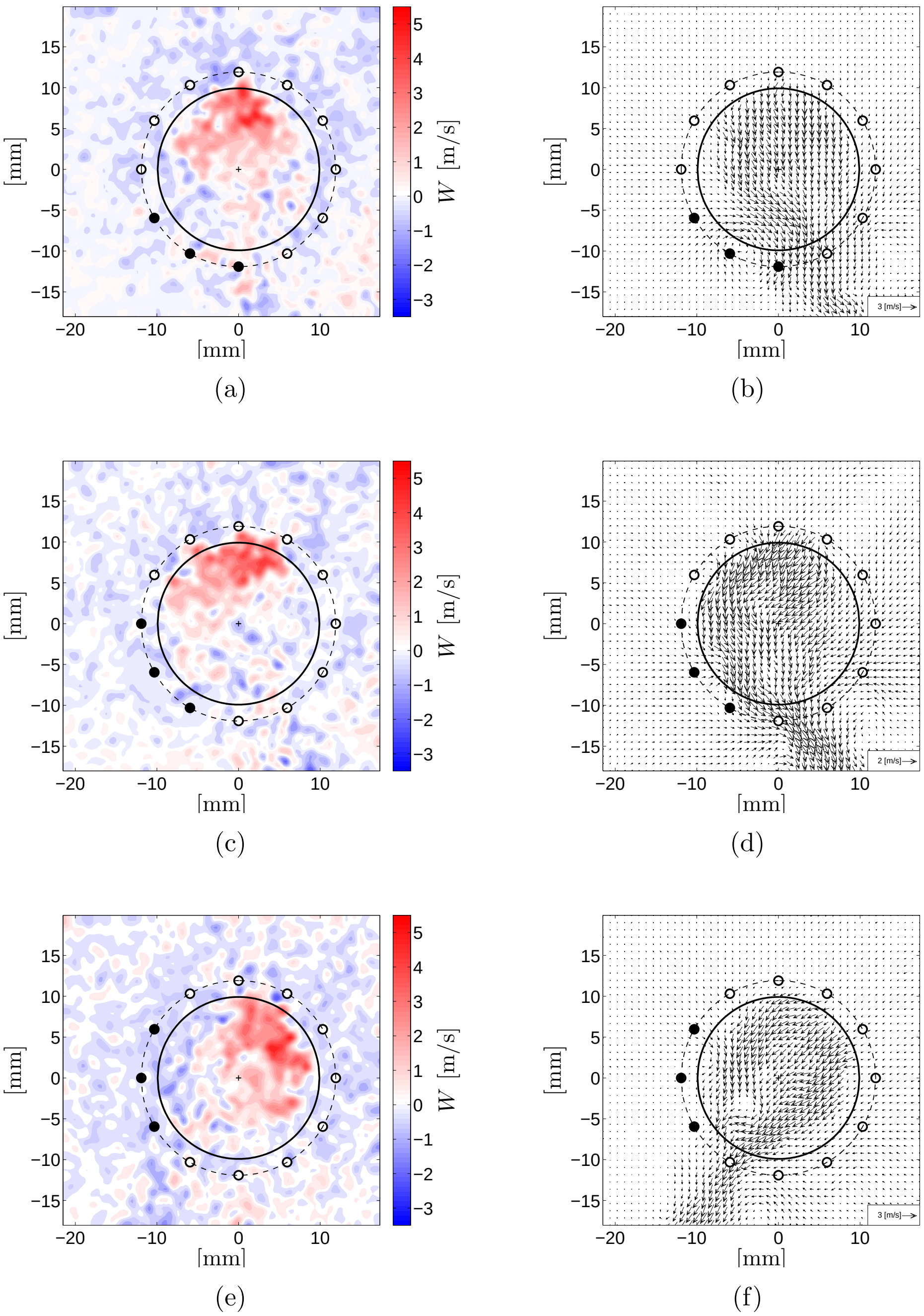

(a) (b)

(c) (d)

(e) (f)

Figure 4.8: Instantaneous outflow (out-of-plane) velocity and in-plane velocity vector field of a chamber with a length ratio $\frac{L}{D}$ = 2.5 and without the center body at Re=62,000 with CW actuation, triggered by injector (a) & (b) 10 (c) & (d) 11 (e) & (f) 12.

Looking at Figures 4.5 to 4.8 in-plane and out-of-plane velocity reveals the trajectory of large scale structure of precessing jet. The injection of secondary flow through actuation pushes the large scale structure to the opposite side of the chamber wall while the presence of lip deflects the precessing jet to its opposite direction again as it discharges (see Figure 4.9).

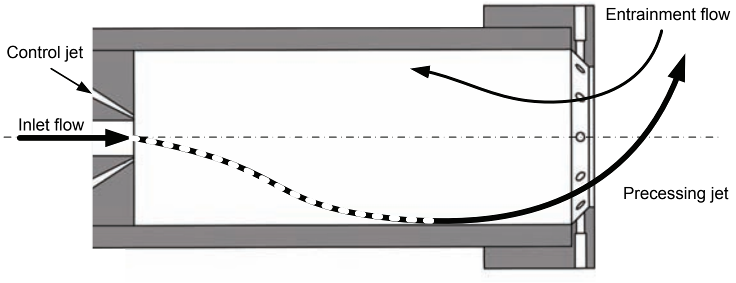

Figure 4.9: The schematic representation of flow behavior as it discharges.

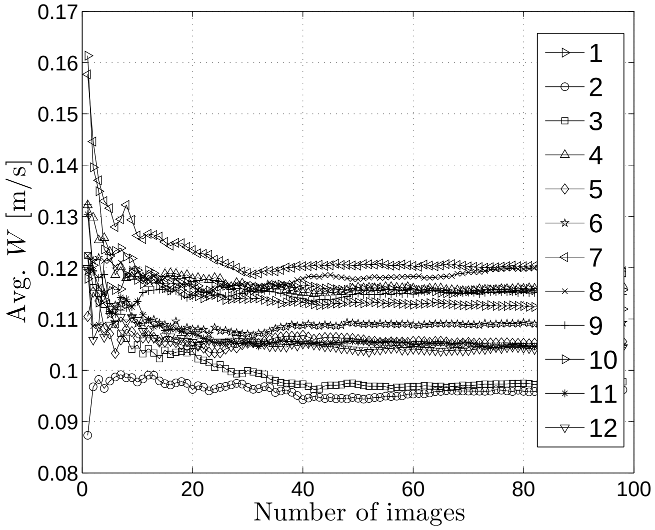

Figure 4.10: Average outflow velocity of a chamber with a length ratio $\frac{L}{D}$ = 2.5 and without the center body over the entire flow field in terms of the number of S-PIV snapshots which are used for averaging at Re=38,000 and CW actuation. The labels represent the trigger state (the label of injector used for triggering).

Having one hundred phase-locked instantaneous flow field for each test point allows the average flow behavior to be examined. To validate that one hundred instantaneous flow field images do represent the average flow, the average out-of-plane velocity versus the number of instantaneous images used in averaging is plotted in Figure 4.10. At greater than 50 images, the average value of out-of-plane velocity does not fluctuate significantly in Figure 4.10 and is almost same as the number of image points increases indicating that one hundred images is sufficient for the average.

Figure 4.11 and Figure 4.12 illustrate the average (W) and RMS (w') outflow jet velocity actuated by CW and CCW actuation at $Re = 38,000$ and $Re = 62,000$ for a particular trigger state where the firing injectors are at the top of the nozzle inlet. The effect of increasing Reynolds number is clearly understood by comparing the maximum velocities in Figure 4.11(a) and Figure 4.11(b) with Figure 4.11(c) and Figure 4.11(d). Also the phase of the precessing jet indicates the direction of the precession (this will be discussed later in more detail). The same trend is observed in RMS velocities in Figure 4.12. It is concluded from Figure 4.11 and Figure 4.12 that the general shape of the precessing jet is similar at both low and high Reynolds numbers and actuation direction. Therefore, in this chapter, only the results of $Re = 62,000$ in CW actuation is reported and the average and RMS velocities of the rest of the test points are given in Appendix E.3.

The average of out-of-plane velocity (W) and RMS (w') for all triggers at $Re = 62,0000$ and CW actuation are shown in Figures 4.13, 4.14 and Figures 4.15, 4.16, respectively. These figures show that there is a correlation between the phase of jet centroid and trigger phase. For example, when the injectors located at the left side fire as shown in Figure 4.13(f), the precessing jet tends toward the opposite side and similar behavior can be seen in all trigger cases.

The RMS velocity reveals not only the location of kidney-bean shape but also the deflection direction of precessing jet such that the precessing jet carries more RMS value in the deflected direction. For instance, Figure 4.16(b) shows that the large scale structure of flow deflected towards right-down while the precessing jet is located at top-left side. Average and RMS velocities (W, w') for $Re = 62,000$ in CCW actuation and also $Re = 38,000$ in both CW and CCW directions are given in Appendix E.3.

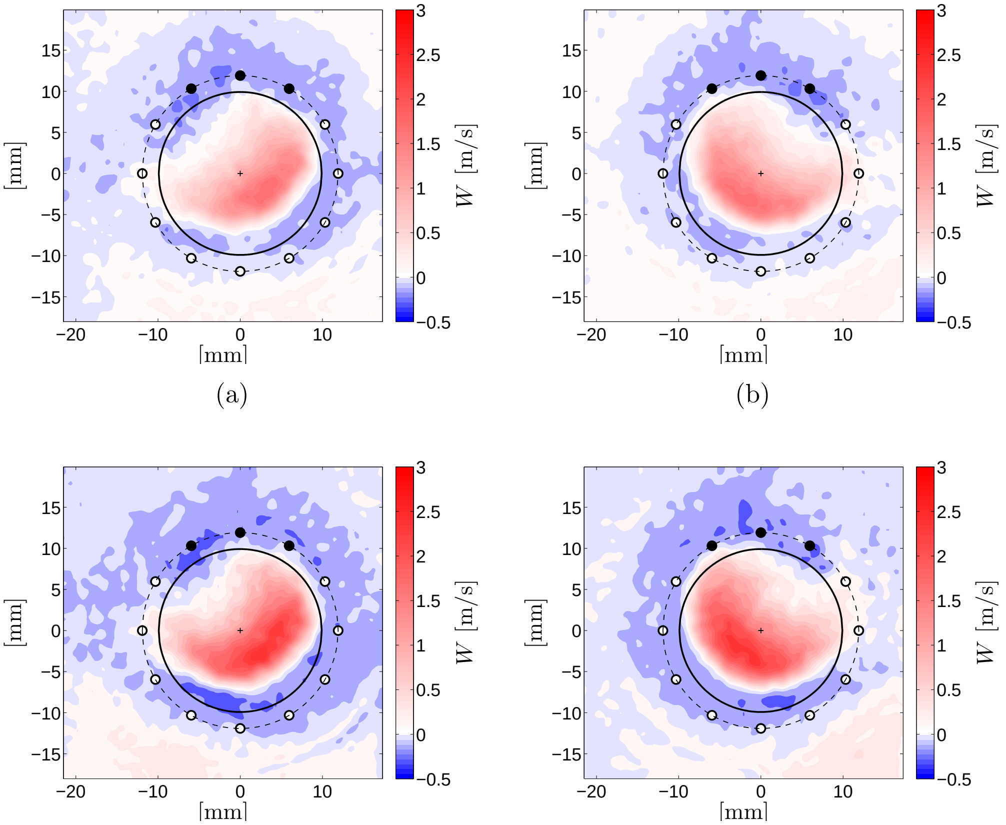

(a) (b)

(c) (d)

Figure 4.11: Phase-locked average outflow velocity for $\frac{L}{D}$ = 2.5, without center body at (a) Re=38,000, CW actuation and phased-locked by injector 3 (b) Re=38,000, CCW actuation and phased-locked by injector 11 (c) Re=62,000, CW actuation and phased-locked by injector 3 (d) Re=62,000, CCW actuation and phased-locked by injector 11.

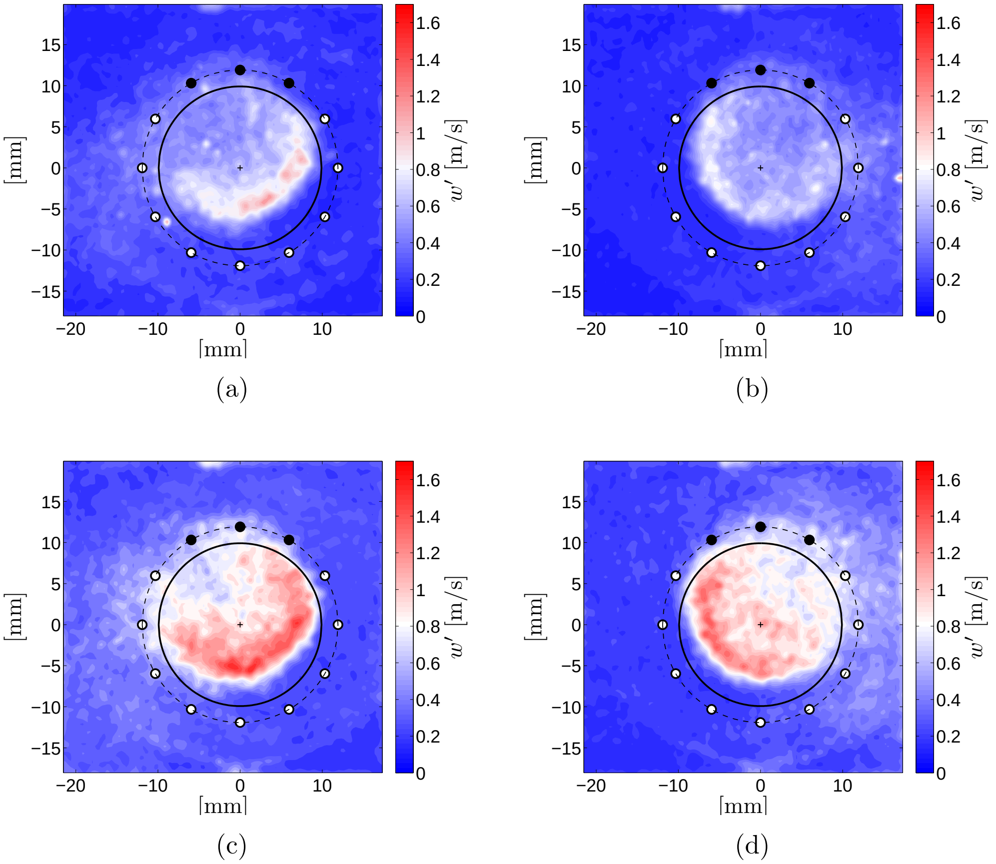

Figure 4.12: Phase-locked RMS outflow velocity for $\frac{L}{D}$ = 2.5, without center body at (a) Re=38,000, CW actuation and phased-locked by injector 3 (b) Re=38,000, CCW actuation and phased-locked by injector 11 (c) Re=62,000, CW actuation and phased-locked by injector 3 (d) Re=62,000, CCW actuation and phased-locked by injector 11.

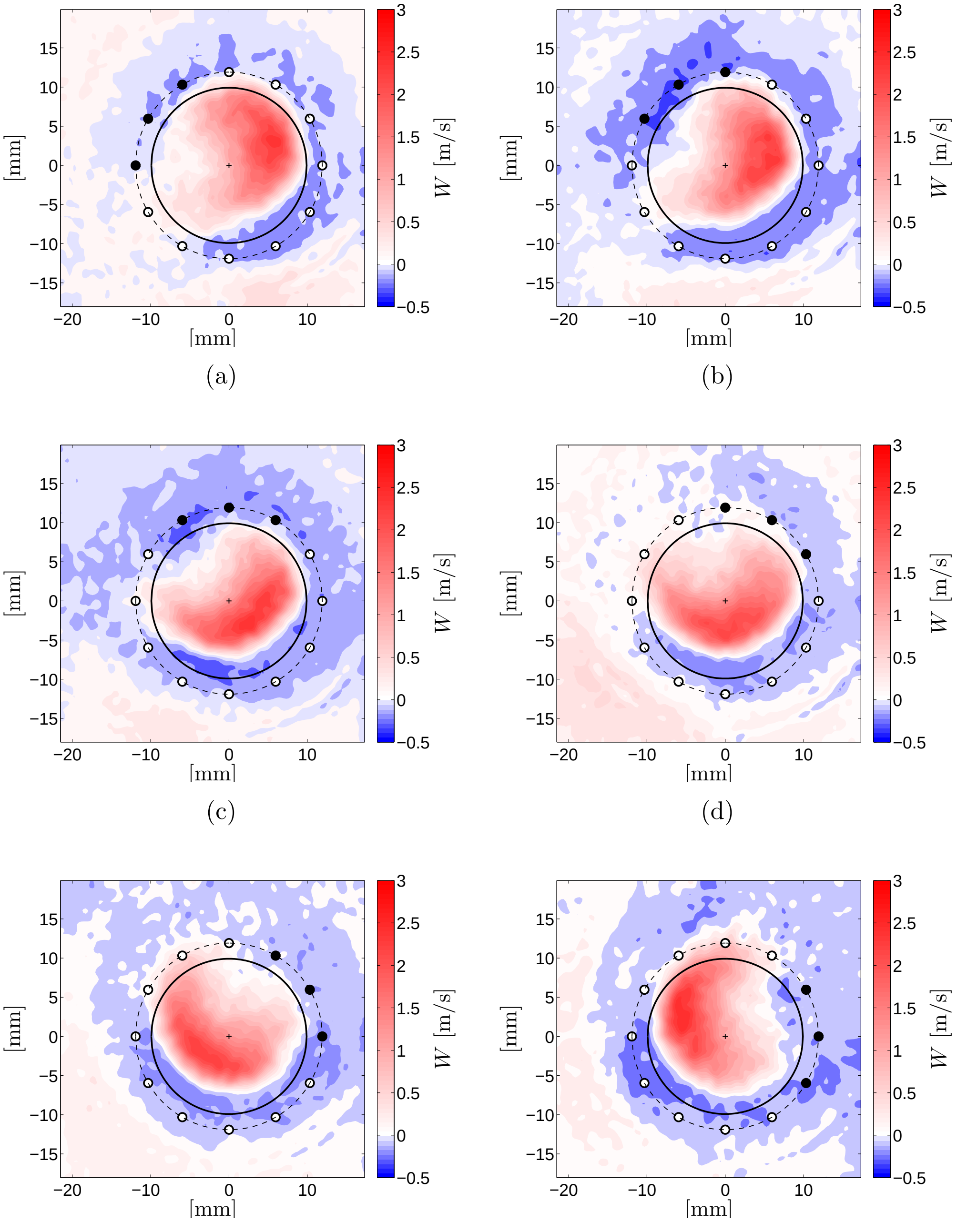

Figure 4.13: Phase-locked average outflow velocity for $\frac{L}{D}$ = 2.5 and without the center body at Re=62,000 and CW actuation, phased-locked by injector (a) 1 (b) 2 (c) 3 (d) 4 (e) 5 (f) 6.

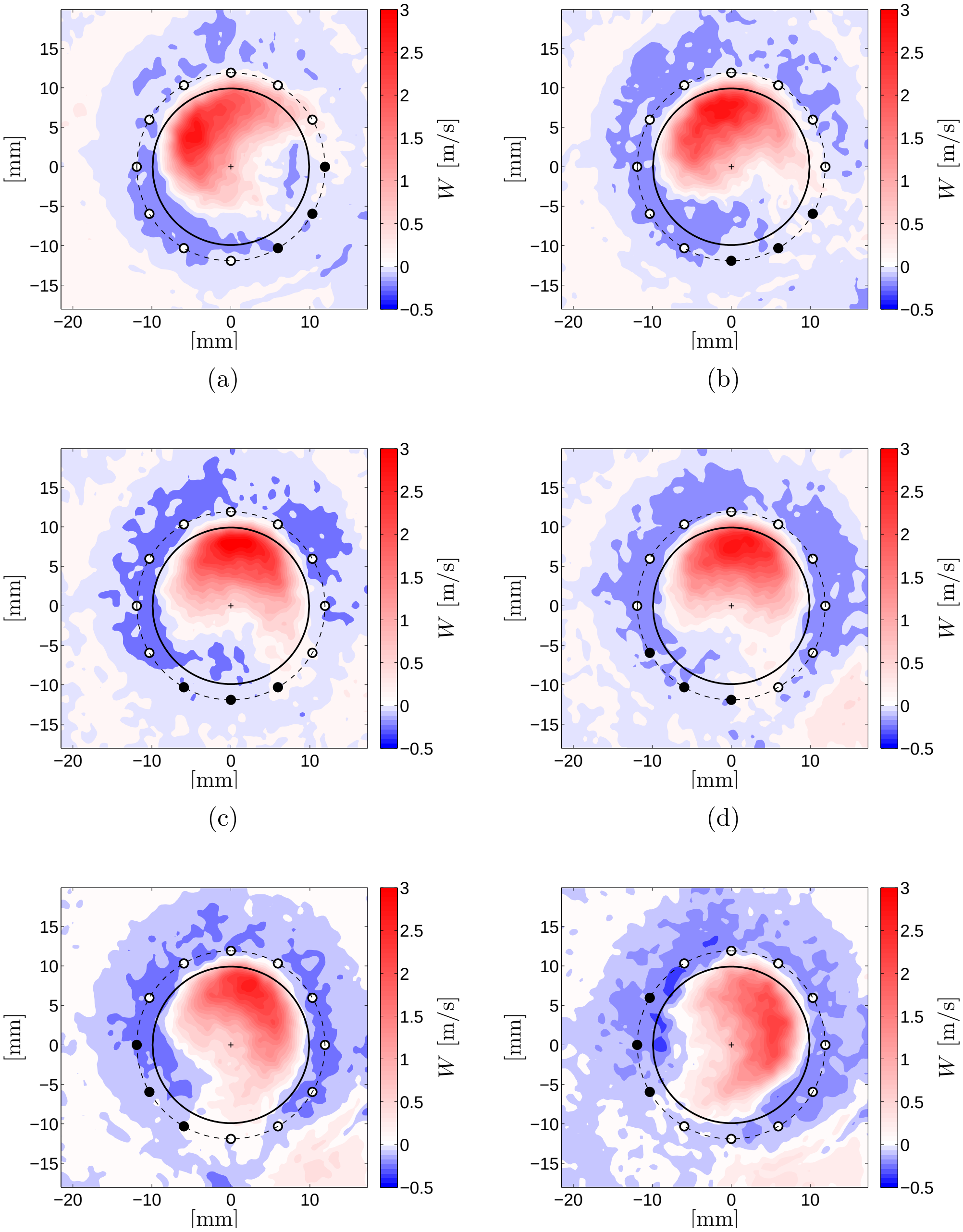

(a) (b) (c) (d) (e) (f)

Figure 4.14: Phase-locked average outflow velocity for $\frac{L}{D}$ = 2.5 and without the center body at Re=62,000 and CW actuation, phased-locked by injector (a) 7 (b) 8 (c) 9 (d) 10 (e) 11 (f) 12.

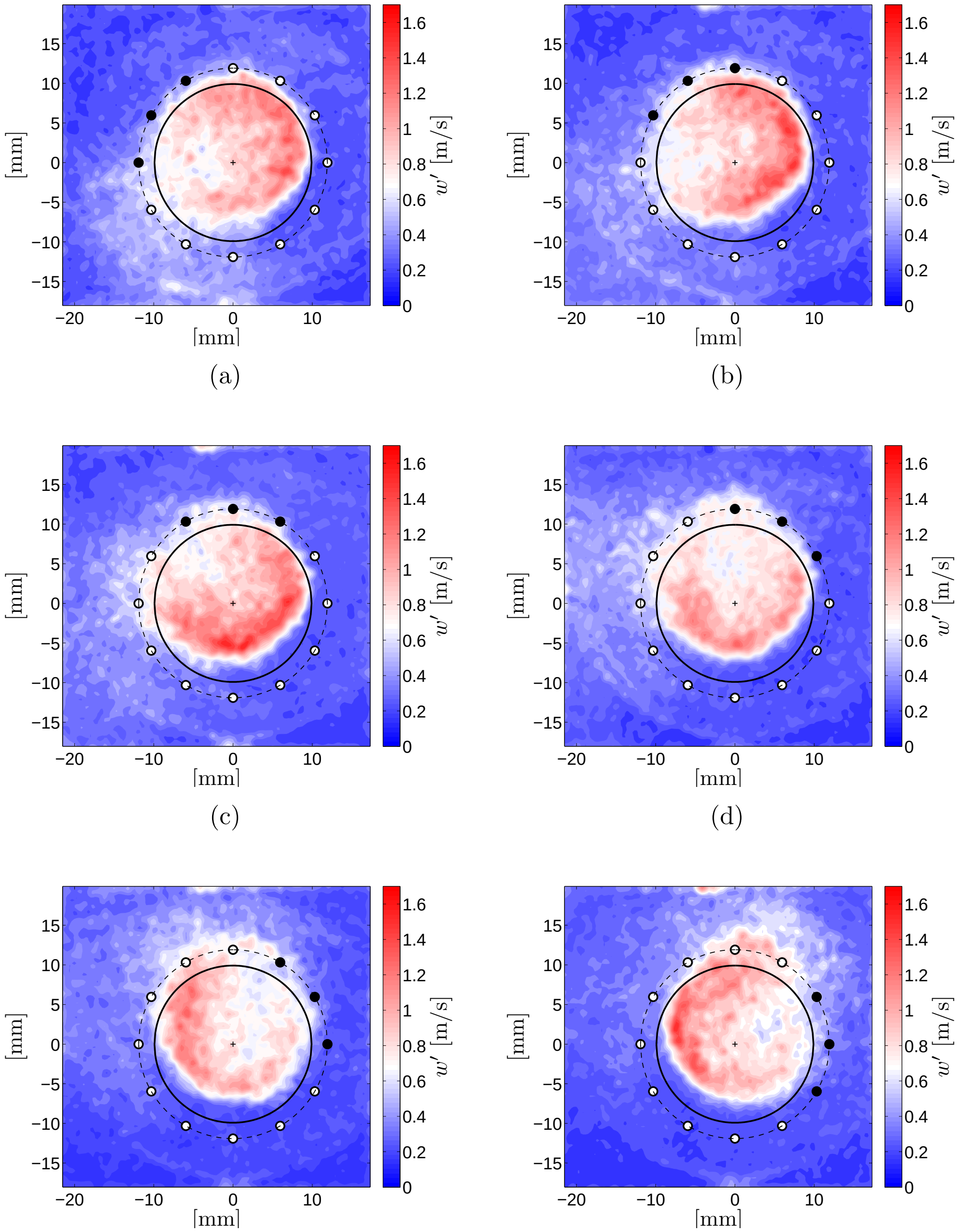

(a)

(b)

(c)

(d)

(e)

(f)

Figure 4.15: Phase-locked RMS outflow velocity for $\frac{L}{D}$ = 2.5 and without the center body at Re=62,000 and CW actuation, phased-locked by injector (a) 1 (b) 2 (c) 3 (d) 4 (e) 5 (f) 6.

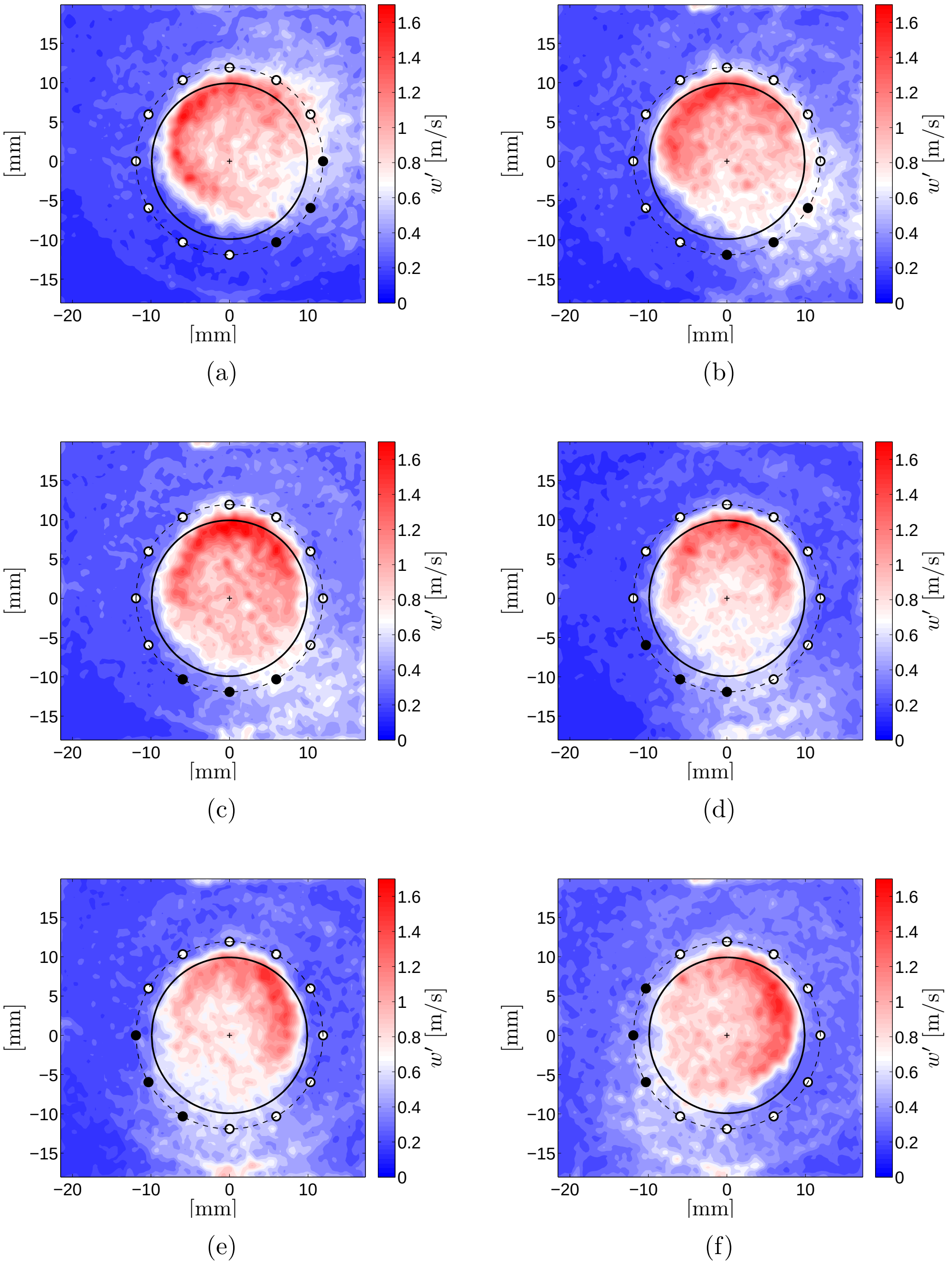

(a) (b) (c) (d) (e) (f)

Figure 4.16: Phase-locked RMS outflow velocity for $\frac{L}{D}$ = 2.5, at Re=62,000 and CW actuation, phased-locked by injector (a) 7 (b) 8 (c) 9 (d) 10 (e) 11 (f) 12.

By comparing Figure 4.13 and 4.14 (actuated) with Figure 4.4(c) and 4.4(d) (without actuation) it can be seen that actuation changes the kidney-bean cross section shape of the precessing jet, introduced in Figure 4.4(e) and 4.4(e), to a paisley shape (or a twisted teardrop). The direction of precession can be revealed by spatial smoothing of phase-locked average axial velocity (8×8 smoothing) in the actuated flow. An example of smoothed axial velocity is given in Figure 4.17 for both $Re = 38,000$ and $Re = 62,000$ and CW and CCW actuation directions. They clearly show the precession direction such that the narrow side is the leading edge and the droplet side is the tailing part of the precessing jet.

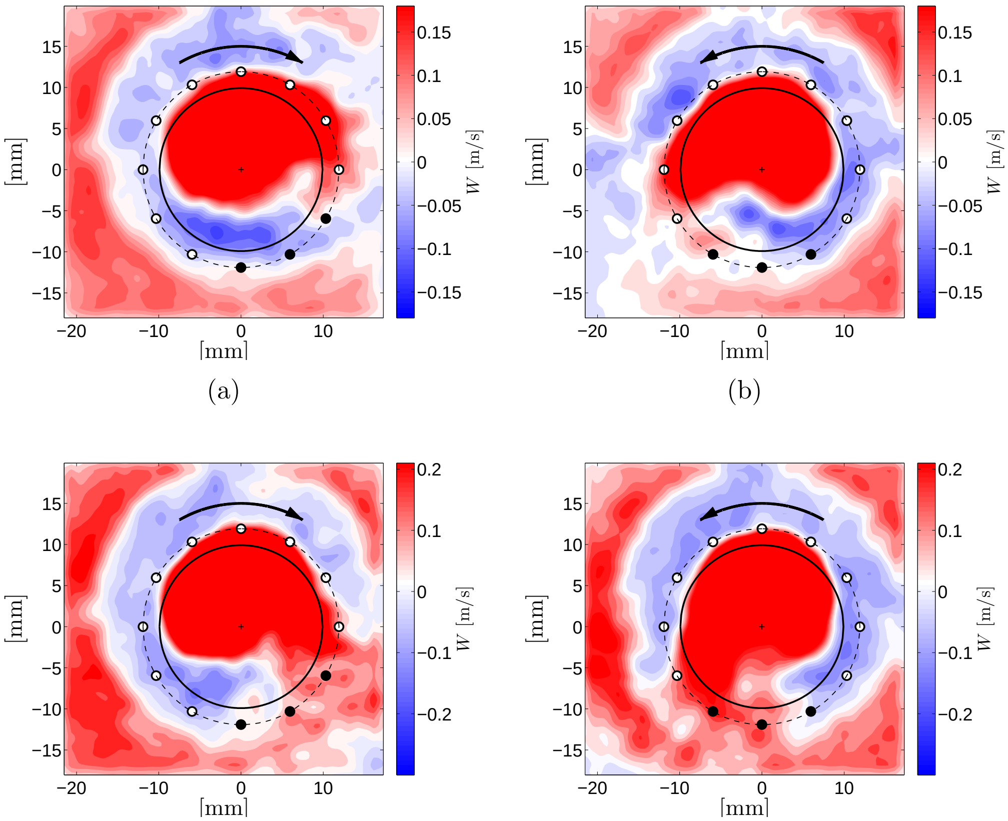

(a) (b)

(c) (d)

Figure 4.17: Phase-locked average outflow velocity for $\frac{L}{D} = 2.5$ and without the center body (spatial smoothed) at (a) Re=38,000 and CW actuation (triggered by injector 8) (b) Re=38,000 and CCW actuation (triggered by injector 5) (c) Re=62,000 and CW actuation (triggered by injector 8) (d) Re=62,000 and CCW actuation (triggered by injector 5). The arrow indicates the actuation direction.

Figure 4.18 is a schematic of the evolution of precessing jet large scale structure with and without actuation. The precessing jet appears in a kidney-bean shape at the chamber exit plane without the actuation. Once the flow is actuated, the actuation forces the flow to follow the actuation direction which in turn results in a distortion in the precessing jet shape such that the narrow side indicates the precession direction.

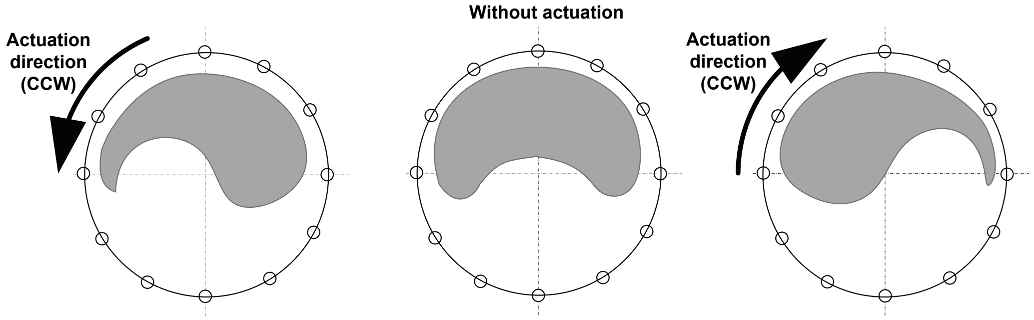

Figure 4.18: The distortion of kidney-bean shape precessing jet due to actuation in CW and CCW direction.

Phase, θ, is defined as the angle between the angle of jet centroid and the x-axis as shown in Figure 4.3 and angle β, is the phase difference between the jet centroid and the injection line (see Figure 4.3). The phase, θ along with the actuator phase, φ, for all test points are given in Figure 4.19. A schematic of the delay, (β), between the injection line and the centroid phase for CW and CCW actuation is given in Figure 4.20. A negative value indicates a lag in CCW direction while the lag is positive for CW actuation.

The delay, β, between the injection line and the centroid phase is shown in Figure 4.21 for all twelve phase angles. All twelve phase angle lags are averaged and the value of this lag is listed in Table 4.2. As expected, the lag average value is less for CW direction since it is the preferred direction of the precession for this experimental setup.

Table 4.2: The lag, β_{PIV}, between the centroid phase and the injection line obtained using S-PIV data

Re	**CW Actuation**	**CCW Actuation**
38,000	19 ± 26	-25 ± 22
62,000	18 ± 33	-20 ± 28

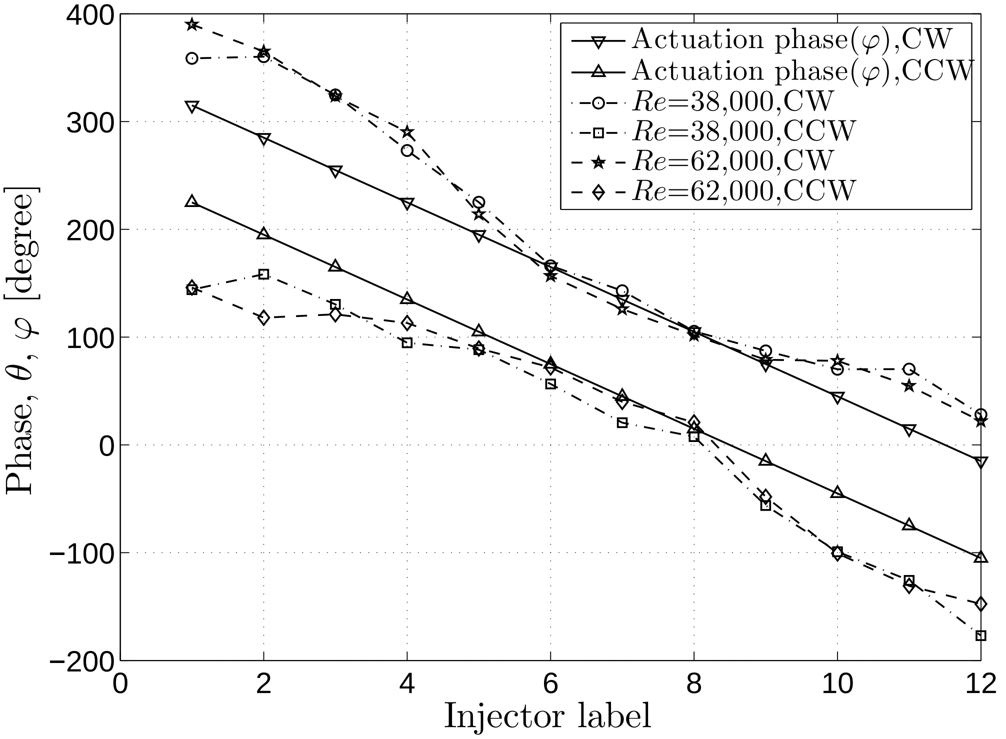

Figure 4.19: The phase obtained using S-PIV data in comparison with the phase of the injection line for *Re*=38,000 and *Re*=62,000 at CW and CCW actuation.

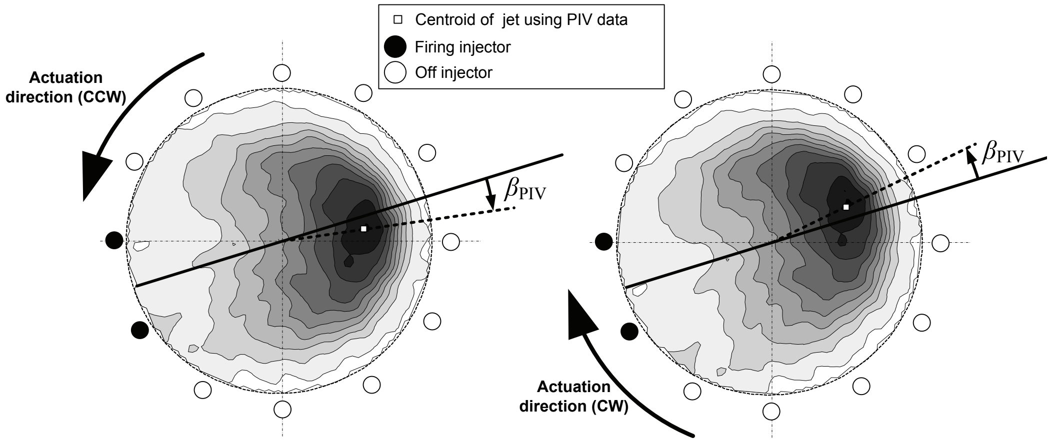

Figure 4.20: The schematic representation of the centroid phase obtained by S-PIV with respect to the injection line.

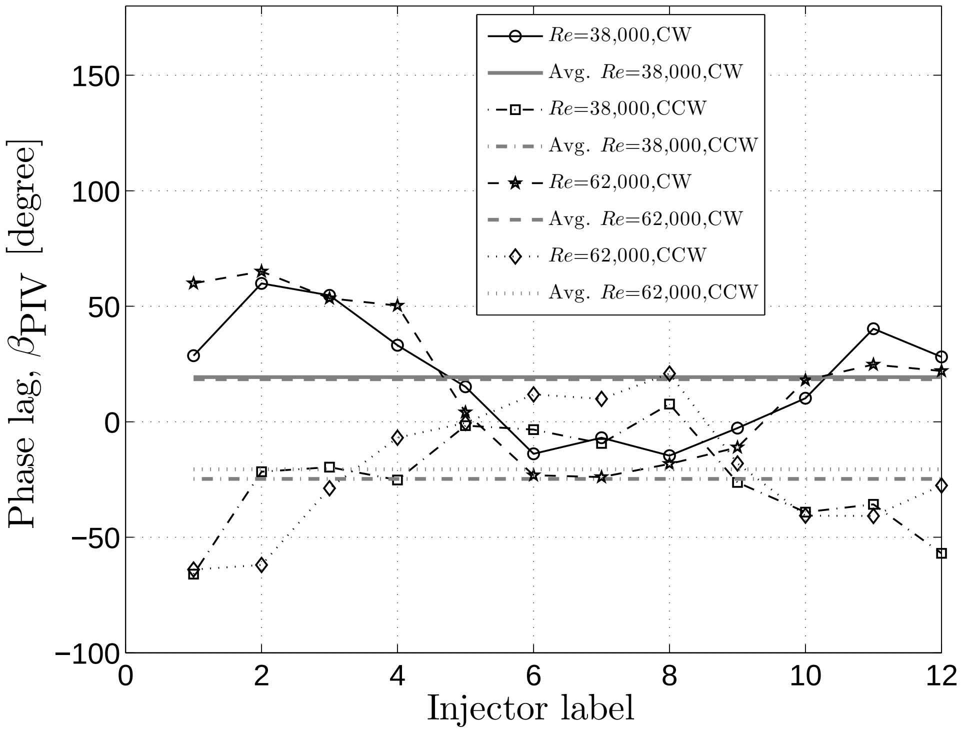

Figure 4.21: The lag, β_{PIV}, obtained using S-PIV data for *Re*=38,000 and *Re*=62,000 at CW and CCW actuation.

4.2 Pressure data analysis

This section describes the pressure data analysis collected simultaneously with S-PIV measurements. The direction analysis of these experiments are shown in Figure 4.22 for $Re = 38,000$ and Figure 4.23 for $Re = 62,000$ (the actuation timing is the same described in Figure 4.1). As expected from Chapter 3, the precession direction can be controlled in $Re = 38,000$ whereas $Re = 62,000$ shows chaotic behavior (for example, see the CCW case triggered with injector 2 in Figure 4.23).

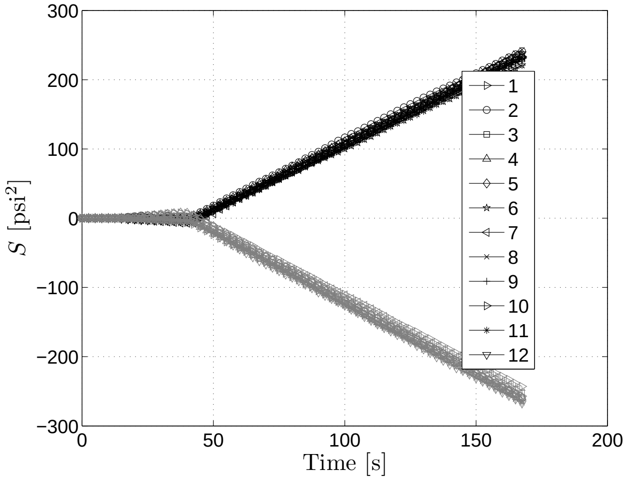

Figure 4.22: Direction analysis for the CW and CCW actuation of the flow with the chamber length ratio ($\frac{L}{D}$) of 2.5, Reynolds number of of 38,000 and without center body at the frequency (f) of 5 Hz.

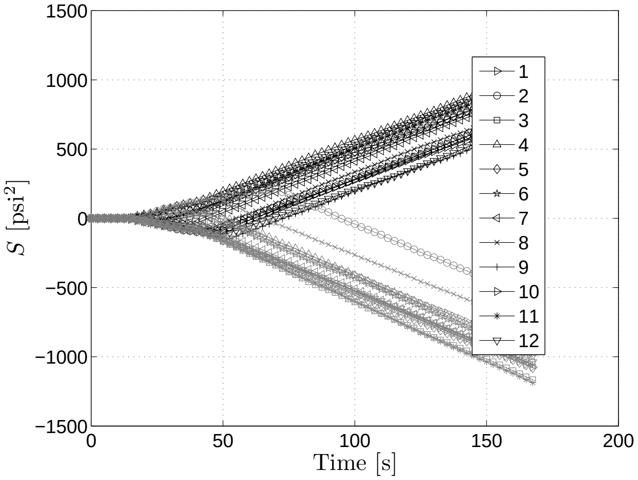

Figure 4.23: Direction analysis for the CW and CCW actuation of the flow with the chamber length ratio ($\frac{L}{D}$) of 2.5, Reynolds number of of 62,000 and without center body at the frequency (f) of 5 Hz.

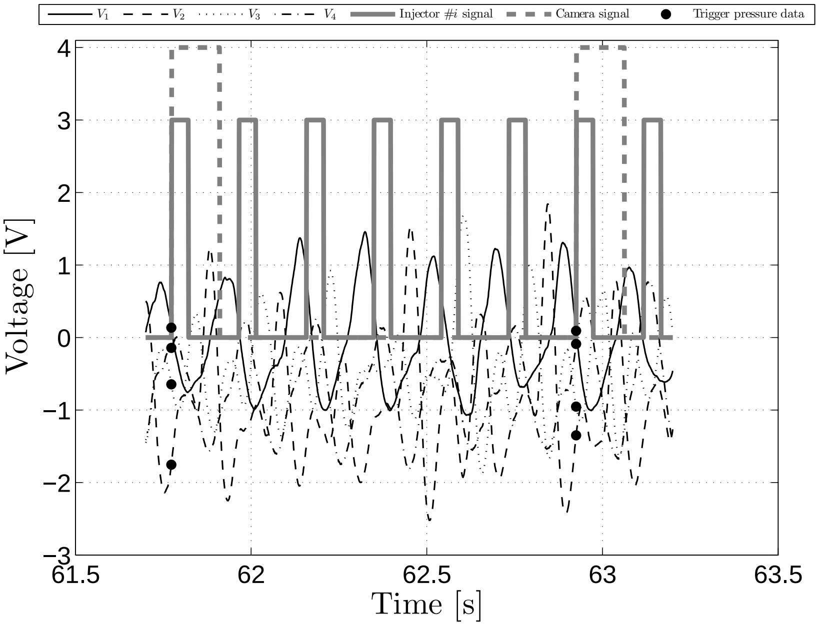

Figure 4.24: A sample of the voltage signal along with the signal of the injector # i and the camera signal; the beginning of the camera signal is used to sample the corresponding pressure data.

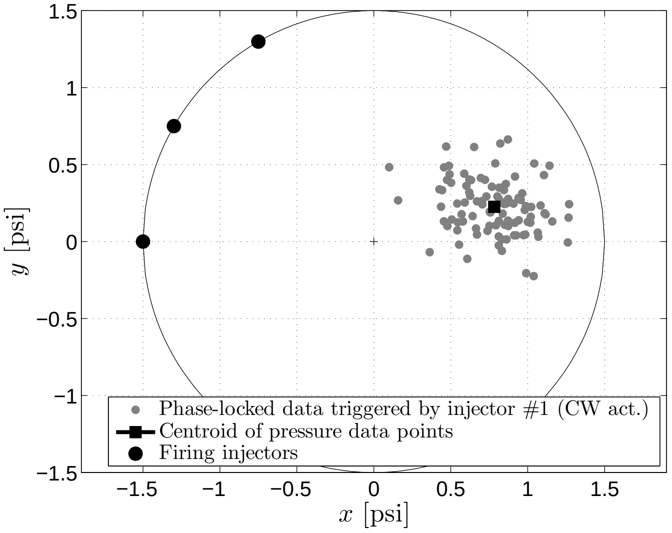

Figure 4.25: The phase plane representation of the triggered pressure data and the centroid point (shown by ■) corresponding to injectors 11 and 12 for $\frac{L}{D}$ of 2.5, without center body, Re=62,000 in the CW actuation with f=5 Hz.

In the previous section, the average phase and lag of the precessing jet centroid are obtained based on S-PIV measurement. A similar procedure is described for the pressure data where the trigger signal for the camera is used to sample pressure data corresponding to S-PIV images (see Figure 4.24). These pressure points are mapped into phase plane as shown in Figure 4.25 and their centroid is calculated by:

$$x_c = \frac{\sum_{i=0}^{n} x_i}{n} \quad , \quad y_c = \frac{\sum_{i=0}^{n} y_i}{n} \tag{4.1}$$

A two dimensional histogram of all triggered pressure data in phase-plane, shown in Figure 4.25, is calculated with a result for a case triggered by injector 1 shown in Figure 4.26. The probability of the precessing jet location is indicated by the color intensity.

Combining all twelve trigger points for each Reynolds number and actuation direction together results in Figure 4.27. Each color represents an experiment based on a different trigger state and same color is used to show corresponding jet position probabilities. While the different color regions for $Re = 38,000$, i.e. Figures 4.27(a) and 4.27(b), are almost separate regions, the colors in high Reynolds number of (i.e. Figures 4.27(c) and 4.27(d)) overlap each other. It can be concluded that actuation for low Reynolds number ($Re = 38,000$) is effective at manipulating the jet position whereas at the high Reynolds number ($Re = 62,000$), the flow control actuation is less effective.

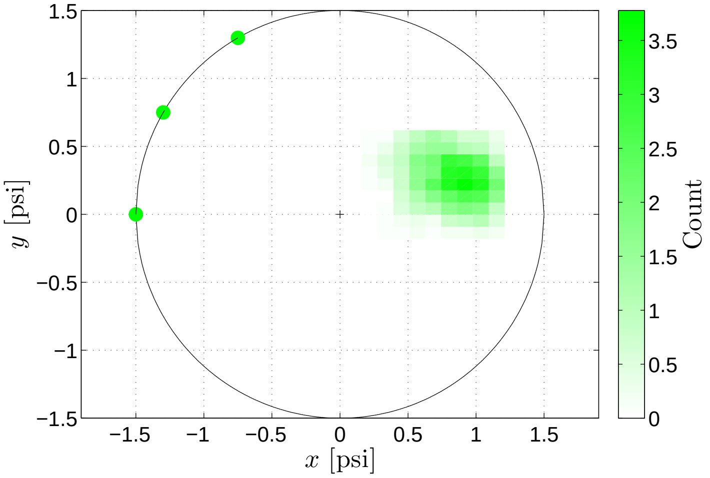

Figure 4.26: Two dimensional histogram representation of the phase plane of the triggered pressure data corresponding to injectors 11 and 12 for $\frac{L}{D}$ of 2.5, without center body, Re=62,000 in the CW actuation with f=5 Hz.

Comparing CW and CCW actuation at $Re = 62,000$ shows more overlap in the CCW than in the CW case which is another indicator that the CW direction is preferred for this flow. Using the centroid of the pressure data as defined in Equation 4.1 to define the jet location from the pressure signal, the phase and lag of this pressure centroid can be defined analogous to S-PIV data (see Figure 4.28). The phase and lag values obtained based on pressure data are shown in Figure 4.29 and 4.30, respectively. Both figures show similar trends compared to S-PIV measurement (see Figure 4.19 and 4.21). The average of lag values for pressure measurement is given in Table 4.3. To compare the ability of the pressure measurements to determine the location of the precessing jet, the difference between lag values obtained by S-PIV (i.e. β_{PIV}), and lag values from pressure measurement (i.e. β_{p}) is shown in Figure 4.31. A comparison of the difference of the phase lag between using S-PIV and pressure data, defined as $\Delta\beta = \beta_{\mathrm{PIV}} - \beta_p$, is listed in Table 4.4.

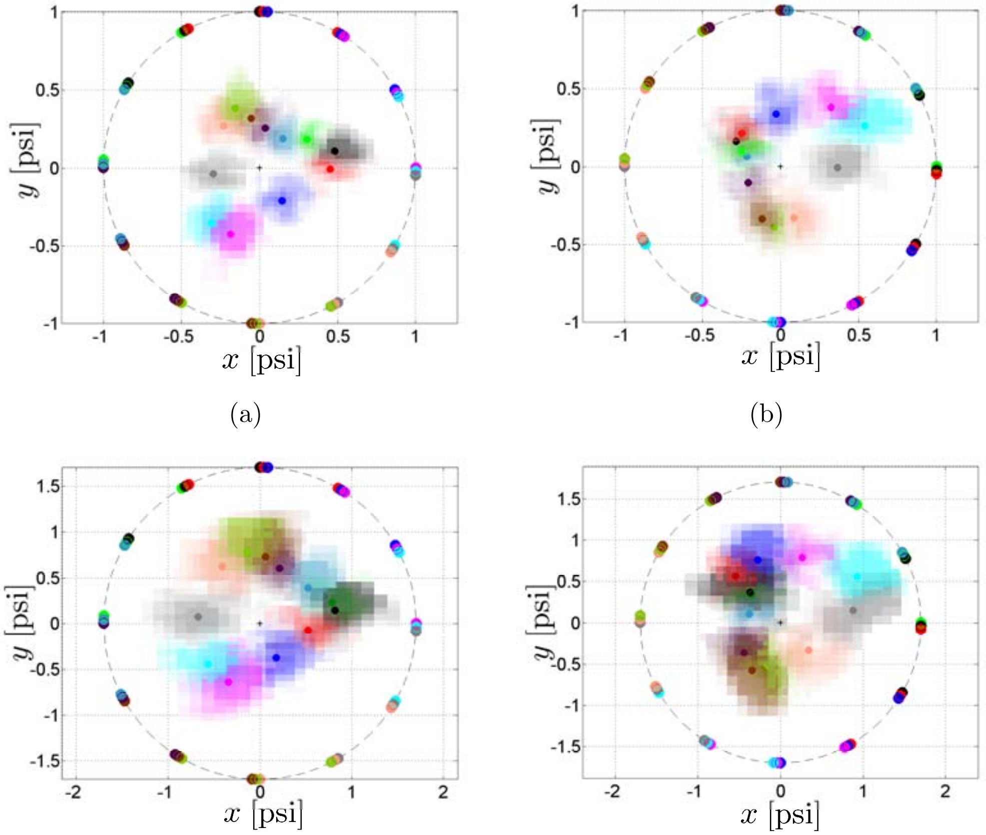

(a)

(b)

(c)

(d)

Figure 4.27: Two dimensional histogram representation of the phase plane of the triggered pressure data for all triggered injectors shown in different colors for $\frac{L}{D}$ =2.5, without center body and the actuation frequency (f) of 5 Hz at (a) *Re*=38,000 in CW actuation, (b) *Re*=38,000 in CCW actuation, (c) *Re*=62,000 in CW actuation and (d) *Re*=62,000 in CCW actuation.

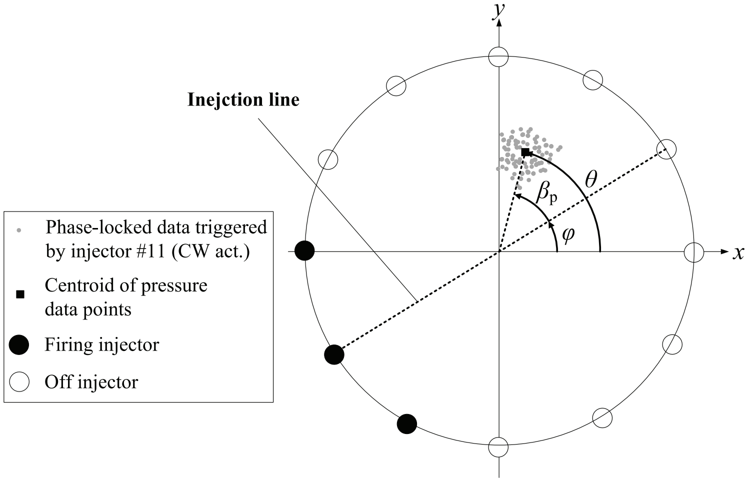

Figure 4.28: The definition of phase and lag between pressure data and the injection line.

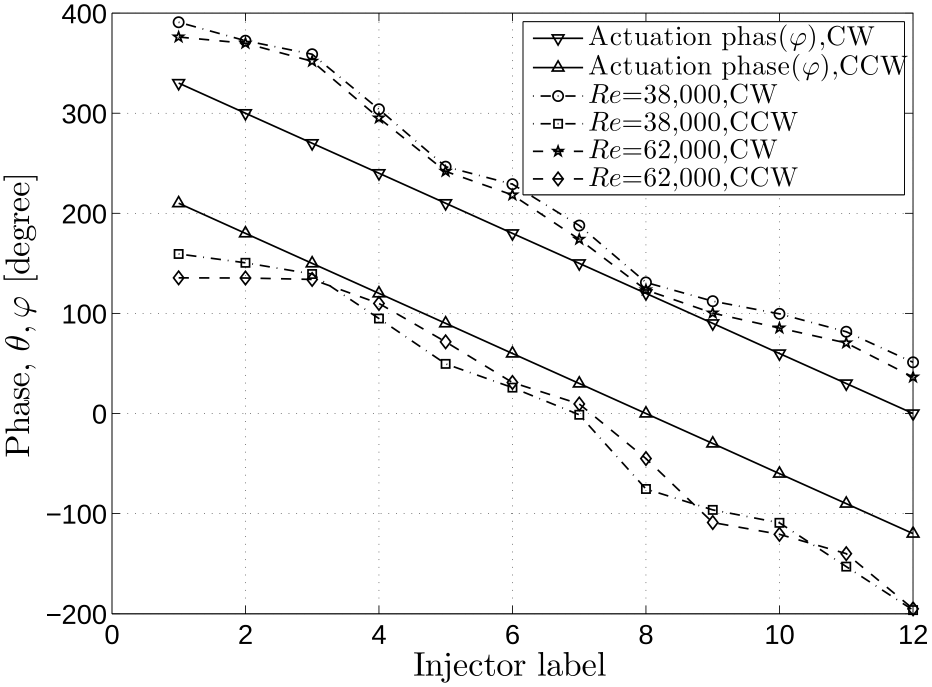

Figure 4.29: The phase obtained based on pressure data in comparison with the phase of injection line for *Re*=38,000 and *Re*=62,000 at CW and CCW actuation.

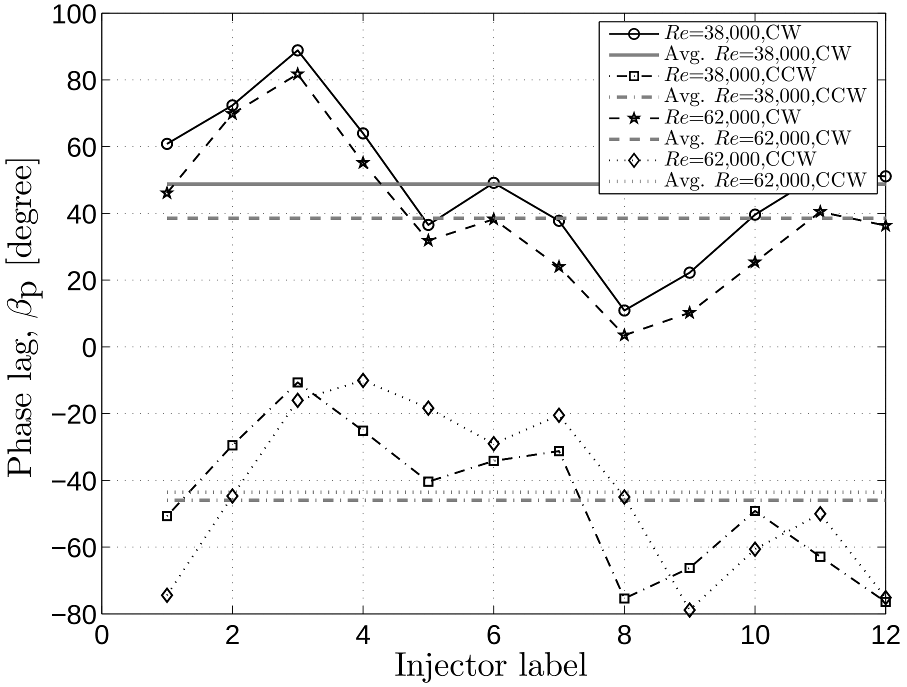

Figure 4.30: The lag, β_p, obtained based on pressure data for Re=38,000 and Re=62,000 at CW and CCW actuation.

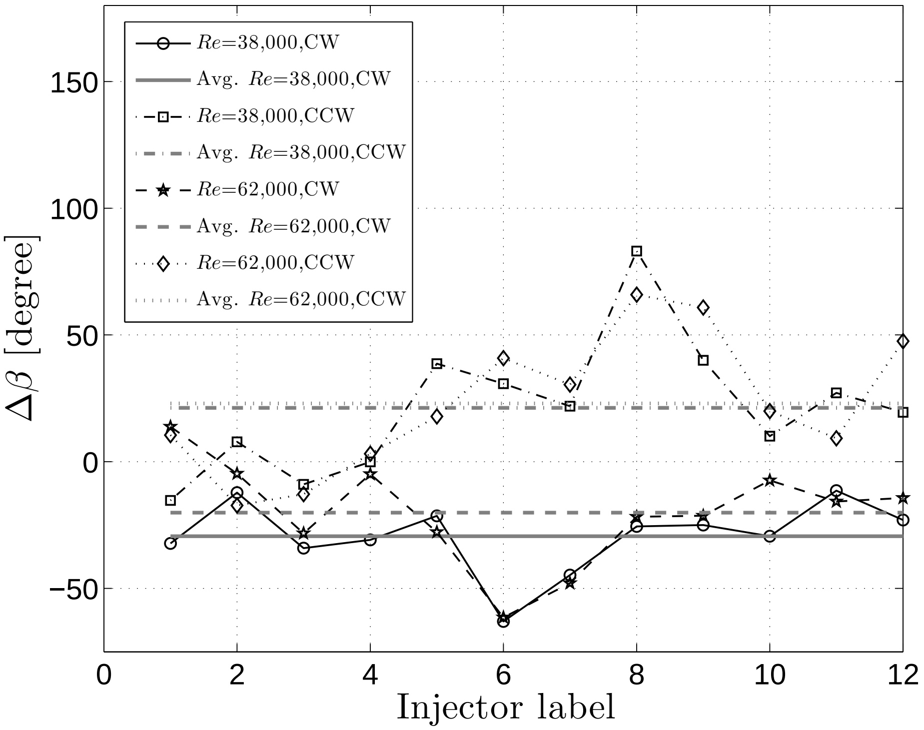

Figure 4.31: The lag difference ($\Delta\beta = \beta_{\mathrm{PIV}} - \beta_{\mathrm{p}}$) between pressure and S-PIV data for Re=38,000 and Re=62,000 at CW and CCW actuation.

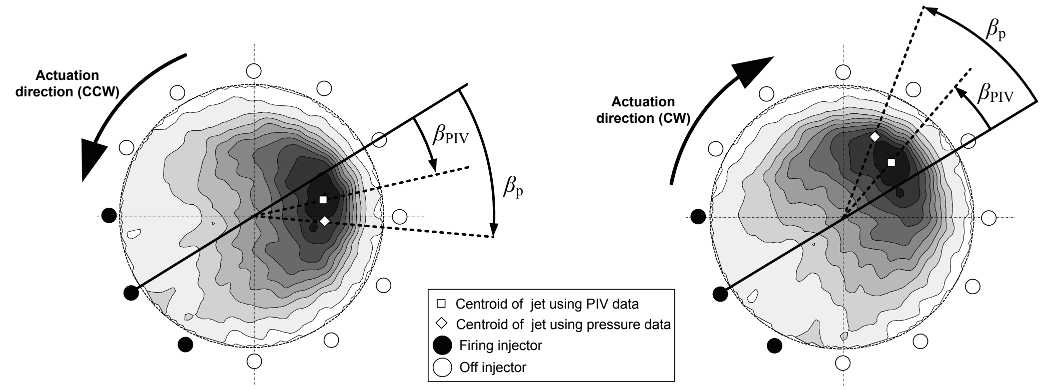

Figure 4.32: The schematic representation of the centroid phase obtained by S-PIV and pressure data with respect to the injection line.

Table 4.3: The lag, β_p, between the centroid phase and the injection line obtained using pressure data

Re	CW Actuation	CCW Actuation
38,000	49 ± 21	-46 ± 21
62,000	39 ± 23	-44 ± 25

Table 4.4: The lag difference between pressure data and S-PIV ($\Delta\beta = \beta_{\mathrm{PIV}} - \beta_{\mathrm{p}}$)

Re	CW Actuation	CCW Actuation
38,000	-30	21
62,000	-21	22

There is a difference of 20-30° between S-PIV and pressure data which is shown in schematic view in Figure 4.32 indicating the pressure data estimation delay compared to the S-PIV estimate.

One possible cause for the difference between the S-PIV and pressure phase lags is that the laser sheet measurement is 4 mm downstream of the chamber exit where the pressure sensor are located. This hypothesis can be further investigated in future through capturing 3D evolution of the precessing jet as it exits the chamber using tomographic PIV.

The pressure data analysis introduced in Chapter 3 for finding the jet location is validated using phase-locked S-PIV technique. The results obtained by comparing S-PIV and pressure data are encouraging as they indicate that pressure data can be used as a measure of the jet location in future feedback control schemes. S-PIV images also reveal that the general shape of the actuated precessing jet evolves from a kidney-bean shape (no actuation) to a twisted teardrop shape during the actuation.

Chapter 5

Conclusions

A precessing jet, subject to both passive and active control is experimentally investigated. The passive control includes changing the chamber length and having a center body present or absent. The active control consists of twelve micro-jets mounted around the nozzle inlet. The flow field is monitored using pressure signals acquired at the chamber exit and by S-PIV just downstream of the chamber exit. Due to the chaotic nature of the precessing jet at some flow conditions, power spectrum and cross correlation methods did not extract useful information of the flow behavior. A phase plane, made up of a subtraction of vertical pressure signals as y axis and a subtraction of horizontal signals for x axis, is developed and found useful to extract information about the precession. In particular, the precession direction, radius and phase of jet high velocity region are analyzed in the phase plane.

Different flow control experiments have been conducted to gain insight into the behavior of flow before and with actuation. The results reveal the experimental apparatus has a preferred precession direction which is CW. At low Reynolds number ($Re = 38,000$), the actuation is able to change the flow direction either CW or CCW. At high Reynolds number ($Re = 62,000$), the flow direction appears random and cannot be controlled. The following conclusions are drawn based on the phase investigation for all chamber lengths, Reynolds number, actuation frequency and direction in the precessing jet with and without center body:

- Using the same actuation frequency for the same flow conditions, the precessing jet can be stabilized in preferred direction (CW here) more easily than in the reverse direction (CCW).
- The effectiveness of actuation is at the highest for the shortest chamber length ratio ($\frac{L}{D} = 2$) and decreases for longer chamber lengths.
- By increasing Reynolds number, the ability to force the jet to precess at the actuation frequency decreases.

- There is a range of actuation Strouhal number where the precessing jet flow follows the actuation with lower variation. This range matches with the natural Strouhal of the precession $(0.002 - 0.006)$.

Phase-locked S-PIV measurement is used to verify that the pressure phase plane corresponds to the jet position determined by S-PIV. The results show that the center of the precessing jet estimated using the pressure sensors at the chamber exit lags about 20-30° behind the jet center determined by the S-PIV measurement. This means that the pressure data can be used as an estimate for the jet position in future feedback control strategies.

Reference List

[1] J. M. Ottino. *The Kinematics of mixing, stretching, chaos, and transport.* Cambridge University Press, 1997.

[2] O.M. Aamo and M. Krstic. *Flow control by feedback, stabilization and mixing.* Springer, 2003.

[3] M. Gad el Hak. *Flow control, passive, active and reactive flow management.* Cambridge University Press, 2006.

[4] S.I. Green, editor. *Fluid Vortices.* Academic Publishers, 1995.

[5] G.J. Nathan, J. Mi, Z.T. Alwahabi, G.J.R. Newbold, and D.S. Nobes. Impacts of a jet's exit flow pattern on mixing and combustion performance. *Progress in Energy and Combustion Science*, 32(5-6):496–538, 2006.

[6] C. Manias, A. Balendra, and D. Retallack. New combustion technology for lime production. *World Cement*, 27(12):34–39, December 1996.

[7] J. Mi, R.E. Luxton, and G.J. Nathan. Oscillating jets, US 6685102 B1, 11 2004.

[8] J. Mi, G.J. Nathan, and R.E. Luxton. Mixing characteristics of a flapping jet from a self-exciting nozzle. *Flow, Turbulence and Combustion*, 67(1):1–23, 2002.

[9] G.J. Nathan, S.J. Hill, and R.E. Luxton. An axisymmetric nozzle to generate jet precession. *Journal of Fluid Mechanics*, 370:347–380, 1998.

[10] C.Y. Wong, P.V. Lanspeary, G.J. Nathan, R.M. Kelso, and T. O'Doherty. Phase-averaged velocity in a fluidic precessing jet nozzle and in its near external field. *Experimental Thermal and Fluid Science*, 27:515–524, May 2003.

[11] G.J. Nathan and R.E. Luxton. Mixing enhancement by a self-exciting, asymmetric precessing flow-field. *J.A. Reizes, Editor, Transport Phenomena in Heat and Mass Transfer*, pages 1297–1307, 1992.

[12] C.Y. Wong, G.J. Nathan, and T. O'Doherty. The effect of initial conditions on the exit flow from a fluidic precessing jet nozzle. *Experiments in Fluids*, 36:70 – 81, 2004.

[13] G.J. Nathan. *The enhanced mixing burner*. PhD thesis, University of Adelaide, 1988.

[14] G.J.R. Newbold. *Mixing and combustion in precessing jet flows*. PhD thesis, University of Adelaide, 1998.

[15] A. Madej. The experimental investigation of the effect of chamber length on jet precession. Master's thesis, University of Alberta, 2010.

[16] S.J. Hill, G.J. Nathan, and R.E. Luxton. Precession in axisymmetric confined jets. In *12th Australasian Fluid Mechanics Conference*, 1995.

[17] R.M. Kelso. A mechanism for jet precession in axisymmetric sudden expansions. In *14th Australasian Fluid Mechanics Conference*, 2001.

[18] R.E. Luxton and G.J. Nathan. Controlling the motion of a fluid jet , US 5060867, 10 1991.

[19] B. Guo, T.A.G. Langrish, and D.F. Fletcher. Numerical simulation of unsteady turbulent flow in axisymmetric sudden expansions. *J. Fluids Eng.*, 123:574–587, September 2001.

[20] J. Mi and G.J. Nathan. Self-excited jet-precession strouhal number and its influence on downstream mixing field. *Journal of Fluids and Structures*, 19:851–862, July 2004.

[21] G.J. Nathan and R.E. Luxton. Entrainment and combustion characteristics of an axi-symmetric, self exciting, enhanced mixing nozzle. In *ASME/JSME Thermal Engineering Joint Conference*, pages 145–152, 1991.

[22] C.G. Manias and G.J. Nathan. Low NO$_x$ clinker production. *World Cement*, 25(5):54–56, May 1994.

[23] C.Y. Wong, G.J. Nathan, and R.M. Kelso. The naturally oscillating flow emerging from a fluidic precessing jet nozzle. *Journal of Fluid Mechanics*, 606:153–188, 2008.

[24] G. Schneider, J. Hooper, A. Musgrove, G.J. Nathan, and R.E. Luxton. Velocity and Reynolds stresses in a precessing jet flow. *Experiments in Fluids*, 22:489–495, 1997.

[25] J. Mi, R.E. Luxton, and G.J. Nathan. The mean flow field of a precessing jet. In *13th Australasian Fluid Mechanics Conference*, 1998.

[26] C.H. Birzer, P.A.M. Kalt, and G.J. Nathan. The influences of jet precession on near field particle distributions. *International Journal of Multiphase Flow*, 35(3):288–96, March 2009.

[27] G. England, P.A.M. Kalt, G.J. Nathan, and R.M. Kelso. The effect of density ratio on the near field of a naturally occurring oscillating jet. *Experiments in Fluids*, 48(1):69–80, 2010.

[28] J. Mi, G.J. Nathan, and C.Y. Wong. The influence of inlet flow condition on the frequency of self-excited jet precession. *Journal of Fluids and Structures*, 22:129–133, January 2006.

[29] R. King, V. Mehrmann, and W. Nitsche. Active flow controla mathematical challenge. In Martin Grtschel, Klaus Lucas, and Volker Mehrmann, editors, *Production Factor Mathematics*, pages 73–80. Springer Berlin Heidelberg, 2010.

[30] J. Mi and G.J. Nathan. Statistical properties of turbulent free jets issuing from nine differently-shaped nozzles. *Flow, Turbulence and Combustion*, pages 1–24, 2009. Article in Press.

[31] P. Behrouzi, T. Feng, and J.J. McGuirk. Active flow control of jet mixing using steady and pulsed fluid tabs. *Proceedings of the Institution of Mechanical Engineers. Part I: Journal of Systems and Control Engineering*, 222(5):381–392, 2008.

[32] C.R. Koch. *Closed loop control of a round jet/diffuser in transitory stall.* PhD thesis, Stanford University, 1991.

[33] A. Sinha, K. Kim, J-H. Kim, A. Serrani, and M. Samimy. Towards feedback control of highspeed and highreynolds number jets. In *4th AIAA Flow Control Conference*, 2008.

[34] F.K. Lu, R.D. Joslin, and D.N. Miller, editors. *Fundamental and applications of modern flow control Volume 231, Progress in Astronautics and Aeronautics.* AIAA, Inc., 2009.

[35] C.H. Sieverding and C. Warsop, editors. *MEMS and active flow control.* von Karman Institute for Fluid Dynamics, 2002.

[36] M. Gad-el Hak. Fluid mechanics of microdevices-the Freeman scholar lecture. *Journal of Fluids Engineering, Transactions of the ASME*, 121(1):5–33, 1999.

[37] Y. Huang and V. Yang. Dynamics and stability of lean-premixed swirl-stabilized combustion. *Progress in Energy and Combustion Science*, 35(4):293 – 364, 2009.

[38] M. Gad el Hak. *Flow control, fundamentals and practices.* Springer, 1998.

[39] M. Raffel, C.E. Willert, S.T. Wereley, and J. Kompenhans. *Particle Image Velocimetry, a practical guide.* Springer, 2007.

[40] C.W.H. Van Doorne and J. Westerweel. Measurement of laminar, transitional and turbulent pipe flow using Stereoscopic-PIV. *Experiments in Fluids*, 42(2):259–279, 2007.

[41] B. Wieneke. Stereo-piv using self-calibration on particle images. *Experiments in Fluids*, 39(2):267–280, 2005.

[42] F.C. Moon. *Chaotic and fractal dynamics, an introduction for applied scientists and engineers.* John Wiley & Sons, Inc., 1992.

[43] K.W. Ng. Chaotic motion in confined jet flows. In *ASME, AMD-Vol. 151, PVP-Vol. 247 Symposium on flow-induced vibration and noise*, 1992.

[44] G. Broze and F. Hussain. Nonlinear dynamics of forced transitional jets: periodic and chaotic attractors. *Journal of Fluid Mechanics*, 263:93–132, 1994.

[45] G. Broze and F. Hussain. Transitions to chaos in a forced jet: Intermittency, tangent bifurcations and hysteresis. *Journal of Fluid Mechanics*, 311:37–71, 1996.

Appendices

Appendix A

Drawings

Table A.1: SolidWorks files

Filename	**Part description**
Assembly.SLDASM	This is the frame developed to mount and seal fuel injectors on them (similar to fuel rail in engine)
Frame.SLDPRT	Side part of the water rail
Seat.SLDPRT	Bottom part of the water rail where fuel injectors sit
Fuel Rail.SLDPRT	Top part of water rail
nozzle.SLDPRT	This part contains main jet with smooth contraction inlet along with micro-channels for injections
lip.SLDPRT	This part is mounted at the end of chamber and has twelve holes for pressure probes, some holes can be blocked if needed
cb.SLDPRT	It is a lip with center body, RP machine
cavity.SLDPRT	Using mentioned lengths of cavities give chamber length of 2,2.5,2.75,3,3.5 for with and without center body case

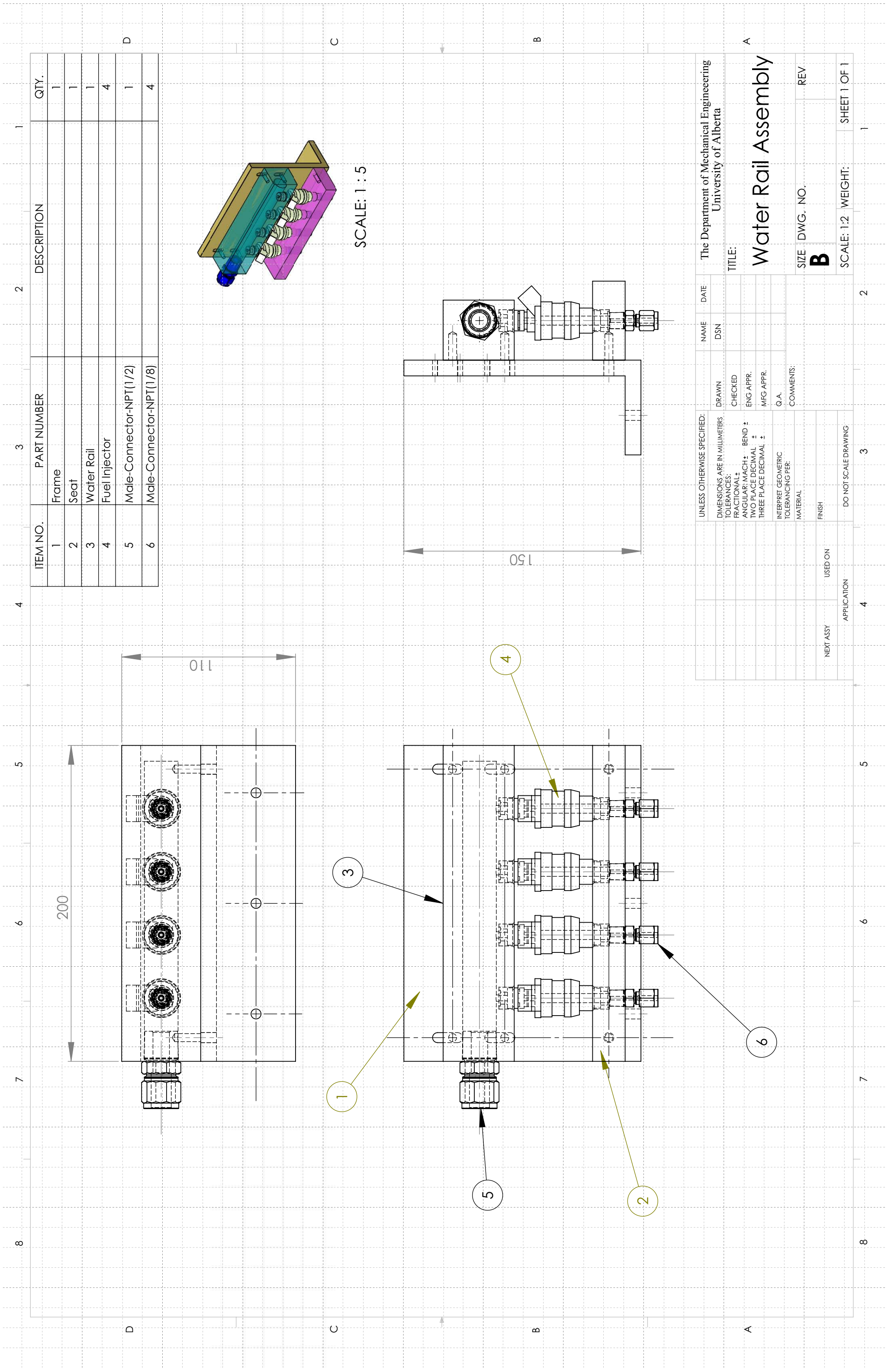

ITEM NO.	PART NUMBER	DESCRIPTION	QTY.
1	Frame		1
2	Seat		1
3	Water Rail		1
4	Fuel Injector		4
5	Male-Connector-NPT(1/2)		1
6	Male-Connector-NPT(1/8)		4

The Department of Mechanical Engineering
University of Alberta

TITLE:
Water Rail Assembly

SIZE B DWG. NO. REV

SCALE: 1:2 WEIGHT: SHEET 1 OF 1

Figure A.1: Drawing, Water rail assembly for injectors feeding.

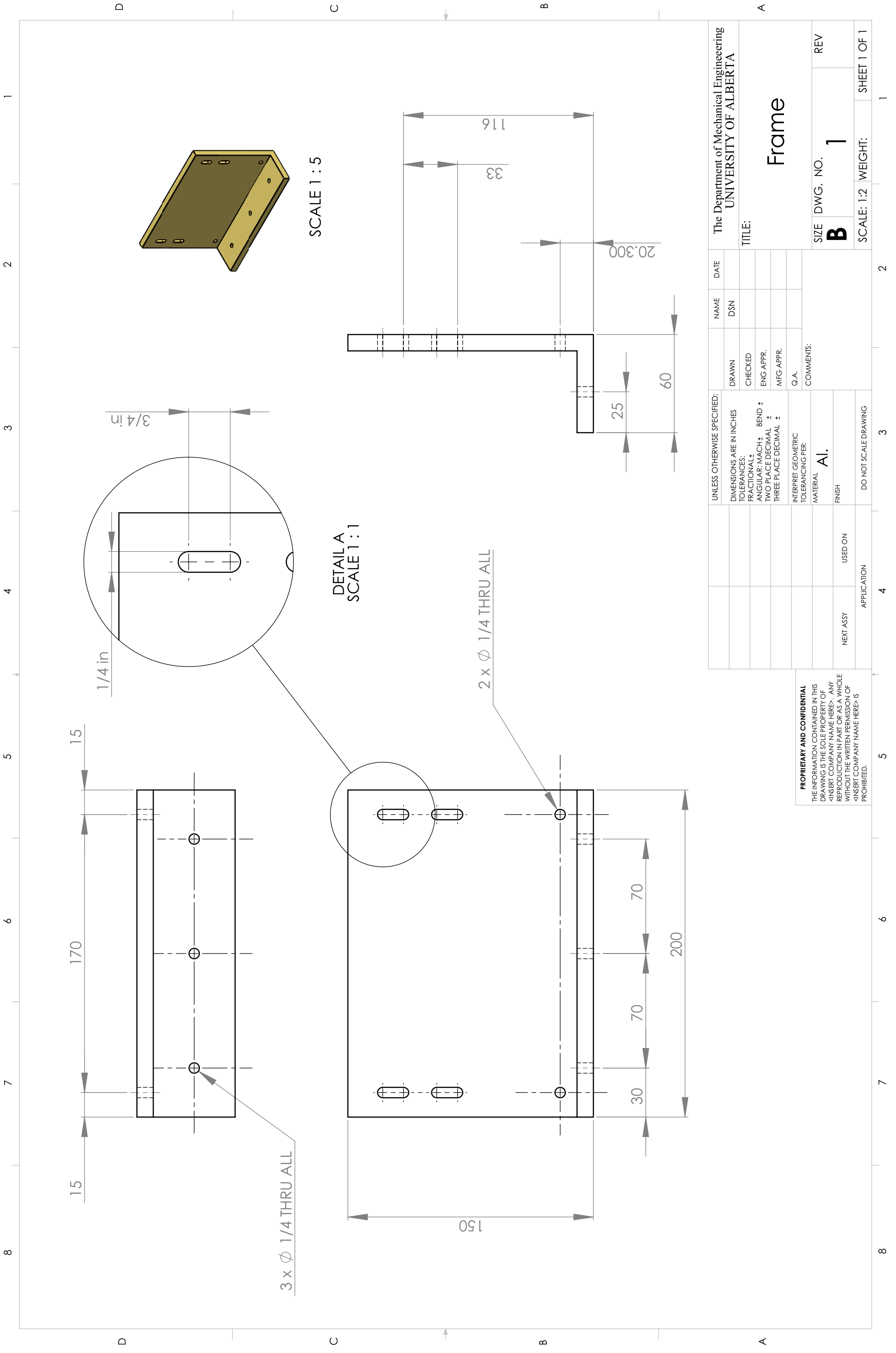

Figure A.2: Drawing, Water rail frame.

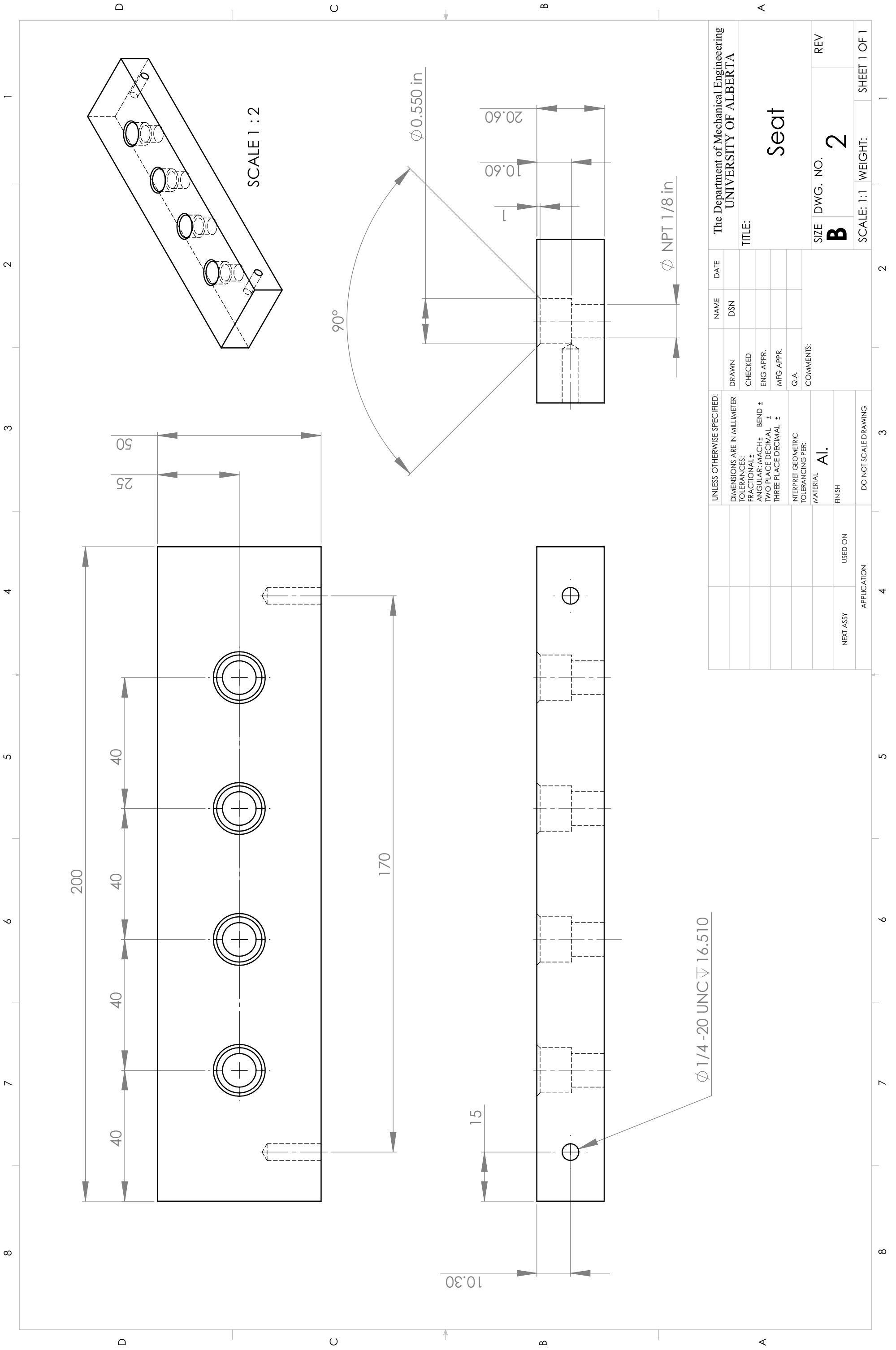

Figure A.3: Drawing, Water rail seat.

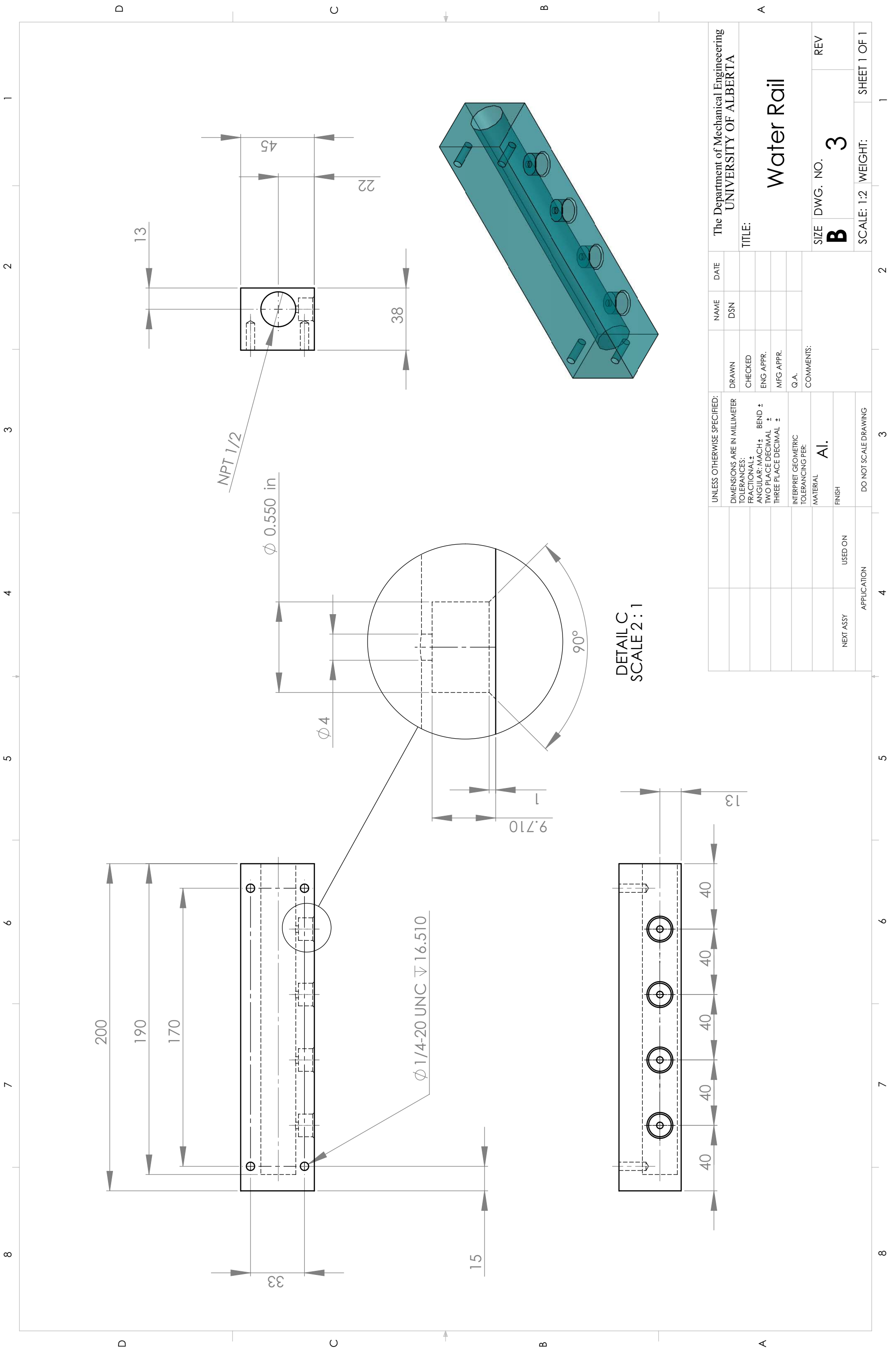

Figure A.4: Drawing, Water rail (top part).

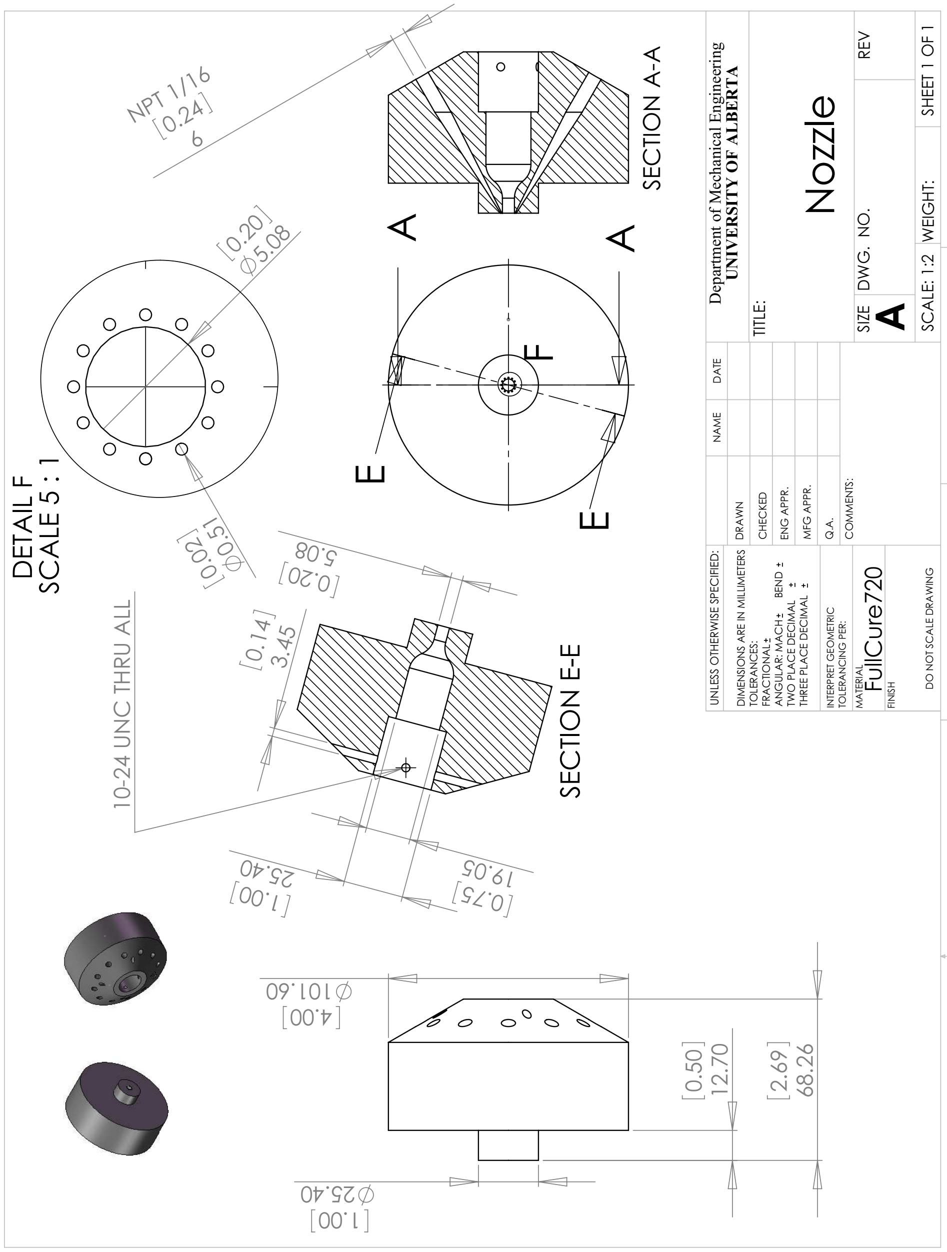

Figure A.5: Drawing, Nozzle.

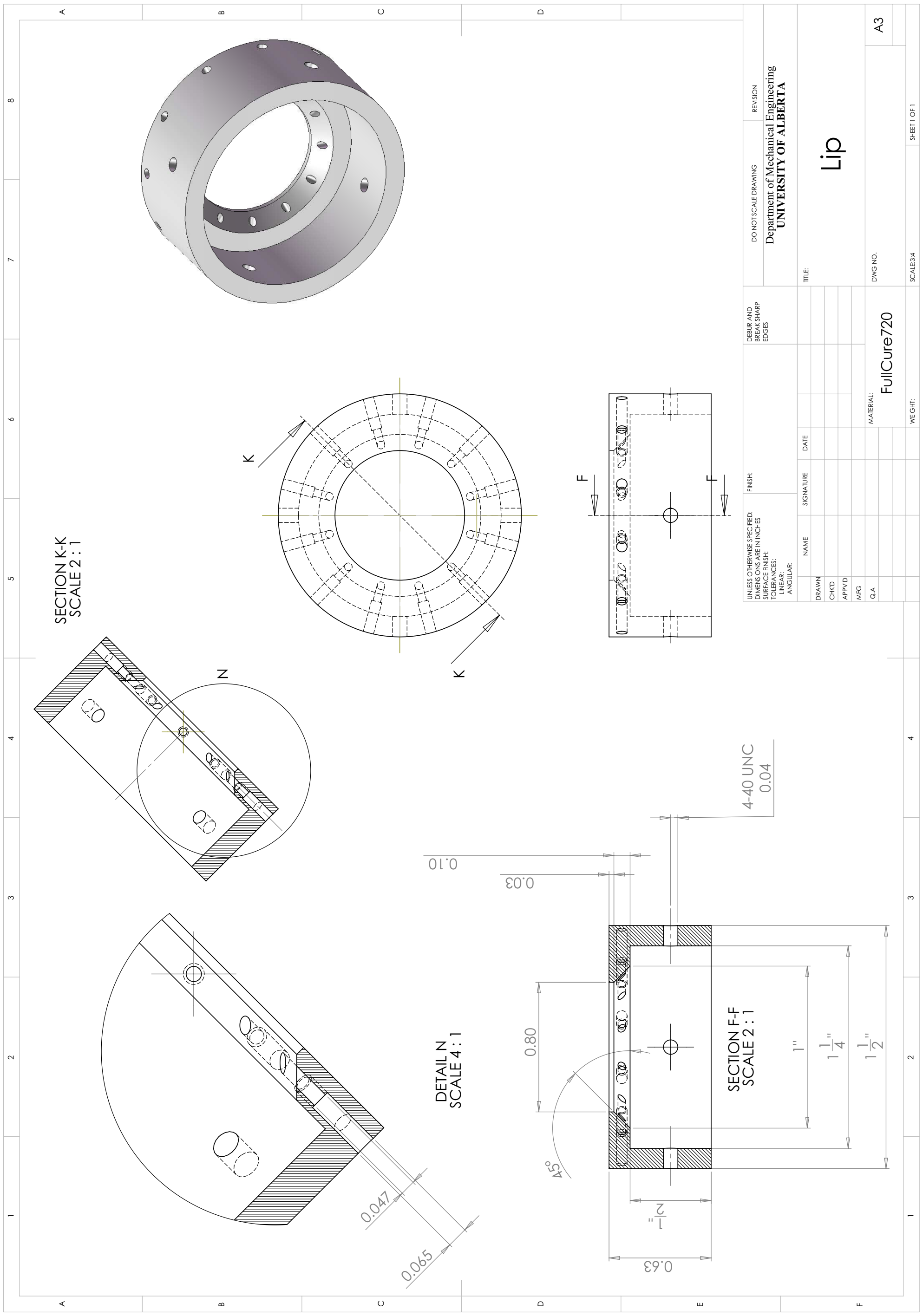

Figure A.6: Drawing, Lip.

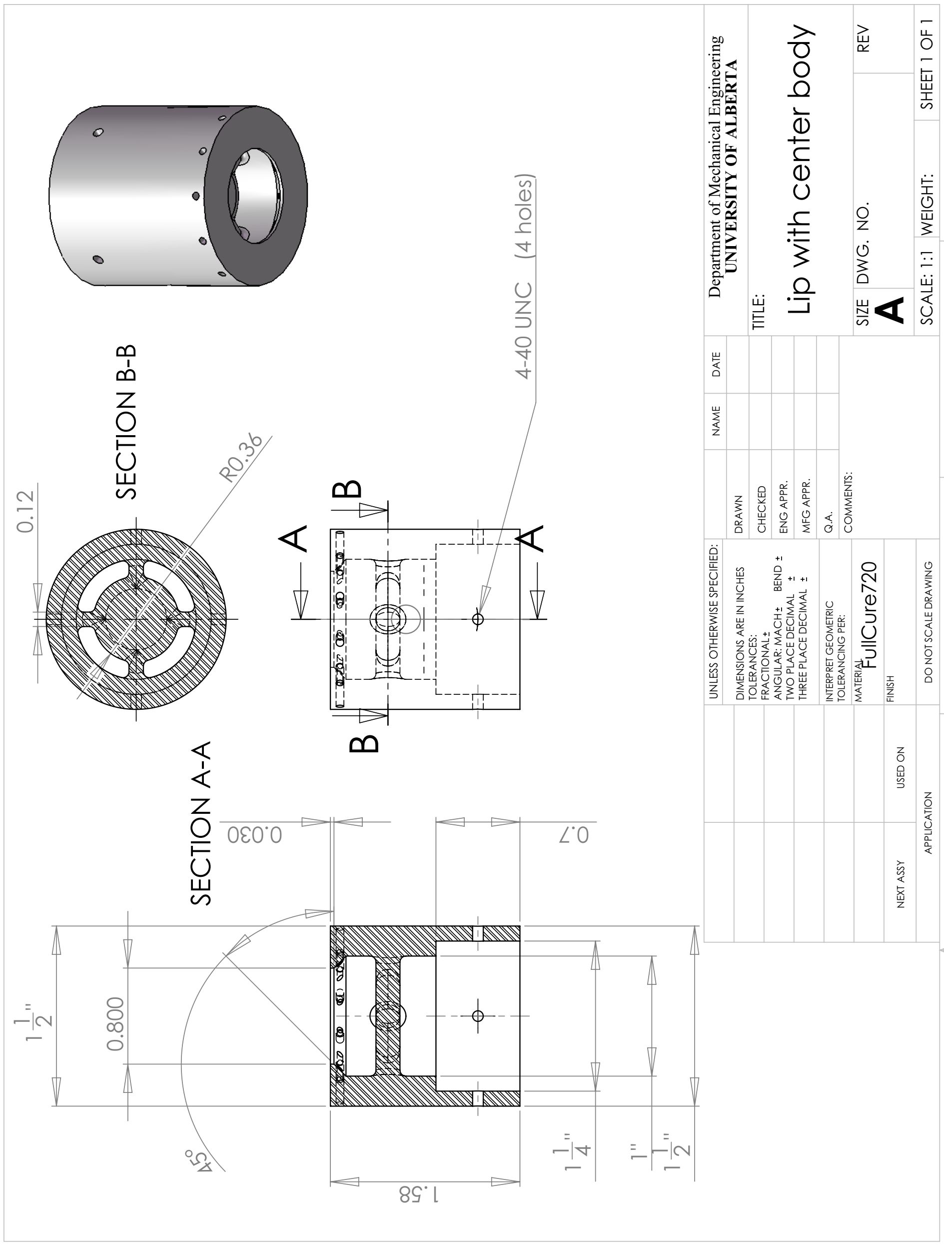

Figure A.7: Drawing, Lip with center body.

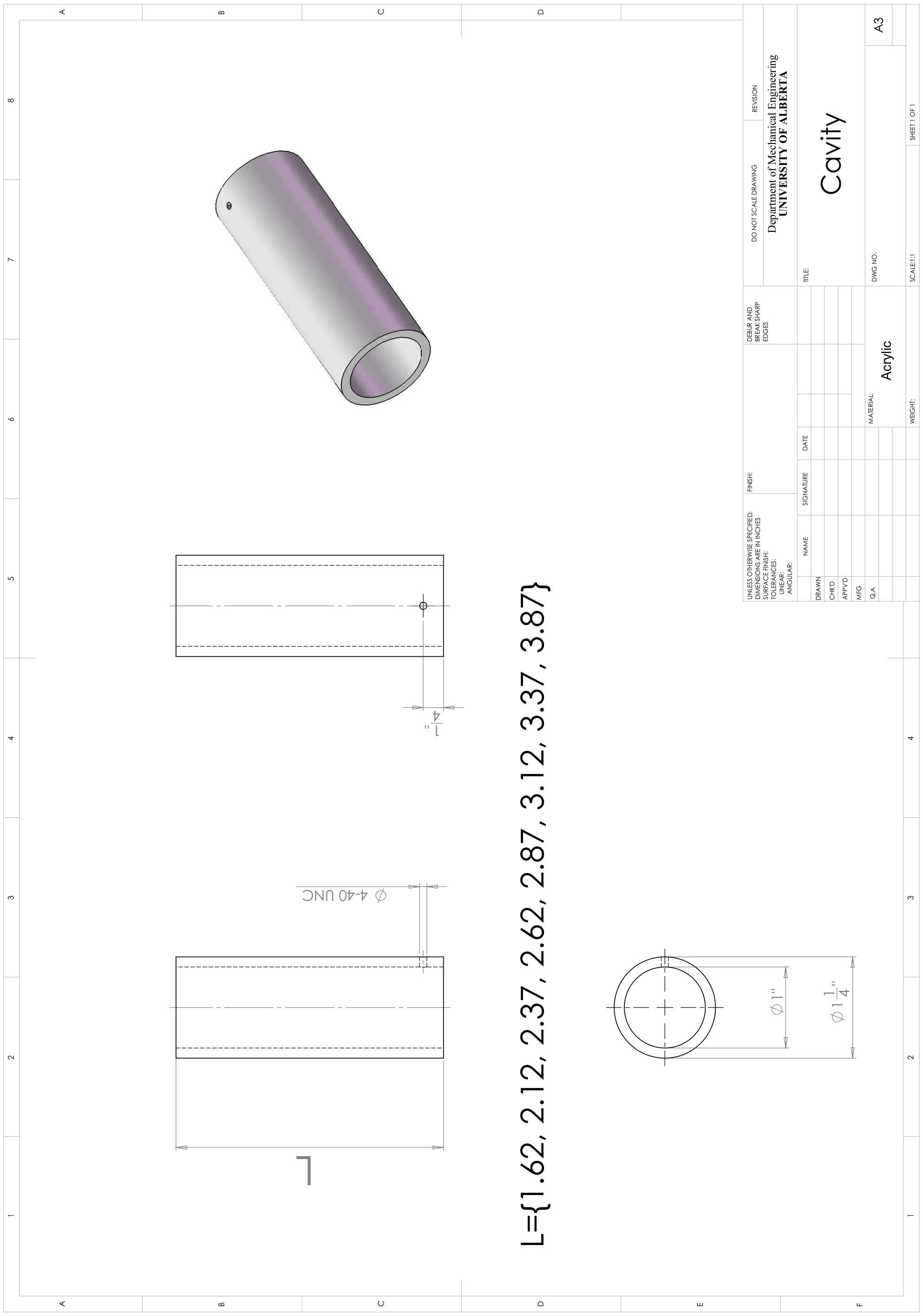

Figure A.8: Drawing, Cavity.

Appendix B

CVI, LabWindows code

Table B.1: LabWindows code

Filename	**code description**
$Acq - ExtClk\_dbg.exe$	use only to run the code
$Acq - ExtClk\_dbg.prj$	use to edit the LabWindows code

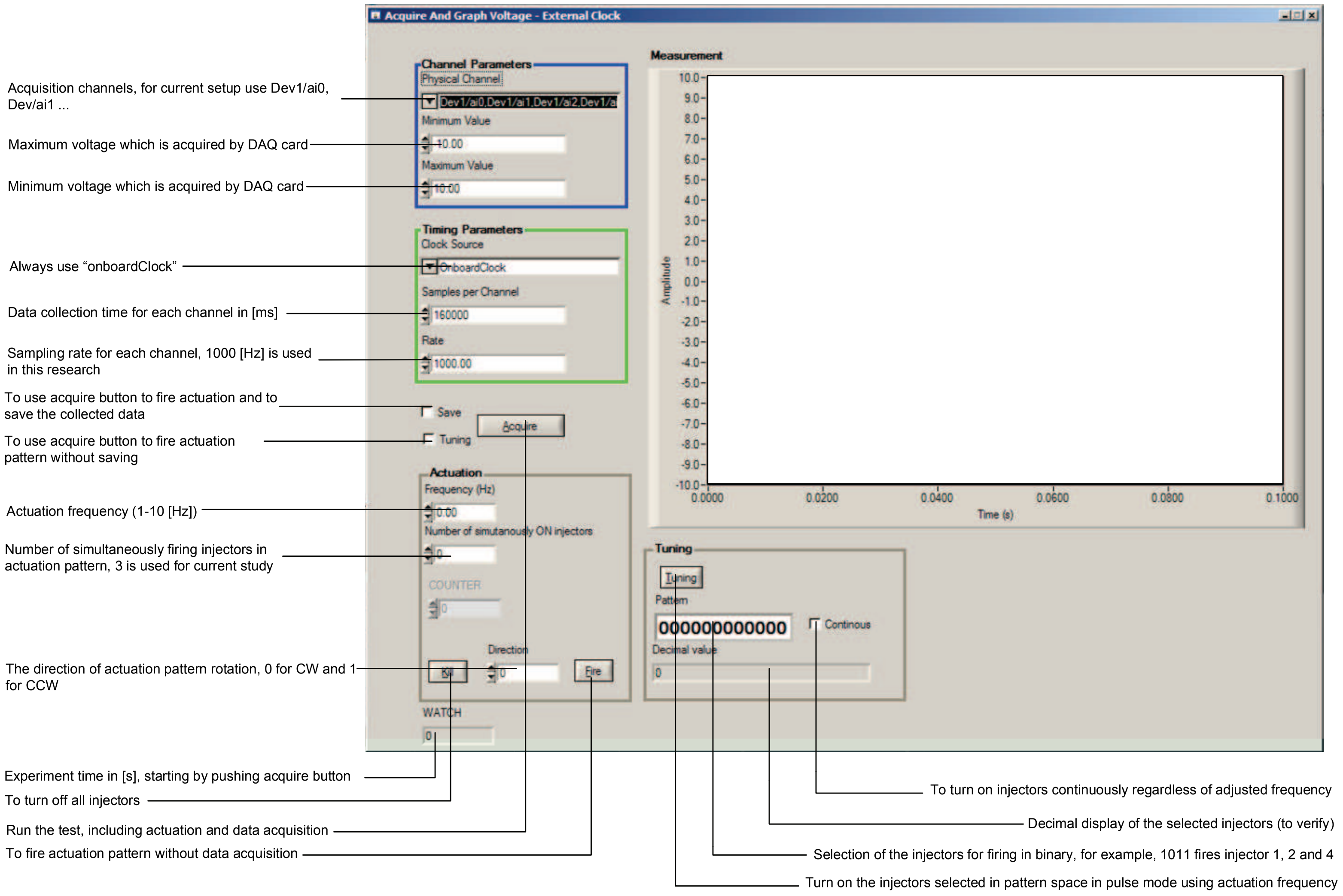

Physical Channel: Dev1/ai0,Dev1/ai1,Dev1/ai2,Dev1/a

Minimum Value: -10.00

Maximum Value: 10.00

Clock Source: OnboardClock

Samples per Channel: 160000

Rate: 1000.00

☐ Save

☐ Tuning

Frequency (Hz): 0.00

Number of simutanously ON injectors: 0

COUNTER: 0

Direction: 0

WATCH: 0

Pattern: 000000000000

☐ Continous

Decimal value: 0

Acquisition channels, for current setup use Dev1/ai0, Dev/ai1 ...

Maximum voltage which is acquired by DAQ card

Minimum voltage which is acquired by DAQ card

Always use “onboardClock”

Data collection time for each channel in [ms]

Sampling rate for each channel, 1000 [Hz] is used in this research

To use acquire button to fire actuation and to save the collected data

To use acquire button to fire actuation pattern without saving

Actuation frequency (1-10 [Hz])

Number of simultaneously firing injectors in actuation pattern, 3 is used for current study

The direction of actuation pattern rotation, 0 for CW and 1 for CCW

Experiment time in [s], starting by pushing acquire button

To turn off all injectors

Run the test, including actuation and data acquisition

To fire actuation pattern without data acquisition

To turn on injectors continuously regardless of adjusted frequency

Decimal display of the selected injectors (to verify)

Selection of the injectors for firing in binary, for example, 1011 fires injector 1, 2 and 4

Turn on the injectors selected in pattern space in pulse mode using actuation frequency

Figure B.1: CVI Graphical User Interface.

Appendix C

MATLAB code

Table C.1: MATLAB code (Pressure data set, Chapter 3)

Filename	**input**	**output**	**Description**
$p\_clb.m$	v, sensor label	p	Converting voltage into pressure data for one sensor
$ps\_clb.m$	v, number of channels	p	Running $p\_clb.m$ for all sensors and adding trigger signal
$convert.m$	filename, number of channels	p^{pd}	Running $ps\_clb.m$, subtracting hydrodynamic pressure and low path filtering (100 Hz)
$f-run.m$	-	print	Finding fft spectra and maximum power for all data sets
$c-run.m$	-	print	Plotting pressure signals inside a window and cross correlation results for different window sizes
$const.m$	filename, number of channels	x and y	Constructing phase plane
$farea$	x and y	S	Finding the direction of precession over time
lag	-	*picked* structure	Includes phase, phase difference with injection line and θ_{STD} of trigger pressure
$pdoc$	-	print	An example of pressure signal and the phase of trigger pressure
$spln$	-	print	Plotting direction analysis for different cases such as variation of Reynolds number
$splnstudy$	-	print	Plotting the influence of chamber length ratio on phase plane radius and direction analysis for all test points
P_lag	-	print	Finding trigger pressure data, phase and their lag with respect to the injection line (for S-PIV data set)
P_STD	-	print	Finding trigger pressure data and standard deviation of their phase (for S-PIV data set)

Table C.2: MATLAB code (PIV data set, Chapter 4)

Filename	**input**	**output**	**Description**
pressuredoc	-	print	2D histogram of trigger pressure data
load_PJ	filename	a structure including coordinates and velocities	Loading PIV raw data
$n \times nsmooth$	*load_P* structure, smoothness degree	smoothed structure	Smoothing velocity vector field
radar	coordinates of *load_P* structure, velocity vector field, chamber origin	centroid coordinates	Finding the precessing jet centroid
$rotate_struct$	*load_P* structure,chamber origin, rotation angle	rotated structure	Rotating a structure
lag_PIV	-	print	Finding PIV trigger data phase and lag and the standard deviation
PIV_plot	-	print	Plotting PIV velocity vector field, out of plane contour, and conditional averaging
PIV_lag	-	print	Plotting all PIV trigger data phase and lag together

Appendix D

Cross Correlation

Following the discussion about cross correlation in Chapter 3, two problems about peak selection in cross correlation for the precessing jet pressure signals are introduced here. Deviation of precession may result in a jump in the cross correlation. There are two main deficiencies of the cross correlation method to analyze the precessing jet flow. First, to get the correct precession frequency, it is necessary to find appropriate cross correlation window size for each Reynolds number, frequency and chamber length which indicates the sensitivity of this method to window size. Second, the appropriate window size is often more than 25 times the period. For example, in an actuation with f = 5 Hz, the window size should be at least t_w = 5 s and due to this long delay this method can not be utilized for real-time flow monitoring.

Moreover, selection of the right cross correlation peak which represents the delay between two signals, requires different approaches and is also problematic. For example, sometimes the highest peak (maximum) of the cross correlation corresponds to the delay (see Figure D.1) and sometimes the selection of appropriate peak is confusing (see Figure D.2). This issue can be attributed to the fact that this flow jumps (flaps) between a few spots on the periphery of the chamber wall instead of the precession; that is why mounting four discrete pressure taps and using cross correlation does not always succeed in monitoring the flow behavior using the cross correlation method.

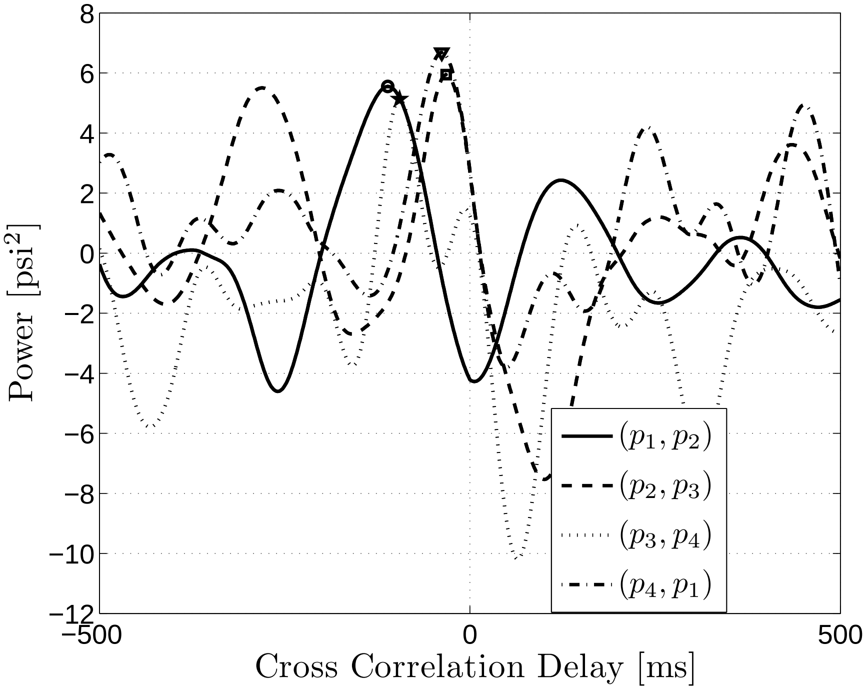

Figure D.1: Cross correlation between p_3 and p_4, the maximum peak should be chosen, though it is not the closest one, $\frac{L}{D} = 2.5$, $Re = 47,000$ and no actuation and without center body.

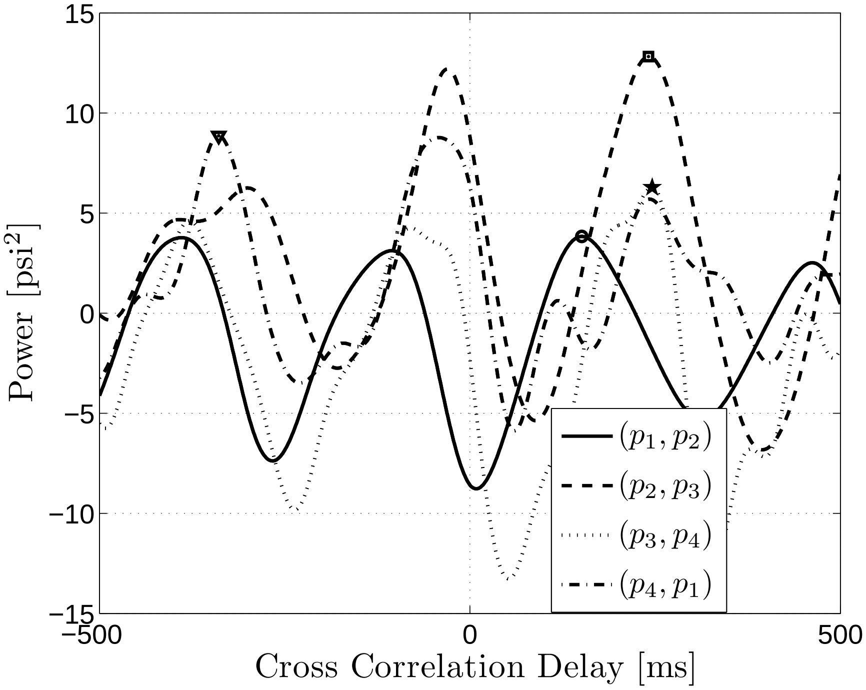

Figure D.2: Cross correlation peak selection, problematic example between p_2 and p_3, the question is which peaks should be chosen, $\frac{L}{D} = 2.5$, $Re = 47,000$ and no actuation and without center body.